Primary Zone Modeling for Gas Turbine Combustors

by

David Scott Underwood

B.S. Aeronautics and Astronautics, Massachusetts Institute of Technology, 1993
M.S. Aeronautics and Astronautics, Massachusetts Institute of Technology, 1995

Submitted to the Department of Aeronautics and Astronautics
in partial fulfillment of the requirements for the degree of

Doctor of Science

at the

MASSACHUSETTS INSTITUTE OF TECHNOLOGY

June 1999

Author .....
Department of Aeronautics and Astronautics
April 30, 1999

Certified by .....
Ian A. Waitz
Professor of Aeronautics and Astronautics
Thesis Supervisor

Certified by .....
Edward M. Greitzer
H. N. Slater Professor of Aeronautics and Astronautics

Certified by .....
William A. Sowa
Senior Research Engineer, United Technologies Research Center

Certified by .....
Saadat A. Syed
Design Chief, Pratt & Whitney

Accepted by .....
Professor Jaime Peraire
Chairman, Department Graduate Committee

Primary Zone Modeling for Gas Turbine Combustors

by

David Scott Underwood

Submitted to the Department of Aeronautics and Astronautics
on April 30, 1999, in partial fulfillment of the
requirements for the degree of
Doctor of Science

Abstract

Gas turbine combustor primary zone flows are typified by swirling flow with heat release in a variable area duct, where a central toroidal recirculation zone is formed. The goal of the research was to develop reduced-order models for these flows in an attempt to gain insight into, and understanding of the behavior of swirling flows with combustion. The specific research objectives were *(i)* to develop a quantitative understanding and ability to compute the behavior of swirling flows with heat addition at conditions typical of gas turbine combustors, *(ii)* to assess the relative merits of various reduced-order models, and *(iii)* to define the applicability of these models in the design process.

To this end, several reduced-order models of combustor primary zones were developed and assessed. The models represent different levels of modeling approximations and complexity. The models include a quasi-one-dimensional control volume analysis, a streamline curvature model, a quasi-one-dimensional model with recirculation zone capturing (CFLOW), and an axisymmetric Reynolds-averaged Navier-Stokes code (UTNS). The models were evaluated through inter-comparison, and comparison with experiment. Following this evaluation, CFLOW was applied to a lean-premixed combustor for which three-dimensional Navier-Stokes solutions existed.

These simplified analyses/models were able to capture the features of swirling flows with heat release across flow regimes of interest in gas turbine combustors, provide insight into the underlying physics, and yield guidelines for design purposes. Cross-comparison of the reduced-order models highlighted the aspects of these flows that need to be described accurately. Specifically, modeling of the mixing on the downstream boundary of a recirculation zone is crucial for accurate computation of these flows, with both Reynolds stresses and bulk transport across the interface being accounted for in order to capture recirculation zone closure. The simplified mixing and heat release models used had limitations arising from the need to input empirically-derived parameters. Calibration of these parameters with higher-fidelity computations and experiments allowed comparison of the models across the flow regimes of interest. Following calibration of the mixing and heat release models, CFLOW was able to compute recirculation zone volumes to within 25% of those given by both the axisymmetric and three-dimensional Navier-Stokes codes for swirl ratios between 0.5 and 1.0 and equivalence ratios between 0.0 and 0.8.

Thesis Supervisor: Ian A. Waitz
Title: Professor of Aeronautics and Astronautics

Acknowledgments

Support for this work was provided by the Office of Naval Research under ONR Grant N00014-95-1-0592 with Dr. Gabriel D. Roy as technical monitor and by Pratt & Whitney under contract number 98-023 with Dr. Steven Kramer as technical monitor. This support is gratefully acknowledged.

The research presented herein could not have been carried out without the help of many individuals. First, I want to thank my committee members, Professor **Ian A. Waitz**, Professor **Edward M. Greitzer**, Dr. **William A. Sowa** of the United Technologies Research Center, and Dr. **Saadat A. Syed** of Pratt & Whitney, for their guidance and encouragement. I would also like to thank Professor **Mark Drela** for his guidance in modifying and running the streamline curvature code as well as developing the quasi-one-dimensional model with recirculation zone capturing. Thanks also to Professor **David Darmofal** for his insights and help in implementing the sensitivity analysis into the aforementioned quasi 1-D model. In addition, I would like to thank Professor **Frank E. Marble** of the California Institute of Technology and Professor **Nick A. Cumpsty** of Cambridge University for numerous stimulating discussions and insightful suggestions. Also, thanks to Dr. **Gavin Hendricks** and Dr. **Dochul Choi** of the United Technologies Research Center for their expertise in modifying and running the axisymmetric Navier-Stokes code.

I'd like to thank everyone at Pratt & Whitney in West Palm Beach, Florida who made my stay there a little more enjoyable. Thanks especially to **Saumil Shah** for the golfing sessions, as well as **Jason Norris**, **Steve Soloff**, and Dr. **Tory Brogan** for the lunchtime (and worktime) humor.

Thanks also to all of my office mates, past and present. In particular, I would like to thank Dr. **Don Hoying**, Dr. **Yifang Gong**, Huu Duc Vo, Brian Corn, and Rajesh Khan for the laughs as well as the technical help.

I would like to thank my closest friends, fraternity brothers all, for the help, encouragement, and especially, the late nights at Crossroads and the Pour House over the years. Thanks to Dr. **Brett Masters**, **Eric 'Radar' Bodnar**, **Tomonori 'Ish' Ishikawa**, and **Travis Atkins** for being such good friends for so long. I owe you. Also, thanks to **Chris 'Meat' Spadaccini**, **Nick Hirschi**, **Hans-Georg Liemke**, **Daryl Hemingway**, and **Eric Martin**. For those of you I've forgotten, forgive me.

I have to thank **Hope Galley** for being my confidant and very dear friend for so many years. Seems like we met just yesterday, but its been close to 15 years now. Thank you for everything. Living so far apart has been difficult.

Finally, to my parents **Larry** and **Jayne Underwood**, thank you for everything. From the financial support you never failed to offer, to the emotional support I could not have done without, thank you. I love you.

This work and all the long hours spent on it are dedicated in loving memory to my mother who died on February 14, 1998. I miss you.

Contents

List of Figures

List of Tables

Nomenclature

Roman

A	Control volume area
b'	Planar shear layer growth rate
C_p	Specific heat of air at constant pressure
E	Eckert number, $(u_1 - u_2)^2 / Cp_t T_1$
H_r	Enthalpy due to tangential shear work
H_t	Enthalpy due to conduction
H_x	Enthalpy due to axial shear work
$\tilde{H}$	Bulk transport of enthalpy across control volume edge
$\tilde{H}_j$	Enthalpy due to jet injection
h	Enthalpy
L	Duct length
M	Mach number
M_x	Axial momentum due to axial shear stress
$\mathcal{M}$	Momentum, $\dot{m}u$
$\tilde{M}$	Bulk transport of axial momentum across control volume edge
$\tilde{M}_j$	Axial momentum due to jet injection
$\dot{m}$	Mass flow
$\tilde{m}$	Bulk transport of mass across control volume edge
$\tilde{m}_j$	Injected jet mass flow
Pr_t	Turbulent Prandtl number
p	Static pressure
R	Radius of duct
	Specific gas constant

Re_b	Reynolds number based on shear layer thickness, $\Delta U b/\nu_t$
$\tilde{R}_j$	Radial momentum due to jet injection
r	Velocity ratio, u_1/u_2
s	Density ratio, ρ_1/ρ_2
T	Static temperature
T_r	Tangential momentum due to tangential shear stress
$\tilde{T}$	Bulk transport of tangential momentum
$\bar{U}$	Average axial velocity of core and outer streams
ΔU	Velocity difference, $u_1 - u_2$
u	Velocity in axial direction
v	Velocity in radial direction
w	Velocity in circumferential direction
z	Coordinate in axial direction

Greek

α	Area ratio, A_D/A_1
Γ	Circulation
γ	Jet injection angle
δ	Radius of vortex core
η	Ratio of specific heats at constant pressure, C_{p_1}/C_{p_2}
ν_t	Effective turbulent viscosity
Ξ	Mixing coefficient
ρ	Density
$\bar{\rho}$	Average density of two adjacent control volumes
τ	Temperature ratio, T_1/T_2
τ_x	Axial shear stress
ϕ	Equivalence ratio
Ω	Swirl ratio, $\Gamma/2\pi\delta u_1$

Subscripts

D	Duct
c	Centerline
j	Jet injection
m	Mixing
pr	Product formation due to chemical reaction
1	Vortex core
2	Irrotational outer stream

Chapter 1

Introduction

1.1 Background and Motivation

The behavior of gas turbine combustor primary zone flows impacts ignition, stability, efficiency, and pollutant formation. Primary zones are typified by swirling flow with heat release in a variable area duct, where a central toroidal recirculation zone is formed. This recirculation zone allows the mixing of hot products with incoming reactants, thereby anchoring the flame.

The work presented in this thesis focuses on lean-premixed (LP) combustor technology which has proven effective in reducing NO_x levels[1]-[5]. Typical strategies for obtaining low NO_x levels from these combustors include tailoring the inlet swirl distribution and the local fuel-air ratio distribution. This complex parametric optimization problem is difficult to tackle efficiently using either experiments or three-dimensional numerical simulations. Further, although much research has been devoted to this area, application-specific experimental and numerical studies have often given little physical insight[6]-[8]. The present work is based on the idea that a need thus exists for reduced-order models which fill the gap between experiments and higher-order numerical methods. These reduced-order models are not intended as a replacement for higher-order codes, but rather as a complement to them, providing a physically-based, computationally efficient parametric design tool which can lend itself to providing the insight needed for developing a design philosophy.

1.2 Literature Review

A review of the literature reveals extensive work in the areas of vortex breakdown, swirling flows with heat release, and combustor design. These works can be grouped generally into three categories. These include review papers, experimental studies, and numerical efforts for computation and modeling. The literature points toward a need for reduced-order modeling of swirling, recirculating flows

with heat addition.

Looking first at the review papers, three are the most closely related to the current work. The first by Escudier[9] summarizes the results of work on vortices in ducts for nonreacting flows. Basic aspects of confined vortex flows such as swirl profiles, conditions for vortex breakdown, and the difference between critical and subcritical vortex flow regimes are reviewed. An overview of the current challenges for gas turbine combustor design is given by Gupta and Lilley[10]. They discuss issues of environmental pollution, NO_x production and reduction schemes, combustion modeling, and numerical simulation. Their conclusions point toward an increase in modeling efforts to aid in the design process for gas turbine combustors. The final review paper by Lilley[11] discusses advances in experimentation, modeling, and prediction of combustor swirl flows. In particular, it highlights the areas of mixing and heat release modeling, improved CFD methods, and application to realistic three-dimensional problems for further research.

The body of experimental work present in the literature is extensive. Gupta, *et al.*[1]-[5], have worked on reduced emissions through the tailoring of inlet swirl velocities in a multi-annular burner. This allowed more control over the mixing downstream of the inlet. The effect of heat release was shown to reduce the size of a recirculation zone. Comparison to computations showed the ability of numerical simulations to yield accurate estimates for flow quantities after calibration of kinetic and mixing coefficients. However, the large parametric space created by the multi-annular burner limits the usefulness of experiments and computations in determining design trends.

Rizk and Mongia[12] and Mellor and Fritsky[13] developed combustor models based on linking empirical correlations. These combustor models rely heavily on the existence of data for the flow conditions present. Therefore, while experimental comparisons for heat transfer, emissions, and primary/secondary jet locations were good, the usefulness of the models for gaining physical understanding was limited.

Smith, *et al.*[14], studied the effects swirl on mixing in a duct with and without heat addition. Swirl was shown to enhance both bulk mixing and small-scale mixing in the duct. Heat release was shown to hinder mixing. Murthy, *et al.*[15], studied the cold flow behavior of a recirculation zone downstream of a swirler. In addition, the interaction of recirculation zones from multiple swirlers was investigated. Recirculation zones formed at the outer duct walls due to a rearward facing step were seen to form and dissolve without explanation. The single swirler cases showed a lack of symmetry, with a precession of the recirculation zone about the centerline. In addition, interaction of adjacent recirculation zones showed a bulk flow in the annular direction. No physical explanation of these effects was given.

Samuelsen, *et al.*[16], studied the interaction of primary jets and swirl-induced recirculation zones. They found that for low momentum jets, the jets do not affect the recirculation zone. For high momentum jets, the jets penetrate to the centerline and cause a decrease in the recirculation

zone length. For very high momentum jets, a significant amount of jet fluid is entrained upstream into the recirculation zone. Heat release was found to reduce the amount of jet entrainment. Whitelaw, *et al.*[6, 7], studied the effects of swirl, heat release, and jet injection on recirculation zone size and combustion products. It was found that reducing the inlet swirl caused an increase in jet penetration and combustion efficiency. Increasing heat release decreased the jet penetration and resulted in a weaker recirculation zone.

Hedman *et al.*[17], studied the effect of fuel-air ratio on the flame structure downstream of a rearward-facing step. The flame structure was found to be held on the downstream edge of the recirculation zone for equivalence ratios below stoichiometric. For fuel-rich conditions, the flame was anchored on the lip of the step. The structure of the flame was found to be intermittent with large holes where fluid passed through unburnt, implying the need for unsteady flow models.

Computational and modeling work is also present in the literature. Heiser, *et al.*[18], developed a set of influence coefficients for a swirling flow in an unconfined environment. This analysis was able to lend insight into the physics of several problems of interest in turbomachinery. However, the parameterization of independent variables and local flow quantities used detracted from the interpretability and use of the formulation for confined flows with mixing. So and Nikjooy[19] and Chao[20] investigated the modeling of mass transport in combustor flows. Calibration of turbulent viscosity through comparison to experimental data showed that accurate computation of a combustor flowfield is possible. It was found that the mixing was captured accurately except near the downstream stagnation point associated with the end of the recirculation zone.

Koutmos and McGuirk[8] computed swirl-stabilized combustor flows for nonreacting conditions. They found that while local velocity errors where high, calculation of the overall flow structure was possible. In particular, the size and location of a recirculation zone could be computed with reasonable accuracy. Sturgess and Syed[21] studied the prediction of confined axisymmetric swirling flows. They found that swirling flows near critical (*i.e.*, near formation of a recirculation zone) are highly dependent on the inlet boundary conditions. In addition, they found that while more accurate turbulence modeling was needed to predict the recirculation zone, mixing had relatively little effect on the mean flow quantities. Rizk and Mongia[22] used 3-D computations to evaluate the performance of a gas turbine combustor. They highlighted several important primary zone structures and phenomena that need to be computed accurately. These included the volume and location of the recirculation zone and the fraction of air entrained into the recirculation zone.

Hussain, *et al.*[23], took a slightly different approach toward reduce-order modeling of combustor flows. They developed analytical solutions to the Navier-Stokes, heat, and diffusion equations along with a technique for matching asymptotic expansions, allowing description of complex swirling flows with recirculation and combustion. They showed that using a composite solution of more basic flow solutions, it was possible to deduce appropriate flow patterns, shapes and positions of flame

fronts, heat transfer, and burner geometries. Optimal parameters were found for flame stabilization and flame-surface expansion, prolonging the residence time of the reactants favorable for complete combustion, enabling a parametric study to optimize the geometry, flowfield, and flame front of a lean-premixed industrial combustor. This optimization was similar to the long-term goals of the work presented in this thesis.

Review of the literature thus shows that while some reduced-order modeling has been done, a need for more work exists. Much experimental and higher-order computational work has been done, providing some knowledge of specific flowfields. However, these efforts have failed to add significant insight into the underlying physics of swirling, recirculating flows with heat addition.

1.3 Objectives

The present research was aimed at illustrating the global features of swirling flows with combustion in order to clarify and understand the behavior of primary zone flows in lean-premixed gas turbine combustors. The specific research objectives were:

1. Develop the ability to predict the behavior of swirling flows with heat addition at conditions typical of gas turbine combustors.
2. Assess the relative merits of various simplified models.
3. Define the applicability of these simplified models in the design process.

The development of physical understanding of these flows, although less quantifiable than the above three goals, was also a key objective.

1.4 Approach

The reduced-order models of primary zone flows include a quasi-one-dimensional (quasi 1-D) control volume analysis, a streamline curvature code, a quasi 1-D control volume analysis with recirculation, and a Reynolds-averaged axisymmetric Navier-Stokes code. The differing levels of modeling approximations inherent in these models were assessed through inter-comparison of the models, as well as through comparison with experimental data. Application of these models to a combustor allowed insight into their potential utility in the design process.

1.5 Contributions

Contributions from this research include:

1. *The reduced-order models were shown to provide physical insight into complex swirling reacting flow problems.* As an example, an influence coefficient analysis of these flows yielded design trend information and elucidated counter-intuitive high swirl trend reversals for recirculation zone size as a function of heat release. These trend reversals had been observed, but not explained.

2. *A reduced-order model allowing computation of recirculation zone size in agreement with axisymmetric and 3-D Navier-Stokes codes was developed.* This model, which yielded flowfield information as well as flowfield sensitivity information, was shown to have potential for utility in the design process.

3. *Cross-comparison of the reduced-order models highlighted the aspects of swirling flows with heat addition that must be described well.* Capturing the mixing on the downstream boundary of a recirculation zone is crucial for computation of these flows. In addition, accurate description of the heat release is necessary over the entire flowfield.

4. *Limitations of simplified mixing and heat release models were determined.* Calibration of input parameters through comparison with experiments and higher-order computations was found to be necessary for accurate computation of recirculation zone volume and location. This calibration was similar to that necessary in higher-fidelity CFD codes. Following calibration of the mixing and heat release models, CFLOW was able to compute recirculation zone volumes to within 25% of those given by both the axisymmetric and three-dimensional Navier-Stokes codes for swirl ratios between 0.5 and 1.0 and equivalence ratios between 0.0 and 0.8.

1.6 Overview

The thesis begins with a description of the quasi 1-D control volume model without recirculation, as well as the influence coefficient analysis, in Chapter 2. The quasi 1-D control volume model with recirculation (CFLOW) is described in Chapter 3. The axisymmetric Navier-Stokes code (UTNS) is described in Chapter 4. The results from inter-comparison of the models along with the comparison to experimental data is presented in Chapter 5, while the results of applying CFLOW to a combustor are presented in Chapter 6. Chapter 7 contains a summary, and conclusions, as well as some suggestions for extension of CFLOW. Appendix A provides a description of a streamline curvature model which was examined and rejected for further development, while Appendix B discusses the details of the Newton matrix set up in CFLOW. Appendix C contains a user's manual for CFLOW. Appendix D discusses a possible CFLOW sensitivity analysis modification to allow examination of recirculation zone dynamics, while a discussion of an extension of CFLOW to unsteady flows is presented in Appendix E.

Chapter 2

Quasi 1-D Control Volume Model

The quasi 1-D differential control volume model developed is an extension of the work of Darmofal, *et al.*[24], which focused on the behavior of confined vortex cores in pressure gradients with no heat release or mixing. Through comparison with axisymmetric Navier-Stokes simulations, they showed that the simplified model could be used to predict the onset of recirculation zone formation.

Here we consider a more general case of a vortex core in a duct of varying area, where heat release in the core and outer flow, and mixing between the streams are allowed. The derivation of this quasi 1-D model follows that of Khan[25], and is described in Sections 2.1 and 2.2. Section 2.3 describes the influence coefficients and their development, while Section 2.4 contains a discussion of the results from the quasi 1-D model without recirculation.

2.1 Assumptions

Figure 2-1 shows a schematic of the model flowfield which is taken to be axisymmetric, steady, and smoothly varying in the axial direction. A cylindrical coordinate system $\vec{x} = (r, \theta, z)$ with velocity components $\vec{u} = (v, w, u)$ is used. The flow field is divided into a vortex core of radius $\delta(z)$ containing all the axial vorticity (denoted stream 1), and an irrotational outer flow (denoted stream 2). The duct radius, $R(z)$, is specified.

The swirl velocity is taken to be a Rankine vortex

$$w(r,z) = \begin{cases} \frac{\Gamma}{2\pi\delta}\frac{r}{\delta} & 0 \le r \le \delta \\ \\ \frac{\Gamma}{2\pi r} & \delta \le r \le R \end{cases} . \tag{2.1}$$

This is not a fundamental limitation of the model, other distributions may be specified, however,

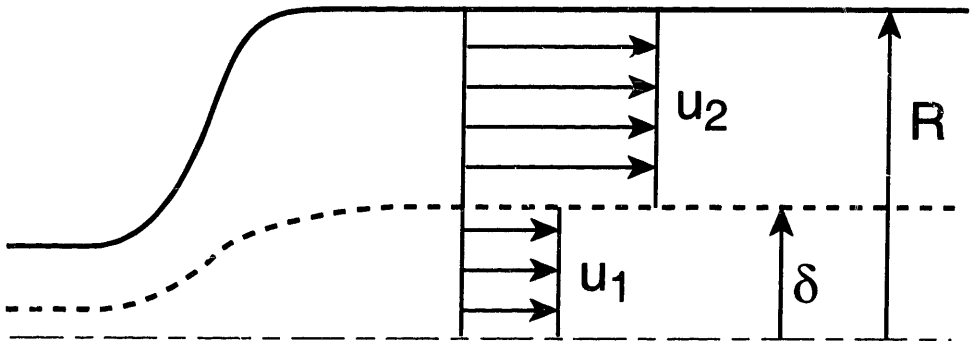

Figure 2-1: Quasi one-dimensional model without recirculation.

LP combustor inlet data suggests that this profile is an appropriate approximation for many flows of interest[26]. The radial velocity is assumed negligible in the quasi 1-D formulation, so the radial momentum equation reduces to

$$\frac{\partial p}{\partial r} = \rho \frac{w^2}{r}. \tag{2.2}$$

Axial velocities in the two streams are assumed constant over an axial cross-section, although the axial velocities are not necessarily the same in each stream. This implies infinitely fast mixing *within* each stream in order to enforce uniform profiles. This *intra-stream* mixing is not the same as the *inter-stream* mixing, or mixing between the streams, which can be specified in the model. While the model allows exchange of momentum and energy between streams, the net mass exchange is zero (*i.e.*, equal and opposite).

2.2 Conservation Equations

Applying conservation of mass, momentum, and energy, as well as the state equation and a summation of areas to the two streams yields a system of differential equations. Conservation of mass for streams 1 and 2 can be expressed as

$$\frac{d\rho_1}{\rho_1} + \frac{du_1}{u_1} + \frac{dA_1}{A_1} = 0, \tag{2.3}$$

$$\frac{d\rho_2}{\rho_2} + \frac{du_2}{u_2} + \frac{dA_2}{A_2} = 0. \tag{2.4}$$

Conservation of momentum for the two streams gives

$$\frac{du_1}{u_1} + \frac{dp_c}{\rho_1 {u_1}^2} - \frac{1}{2}\Omega^2 \frac{dA_1}{A_1} = \frac{d\mathcal{M}}{\dot{m}_1 u_1}, \tag{2.5}$$

$$\frac{du_2}{u_2} + sr^2 \frac{dp_c}{\rho_1 {u_1}^2} - \frac{1}{2}(s+1)r^2\Omega^2 \frac{dA_1}{A_1} + \frac{1}{2}sr^2\Omega^2 \left(\frac{\alpha}{\alpha - 1}\right) \frac{d\rho_1}{\rho_1}$$

$$+ \frac{1}{2}r^2\Omega^2 \left(\frac{\alpha - \ln \alpha}{\alpha - 1}\right) \frac{d\rho_2}{\rho_2} = \frac{-sr^2}{\alpha - 1} \frac{d\mathcal{M}}{\dot{m}_1 u_1}, \tag{2.6}$$

where the different quantities are defined in the Nomenclature section. The terms containing area and density differentials that appear on the left-hand side of Equations 2.5 and 2.6 reflect the effect of the swirl component of velocity. The source term on the right-hand side of the equations represents the transfer of momentum from one stream to the other due to mixing.

Conservation of energy for the two streams is expressed as

$$\frac{dT_1}{T_1} + \frac{{u_1}^2}{C_{p_1} T_1} \frac{du_1}{u_1} = \frac{dh_{pr_1}}{C_{p_1} T_1} + \frac{dh_m}{C_{p_1} T_1}, \tag{2.7}$$

$$\frac{dT_2}{T_2} + \frac{{u_2}^2}{C_{p_2} T_2} \frac{du_2}{u_2} = \frac{dh_{pr_2}}{C_{p_2} T_2} - \frac{sr\eta\tau}{\alpha - 1} \frac{dh_m}{C_{p_1} T_1}. \tag{2.8}$$

The source terms on the right-hand side of the equations represent the enthalpy addition due to combustion (dh_{pr}) and the transfer of enthalpy from one stream to the other due to mixing (dh_m).

The equation of state for the two streams is

$$\frac{dp_c}{p_c} - \frac{d\rho_1}{\rho_1} - \frac{dT_1}{T_1} = 0, \tag{2.9}$$

$$\frac{dp_c}{p_c} - \frac{d\rho_2}{\rho_2} - \frac{dT_2}{T_2} = 0. \tag{2.10}$$

Summation of areas yields

$$\frac{1}{\alpha} \frac{dA_1}{A_1} + \frac{\alpha - 1}{\alpha} \frac{dA_2}{A_2} = \frac{dA_D}{A_D}. \tag{2.11}$$

For the parametric studies presented, the duct radius was specified by the function

$$R(z) = a[\text{erf}\,(bz - c) + 1] + R_0, \tag{2.12}$$

where a, b, and c were chosen to give a geometry typical of gas turbine combustors[27]. The values of a, b, and c used in the examples are 0.02, 60, and 2.5, respectively. Again, the form of Equation 2.12 provides a convenient expression but other forms may be used to address other geometries.

Heat release profiles, $dh_{pr_i}(z)$, are also specified for both streams, with profiles representative of those found in modern combustors. The total heat release in each stream relative to the incoming flow enthalpy is set to represent a methane-air reaction of the form

$$CH_4 + \frac{2}{\phi_i}(O_2 + 3.76N_2) \rightarrow CO_2 + 2H_2O + \left(\frac{2}{\phi_i} - 2\right)O_2 + \frac{7.52}{\phi_i}N_2. \tag{2.13}$$

where ϕ_i is the equivalence ratio of stream i.

The heat release profile is taken the same for both streams except for the value of the peak which is set by ϕ_i. The profile is given by the function

$$dh_{pr_i} = \phi_i\, dh_{max}\left\{\left[\text{erf}\left(d\frac{z}{L}\right) + \frac{1}{2}\text{erfc}\left(e\frac{z}{L} - f\right)\right] - 1\right\}, \tag{2.14}$$

where d, e, and f have been chosen to give heat release profiles typical of gas turbine combustors[12]. For all computations $L/R_0 = 5$, $d = 14$, $e = 7$, and $f = 3$. Figure 2-2 shows heat release profiles for low and high heat release cases ($\phi = 0.2$ and 0.8) along with the duct geometry. The consequences of varying the functional form of the heat release profiles and duct geometry were not evaluated in the current study, and only effects of the overall level of heat release were investigated.

Mixing causes exchange of momentum and energy between the two streams. A mixing coefficient, Ξ, is specified where Ξ is a fraction of the mixing rate set by an effective turbulent viscosity, ν_t. The mixing rate is thus proportional to $\Xi\nu_t$ where ν_t is determined using Prandtl's second hypothesis[28, 29]

$$\nu_t = C_1(b'\bar{U})^2\frac{z}{\bar{U}}. \tag{2.15}$$

and where b' is defined as[30]

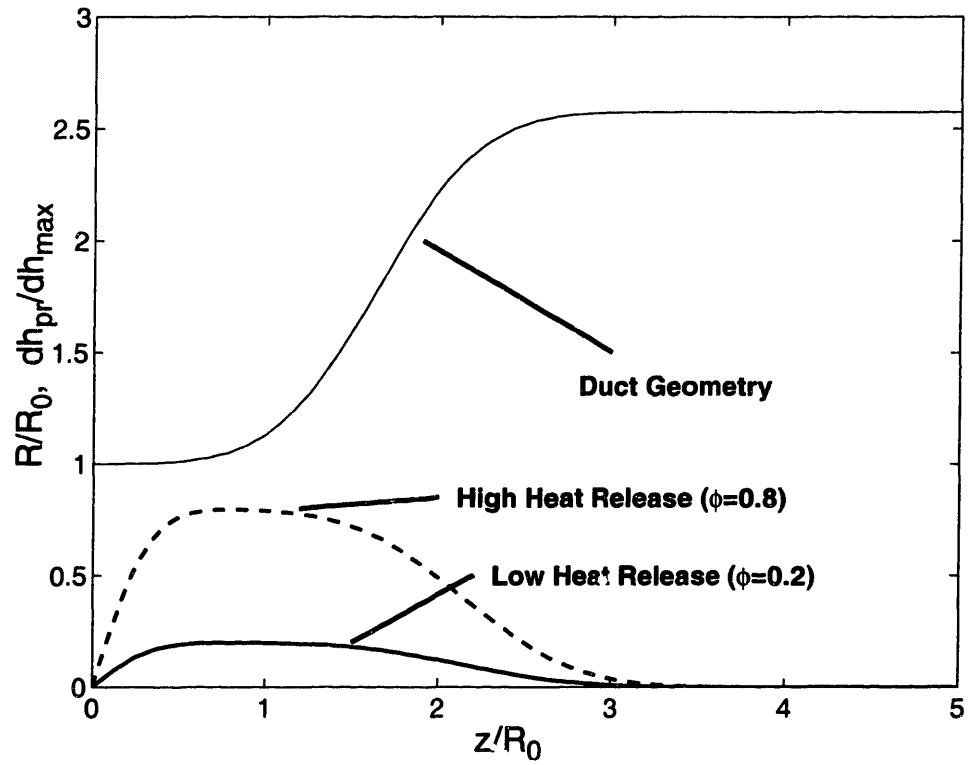

Figure 2-2: Heat release and duct radius profiles.

$$b' = \frac{.37(1-r)(1+s^{\frac{1}{2}})}{2(1+s^{\frac{1}{2}}r)}B,$$
$$B = 1 - \frac{1-s^{\frac{1}{2}}}{(1+s^{\frac{1}{2}})\left[1+2.9\frac{(1+r)}{(1-r)}\right]}. \tag{2.16}$$

The constant C_1 in Equation 2.15 is found by using an error function for the velocity profile across the shear layer and using the 5% and 95% points to compute C_1, yielding a value of $C_1 = 0.092$. The momentum transfer term, $d\mathcal{M}/\dot{m}_1 u_1$, can thus be expressed as

$$\frac{d\mathcal{M}}{\dot{m}_1 u_1} = -\frac{1}{Re_b}\frac{\rho_1+\rho_2}{\rho_1}\frac{(u_1-u_2)^2}{{u_1}^2}\frac{1}{\delta}. \tag{2.17}$$

The energy transfer term can be related to the momentum transfer term by

$$\frac{dh_m}{C_{p_1}T_1} = \frac{r}{r-1}\left[\frac{1}{Pr_t}\frac{\tau-1}{\tau}+E\right]\frac{d\mathcal{M}}{\dot{m}_1 u_1}. \tag{2.18}$$

Again, no effort was made to study the consequences of varying the functional form of the momentum and energy exchange. Only the sensitivity of the model results to the overall mixing rate (ν_t) was investigated. These results are discussed in Section 2.4.

Equations 2.3-2.11 are solved by specifying inlet conditions, duct geometry, heat release profiles, and mixing rate and then integrating along the duct in the axial direction. The equations are thus parabolic and downstream influences are not felt. This assumption has been investigated by Darmofal, *et al.*[24], for the case without heat addition and mixing, where it was shown, through comparison with solutions from a Navier-Stokes code, that a quasi 1-D model can capture the overall features of the flow, including the tendency for recirculation zone formation.

2.3 Influence Coefficients

Influence coefficients represent the sensitivity of various flow parameters (dependent variables) to changes in area, heat addition, and mixing (independent variables). Their utility lies not only in quantitative results, but also in the insight they afford into the roles that various mechanisms play in determining the flow behavior. Based on the above formulation, influence coefficients for two streams with area change, heat release, and mixing have been derived following the method developed by Shapiro and Hawthorne[31] and popularized through circulation of the text by Shapiro[32].

There are several features about the flows of interest that can be used to simplify the influence coefficient analysis compared to the full set of equations (Eqns. 2.3-2.11). First, as is the case in gas turbine combustors, Mach numbers are low enough that changes in pressure have no significant effect on density, and the state equation is thus $\rho T \approx const + O(M^2)$. (This assumption implies that the quantity $dp/p \approx 0$; the quantity $dp/\rho u^2$ is not zero.) Density variations are thus due only to heat release. Further, kinetic energy changes are also small compared to enthalpy changes. Equations 2.7, 2.8, 2.9, and 2.10 then simplify to

$$\frac{dT_1}{T_1} = \frac{dh_{pr_1}}{C_{p_1}T_1} + \frac{dh_m}{C_{p_1}T_1}, \tag{2.19}$$

$$\frac{dT_2}{T_2} = \frac{dh_{pr_2}}{C_{p_2}T_2} - \frac{sr\eta\tau}{\alpha - 1}\frac{dh_m}{C_{p_1}T_1}, \tag{2.20}$$

$$\frac{d\rho_1}{\rho_1} + \frac{dT_1}{T_1} = 0, \tag{2.21}$$

$$\frac{d\rho_2}{\rho_2} + \frac{dT_2}{T_2} = 0, \tag{2.22}$$

respectively.

The influence coefficients for this set of equations are summarized in Table 2.1. They represent the sensitivities of the dependent variables (shown in the left most column) to changes in the independent variables (shown in the top row). The influence coefficients collapse to the results of Shapiro[32] for a single stream with no swirl at low Mach number.

As with the full set of equations, Eqns. 2.3-2.6, 2.11, and 2.19-2.22 can be integrated to yield a complete nonlinear solution. Their greatest practical use, however, is to indicate the directions and rates of change of flow variables *locally*. This type of analysis provides a pathway for understanding complex fluid behavior over a broad parametric range.

The trends derived from the influence coefficients are summarized in Table 2.2. These trends are not dependent on the prescribed geometry, heat release profile, or mixing rate profile since the influence coefficients only describe the local flow behavior based on local ratios of flow variables.

As example of the use of the influence coefficients, we can examine the change in core axial velocity (du_1/u_1) as a function of heat release in the core ($dh_{pr_1}/C_{p_1}T_1$). We focus on this example for two reasons. First, acceleration or deceleration of the vortex core is directly related to the potential for recirculation zone formation, and many combustors rely on a recirculation zone for flame stability. Therefore, a desirable recirculation zone for current combustor applications has average velocities much lower than the flame speed, entrains hot products from downstream and transports them upstream thus yielding a strong radical pool for ignition, and occupies a fraction of the duct large enough to ensure complete combustion across the duct[33]. Second, this situation illustrates a result that may seem counter-intuitive and appears to us to be difficult to arrive at with more complex analyses or experiments. It thus demonstrates the utility of the simplified model.

The relation between the core axial velocity and the core heat release is given by

$$\frac{du_1}{u_1} = \frac{1 - \frac{1}{2}r^2\Omega^2\left[\alpha\left(s+1\right) - 1\right]}{\beta}\frac{dh_{pr_1}}{C_{p_1}T_1}, \tag{2.23}$$

where β is defined as

$$\beta = 1 + r^2\left(\alpha - 1\right)\left(s - \frac{1}{2}\Omega^2\right). \tag{2.24}$$

Examining the denominator of the influence coefficient (Eqn. 2.23), the local swirl ratio, Ω, that

Table 2.1: Influence coefficients for two streams with area change, heat release, and mixing.

	$\frac{dA_D}{A_D}$	$\frac{dh_{pr_1}}{C_{p_1}T_1}$	$\frac{dh_{pr_2}}{C_{p_2}T_2}$
$\frac{dp_c}{\rho_1 {u_1}^2}$	$\frac{\alpha\left(1+\frac{1}{2}\Omega^2\right)}{\beta}$	$-\frac{1-\frac{1}{2}r^2\Omega^2\left[(\alpha-1)+s\left(2\alpha+\frac{1}{2}\alpha\Omega^2-1\right)\right]}{\beta}$	$-\frac{\left(1+\frac{1}{2}\Omega^2\right)\left[(\alpha-1)-\frac{1}{2}r^2\Omega^2(\alpha-\ln\alpha)\right]}{\beta}$
$\frac{du_1}{u_1}$	$-\frac{\alpha}{\beta}$	$\frac{1-\frac{1}{2}r^2\Omega^2[\alpha(s+1)-1]}{\beta}$	$\frac{(\alpha-1)-\frac{1}{2}r^2\Omega^2(\alpha-\ln\alpha)}{\beta}$
$\frac{du_2}{u_2}$	$-\frac{\alpha r^2\left(s-\frac{1}{2}\Omega^2\right)}{\beta}$	$\frac{sr^2\left(1+\frac{1}{2}\frac{\alpha}{\alpha-1}\Omega^2\right)}{\beta}$	$\frac{r^2\left[(\alpha-1)\left(s-\frac{1}{2}\Omega^2\right)+\frac{1}{2}\Omega^2\left(\frac{\alpha-\ln\alpha}{\alpha-1}\right)\right]}{\beta}$
$\frac{dT_1}{T_1}$	0	1	0
$\frac{dT_2}{T_2}$	0	0	1
$\frac{d\rho_1}{\rho_1}$	0	-1	0
$\frac{d\rho_2}{\rho_2}$	0	0	-1
$\frac{dA_1}{A_1}$	$\frac{\alpha}{\beta}$	$\frac{(\alpha-1)sr^2+\frac{1}{2}\alpha sr^2\Omega^2}{\beta}$	$-\frac{(\alpha-1)-\frac{1}{2}r^2\Omega^2(\alpha-\ln\alpha)}{\beta}$
$\frac{dA_2}{A_2}$	$\frac{\alpha r^2\left(s-\frac{1}{2}\Omega^2\right)}{\beta}$	$-\frac{sr^2\left(1+\frac{1}{2}\frac{\alpha}{\alpha-1}\Omega^2\right)}{\beta}$	$\frac{1-\frac{1}{2}r^2\Omega^2\left(\frac{\alpha-\ln\alpha}{\alpha-1}\right)}{\beta}$
$\frac{dp_{t_1}}{\rho_1 {u_1}^2}$	0	$-\frac{1}{2}\left(1+\Omega^2\right)$	0
$\frac{dp_{t_2}}{\rho_2 {u_2}^2}$	0	0	$-\frac{1}{2}\left(1+\Omega^2\right)$
	$\frac{d\mathcal{M}}{\dot{m}_1 u_1}$		
$\frac{dp_c}{\rho_1 {u_1}^2}$	$\frac{1-sr^2-\frac{1}{2}r^2\Omega^2[\alpha(s+1)-1]}{\beta}-\epsilon\frac{1-\alpha sr^2\Omega^2-\frac{1}{2}r^2\Omega^2\left[(\alpha-1)-s\left(1-\frac{1}{2}\alpha\Omega^2\right)\right]-\left(1+\frac{1}{2}\Omega^2\right)\eta\tau G}{\beta}$		
$\frac{du_1}{u_1}$	$\frac{\alpha sr^2}{\beta}+\epsilon\frac{1-\frac{1}{2}r^2\Omega^2[\alpha(s+1)-1]-\eta\tau G}{\beta}$		
$\frac{du_2}{u_2}$	$-\frac{sr^2\frac{\alpha}{\alpha-1}}{\beta}+\epsilon\left\{\frac{sr^2\left[1-\frac{1}{2}\alpha r^2\Omega^2\left(s-\frac{1}{2}\Omega^2\right)\right]-r^2\left(s-\frac{1}{2}\Omega^2\right)\eta\tau G}{\beta}+J+K\right\}$		
$\frac{dT_1}{T_1}$	ϵ		
$\frac{dT_2}{T_2}$	$-\frac{sr\eta\tau}{\alpha-1}\epsilon$		
$\frac{d\rho_1}{\rho_1}$	$-\epsilon$		
$\frac{d\rho_2}{\rho_2}$	$\frac{sr\eta\tau}{\alpha-1}\epsilon$		
$\frac{dA_1}{A_1}$	$-\frac{\alpha sr^2}{\beta}+\epsilon\frac{(\alpha-1)sr^2+\frac{1}{2}\alpha sr^2\Omega^2+\eta\tau G}{\beta}$		
$\frac{dA_2}{A_2}$	$\frac{sr^2\frac{\alpha}{\alpha-1}}{\beta}-\epsilon\left\{\frac{sr^2\left[1-\frac{1}{2}\alpha r^2\Omega^2\left(s-\frac{1}{2}\Omega^2\right)\right]-r^2\left(s-\frac{1}{2}\Omega^2\right)\eta\tau G}{\beta}+J+L\right\}$		
$\frac{dp_{t_1}}{\rho_1 {u_1}^2}$	$1-\frac{1}{2}\left(1+\Omega^2\right)\epsilon$		
$\frac{dp_{t_2}}{\rho_2 {u_2}^2}$	$-\frac{sr^2}{\alpha-1}+\frac{1}{2}\left(1+\Omega^2\right)\frac{sr\eta\tau}{\alpha-1}\epsilon$		

$$G = sr - \tfrac{1}{2}sr^3\Omega^2\left(\alpha - \ln\alpha\right),\ \epsilon = \tfrac{r}{r-1}\left[\tfrac{1}{Pr_t}\tfrac{\tau-1}{\tau} + E\right],$$

$$J = \tfrac{1}{2}\tfrac{\alpha}{\alpha-1}sr^2\Omega^2,\ K = \tfrac{1}{2}sr^3\Omega^2\left(\tfrac{\alpha-\ln\alpha}{\alpha-1}\right)\tfrac{\eta\tau}{\alpha-1},\ L = \tfrac{sr\eta\tau}{\alpha-1}\left[1-\tfrac{1}{2}r^2\Omega^2\left(\tfrac{\alpha-\ln\alpha}{\alpha-1}\right)\right]$$

Table 2.2: Local trends from influence coefficients.

	Duct Area Change	Heat Release in Core	Heat Release in Outer Flow	Mixing ($2 \rightarrow 1$)
p_c	$\uparrow$	$\downarrow, \Omega < \Omega_2$ $\uparrow, \Omega > \Omega_2$	$\downarrow$	$\uparrow$
u_1	$\downarrow$	$\uparrow, \Omega < \Omega_1$ $\downarrow, \Omega > \Omega_1$	$\uparrow$	$\downarrow$
u_2	$\downarrow, \Omega < \Omega_3$ $\uparrow, \Omega > \Omega_3$	$\uparrow$	$\uparrow$	$\uparrow$
A_1	$\uparrow$	$\uparrow$	$\downarrow$	$\downarrow$
A_2	$\uparrow, \Omega < \Omega_3$ $\downarrow, \Omega > \Omega_3$	$\downarrow$	$\uparrow$	$\uparrow$
p_{t1}	No Effect	$\downarrow$	No Effect	$\uparrow$
p_{t2}	No Effect	No Effect	$\downarrow$	$\downarrow$

yields $\beta = 0$ can be found. This swirl ratio, denoted as Ω_{crit} in Table 2.2 and defined as

$$\Omega_{crit} = \sqrt{2\left[s + \frac{1}{r^2(\alpha - 1)}\right]}, \tag{2.25}$$

corresponds to the critical value of swirl ratio at which (locally) the core growth rate is unbounded. This is of interest because this condition has been linked to recirculation zone formation[24]. In the following discussion, *only swirl ratios below critical* will be considered.

Looking again at Eqn. 2.23 and solving for the swirl ratio that makes the numerator of the influence coefficient zero, a local swirl ratio is found where the sign of the influence coefficient changes. This corresponds to a reversal of the effect of adding heat to the core. Specifically, for low swirl ratios, adding heat to the core accelerates the core, as is familiar from the limiting case of zero swirl. At high swirl ratios, however, adding heat to the core decelerates the core. The transitional swirl ratio between the two regimes is denoted as Ω_1 in Table 2.2 and defined as

$$\Omega_1 = \sqrt{\frac{2}{r^2[\alpha(s+1) - 1]}}. \tag{2.26}$$

Note that Ω_1 is a function of the local ratios of density, velocity, and area only. Thus, from the perspective of combustor design, it is possible for particular choices of local fuel-air ratio and swirler geometry to lead to acceleration or deceleration of the vortex core, thereby hindering or promoting recirculation zone formation.

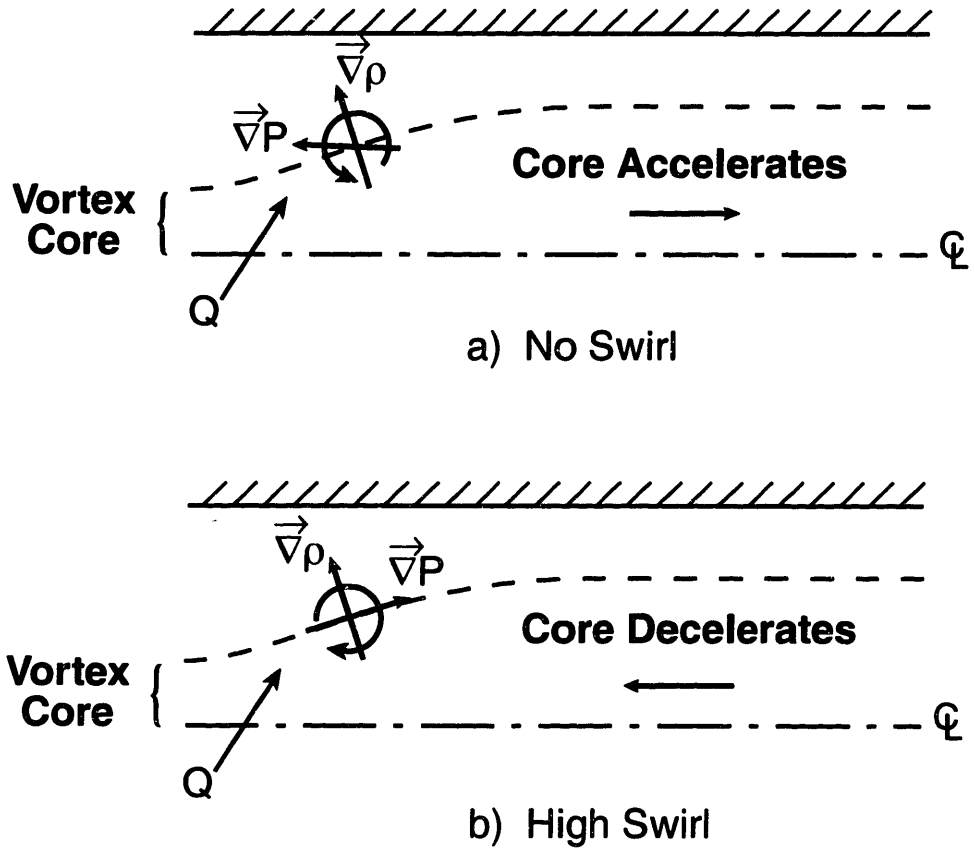

Figure 2-3: Schematic of vorticity production due to baroclinic torque for a) no swirl and b) high swirl.

A physical explanation for the above behavior can be given as follows. Consider the cases of no swirl and strong swirl for a vortex core in a constant area duct, where strong swirl means a swirl ratio just below the critical swirl ratio. For simplicity, we assume the core and outer flow to have the same value of axial velocity upstream of the region of heat addition, although this is not necessary for the arguments that follow.

Consider the no swirl situation first. Heat addition will lower the density and cause the core to expand, as shown in Figure 2-3a. The streamtube area in the outer flow thus contracts, so that the outer flow axial velocity increases and the static pressure decreases in the flow direction. Because the static pressure is uniform across the duct, this implies an acceleration in the core ($\rho u du = -dp$).

Equivalently, the physical basis for the above behavior can be viewed from the perspective of vorticity dynamics by examining the production of vorticity due to the interaction of density and pressure gradients. Changes in the azimuthal vorticity (*i.e.*, vorticity oriented in the θ direction) at the edge of the core, are set by a balance between the production of negative azimuthal vorticity due to stretching and the production of positive azimuthal vorticity due to baroclinic torque. Stretching of the interface occurs due to dilatation of the gas in the core, while the baroclinic torque occurs

due to non-parallel pressure and density gradients.

The only density gradients are across, and normal to, the core-outer flow interface. From the arguments above, the pressure gradient along this interface points in the upstream direction, as shown in Figure 2-3a. Generation of vorticity at the interface is given by

$$\frac{D\vec{\omega}}{Dt} = \frac{1}{\rho^2}\vec{\nabla}\rho \times \vec{\nabla}p. \tag{2.27}$$

Equation 2.27 implies the production of vorticity of the sense indicated in Figure 2-3a and thus acceleration of the core relative to the outer flow.

Consider now the situation of strong swirl, so the effect of the change in axial velocity on static pressure is small. Again, as shown in Figure 2-3b, the core expands in the region of heat addition. At the outer radius of the duct (*i.e.*, at the wall) the azimuthal velocity and the stagnation pressure do not vary along the duct. Radial equilibrium thus implies that in the axial region in which there is heat addition, and therefore core expansion, the static pressure on the interface between the two streams will increase in the direction of the flow. There is thus a pressure force pointing upstream on a volume of the vortex core between stations upstream and downstream of the heat addition, and hence a deceleration of the core.

In terms of vorticity dynamics, we can refer to Figure 2-3b, which shows the static pressure rising along the interface. The sense of the vorticity generated is thus opposite to that in the weak swirl case, so that the fluid in the core is decelerated relative to the outer flow. There are additional effects which need to be accounted for in the general case, for example the effect of the axial velocity changes and the stretching of existing azimuthal vortex lines, both of which are neglected in the above description. The limiting case arguments, however, do capture the essential physical mechanisms.

Examining the influence coefficients further, two more swirl ratios can be defined where other coefficients change sign. These two, denoted as Ω_2 and Ω_3, define the boundaries between the low and high swirl behavior of centerline static pressure with heat release in the core, and outer stream velocity/area with duct area change. The swirl ratios Ω_2 and Ω_3 are defined as

$$\Omega_2 = \sqrt{\frac{-r^2[(\alpha-1)+s(2\alpha-1)]+F}{\alpha s r^2}}, \tag{2.28}$$

and

$$\Omega_3 = \sqrt{2s}, \tag{2.29}$$

where F is given by

$$F = \sqrt{r^4[(\alpha - 1) + s(2\alpha - 1)]^2 + 4\alpha s r^2}.$$

Examining the boundary between high and low swirl behavior of the centerline static pressure with heat addition, it is seen that for low swirl, heat addition causes the pressure at the centerline to decrease, corresponding to an accelerating vortex core. This agrees with the behavior of the core axial velocity at low swirls. At high swirls, the heat addition causes the centerline pressure to increase. This effect has been described above during the discussion of the core axial velocity reversal, pointing out that the pressure gradient is set by the swirl, and therefore the pressure rises along the core edge in the streamwise direction. A third region of very limited extent exists where the local swirl ratio is such that heat addition causes the centerline pressure and the core axial velocity to increase. In this case, dilation causes the pressure to increase in the flow direction, but the core axial velocity still accelerates because the production of positive azimuthal vorticity due to baroclinic torque is greater than the generation of negative azimuthal vorticity due to stretching.

Looking now at the boundary between high and low swirl behavior of the outer flow axial velocity and area with a change in duct area, we see that for the low swirl case, a duct expansion causes the pressure to rise in the axial direction. This causes the velocity of the outer flow to decrease and the area of the outer flow to increase. For high swirl, the expansion of the vortex core due to area change is greater than the difference in the area changes of the duct and outer flow. This squeezes the outer flow, causing the outer flow axial velocity to increase and the area to decrease.

As shown in Table 2.2, several other statements can be made as to the effect of area change, heat release, and mixing on recirculation zone formation. A decrease in core axial velocity moves the flow towards the formation of a recirculation zone, while an increase in core axial velocity moves the flow away from the formation of a recirculation zone. An increase in duct area thus enhances recirculation zone formation, due to the corresponding decrease in core axial velocity.

Noting that there are no regions where the trends change sign for heat release in the outer flow or for mixing between the streams, two general statements about these two inputs can be made. Heat release in the outer flow hinders recirculation zone formation since heat addition causes dilation of the outer flow. This squeezes the vortex core, causing the core axial velocity to increase. Mixing between the streams (defined as positive for exchange of momentum and energy from the outer flow to the core) hinders recirculation zone formation. As defined, mixing serves to re-energize the vortex core by mixing in higher momentum fluid. This increase in momentum (and energy) causes the core axial velocity to increase.

The generalizations that can be drawn from the influence coefficient can thus be summarized as:

1. For low swirl ratios, heat release in the core hinders recirculation zone formation.
2. For high swirl ratios, heat release in the core enhances recirculation zone formation.
3. For all swirl ratios, heat release in the outer stream hinders recirculation zone formation.
4. Mixing hinders recirculation zone formation.
5. Increasing duct area enhances recirculation zone formation.

2.4 Results of Quasi 1-D Analysis Without Recirculation

The local trends given by the influence coefficients were examined for the overall duct flowfield by using the solution from the 1-D model to calculate values of Ω_1, Ω_2, Ω_3, and Ω_{crit}. These values are compared to the local swirl ratio (Ω) in order to determine the behavior of the flow in a given section of the duct. Figure 2-4a shows the results from a high swirl, low heat release case ($\phi_1 = \phi_2 = 0.2$), while Figure 2-4b shows the results from a high swirl, high heat release case ($\phi_1 = \phi_2 = 0.8$). The values of the inlet parameters for these runs are given in Table 2.3.

In Figure 2-4, the solution from the quasi 1-D model (Ω) is denoted by the *'s. Six regions are defined, labeled 1-6. The boundaries of these regions are the swirl ratios where the influence coefficients, given in Appendix A, change sign. These swirl ratios, defined by Equations 2.26, 2.28, and 2.29 and denoted by the solid, dashed, and dashed-dot lines respectively, have been computed using the solution from the quasi 1-D model. The other boundary on Figure 2-4 is the critical swirl ratio defined by Equation 2.25 and denoted by the "x". It corresponds to the conditions where the influence coefficients go to $\pm\infty$.

The behavior of the flow at any axial location in the duct is determined by which region the solution (Ω) lies in at that point. Region 1 is below all the boundaries, and the behavior of the flow is qualitatively similar to the zero swirl behavior. Region 2 is above the dashed line, meaning that the local swirl ratio (Ω) is greater than Ω_2. This corresponds, as is shown in Table 2.2, to the case where adding heat to the core increases the centerline static pressure, counter to the low

Table 2.3: Conditions for the high swirl cases of Figure 2-4.

Inlet Parameter	Value
Swirl Ratio, Ω_0	1.5
Velocity Ratio, r_0	0.8
Density Ratio, s_0	1
Area Ratio, α_0	4

swirl behavior. Region 3 lies above both the solid and dashed lines (Ω_1 and Ω_2, respectively), so adding heat to the core increases the centerline static pressure and decelerates the core as shown in Table 2.2.

In region 4, adding heat to the core accelerates the core and decreases the centerline static pressure as in the zero swirl case. However, increasing the duct area increases the axial velocity of the outer stream and decreases the area of the outer stream. This effect, shown in Table 2.2, is again counter to the zero swirl case. In region 5, adding heat to the core increases the centerline static pressure, while increasing the duct area increases the outer stream axial velocity and decreases the outer stream area. Finally, in region 6 adding heat to the core increases the centerline static pressure and decreases the core axial velocity, while increasing the duct area increases the outer stream axial velocity and decreases the outer stream area. All of these effects are summarized in Table 2.2.

Comparing the low and high heat release cases of Figures 2-4a and b respectively, it is seen that the shape of the six regions changes somewhat as does the trajectory of the solution (*'s), although the solution begins and ends in the same regions. Plotting the solution in this manner is useful for understanding the parametric behavior. Examination of the solution and its relation to the boundaries for trend reversal given by the influence coefficients allows the determination of the effect of heat release for a given set of inlet conditions, heat release profiles, and geometry.

Note that at no point in either Figures 2-4a or 2-4b does the local swirl ratio approach the critical swirl ratio (Ω_{crit}). A case was computed with a duct-to-core area ratio of 100 instead of 4, and this showed a significant growth of the core as the local swirl ratio approached critical. This rapid and large core growth along with a concurrent drop in core axial velocity toward zero, indicates the onset of reverse flow, and hence recirculation zone formation. However, the reversed flow case cannot be computed by the current model, and therefore only a solution with a swirl ratio less than critical can be studied. The likelihood of recirculation zone formation is greatly increased for larger initial area ratios, corresponding to starting with a smaller vortex core for a given initial duct geometry. As the initial area of the vortex decreases for a given initial duct area, more room exists for the core to expand, allowing the centerline velocity to approach zero, and increasing the potential for recirculation zone formation. This result is consistent with the results of Darmofal, *et al*[24].

Turning to the effect of inter-stream mixing, it can be seen from Table 2.2 that no regions exist where the trends change due to mixing. Therefore, the addition of mixing only modifies the shape of the various flow regimes. Figure 2-5 shows two flow regime maps for a high swirl ($\Omega = 1.5$), high heat release ($\phi_1 = \phi_2 = 0.8$) case with different mixing rates. The mixing rate for Figure 2-5a was chosen to be equal to that predicted by the planar shear layer growth rate of Hermanson and Dimotakis[30], and the mixing rate for Figure 2-5b was chosen to be ten times that mixing rate.

Comparing Figures 2-4b and 2-5a, there is little difference between the no mixing case and the low mixing case. Comparing Figures 2-5a and b, one sees that the shape of the regions has been

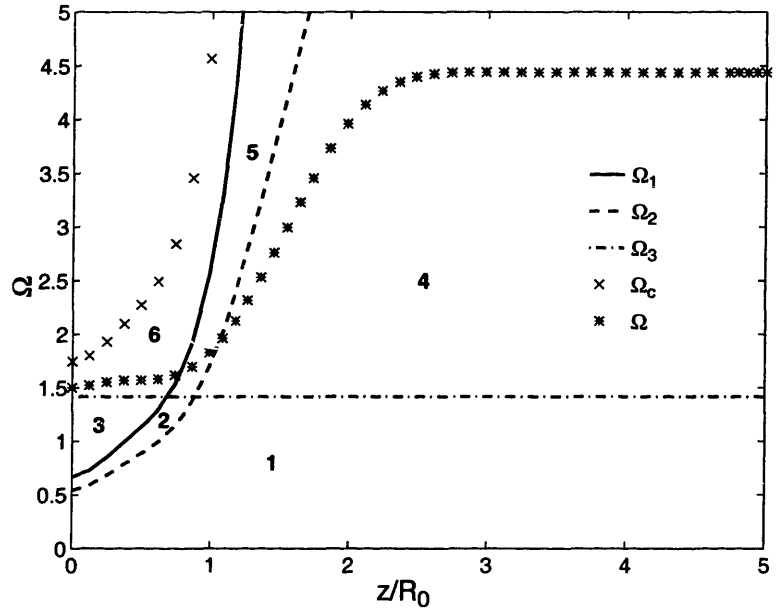

a)

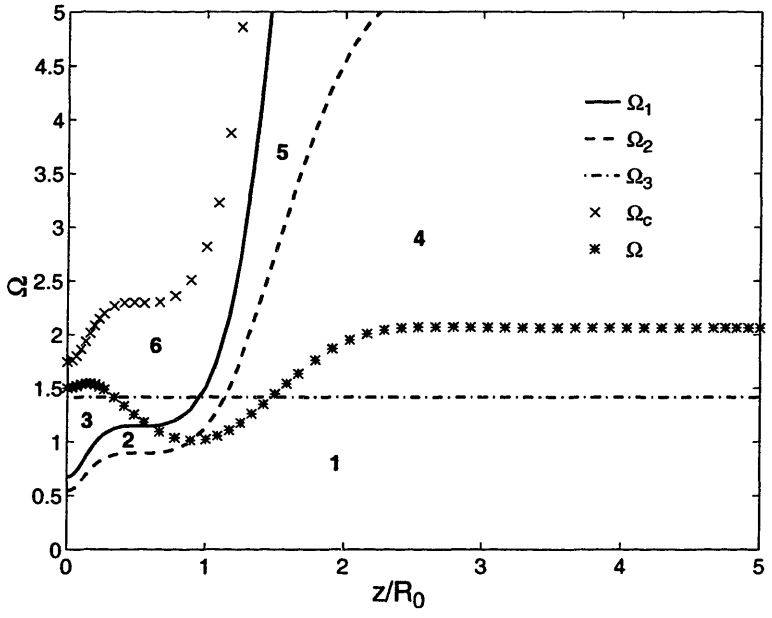

b)

Figure 2-4: Flow regime maps for high swirl ($\Omega_0 = 1.5$) with a) low heat release ($\phi_1 = \phi_2 = 0.2$) and b) high heat release ($\phi_1 = \phi_2 = 0.8$).

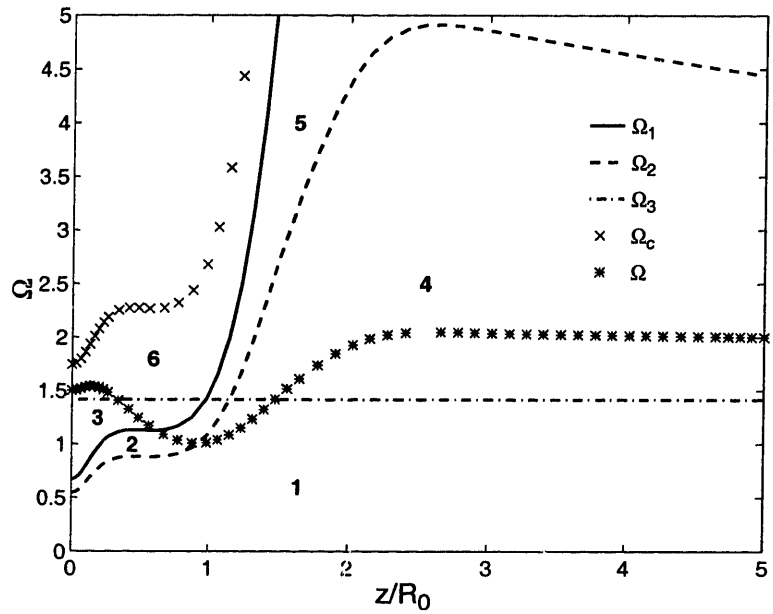

a)

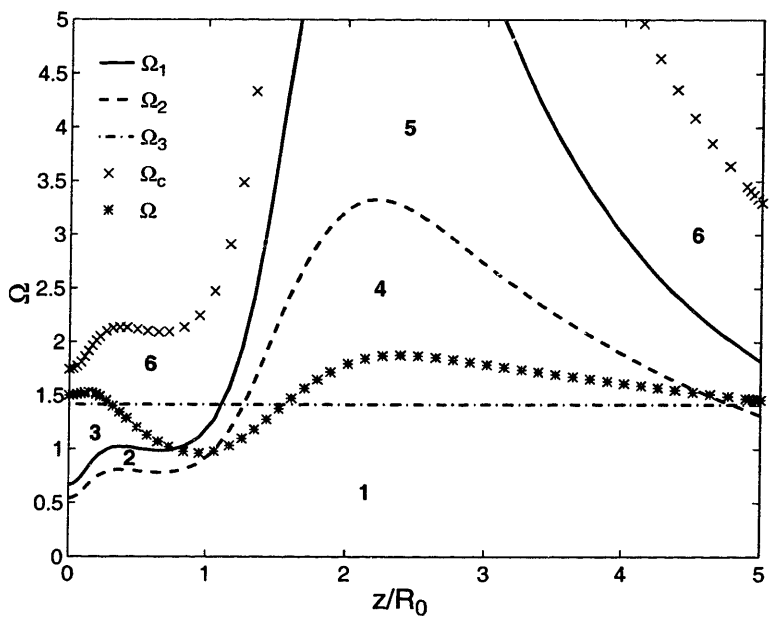

b)

Figure 2-5: Flow regime maps for high swirl ($\Omega_0 = 1.5$) and high heat release ($\phi_1 = \phi_2 = 0.8$) with a) low mixing rate (ν_t) and b) high mixing rate ($10\nu_t$).

Table 2.4: Conditions for the low swirl cases of Figure 2-6.

Inlet Parameter	Value
Swirl Ratio, Ω_0	0.4
Velocity Ratio, r_0	0.8
Density Ratio, s_0	1
Area Ratio, α_0	4

altered for the high mixing rate case, but the overall effect on the solution is small. Therefore, mixing does not change the parametric flow behavior.

Additional flow maps for a low swirl case with varying heat release and mixing are presented in Figures 2-6 and 2-7. Figure 2-6a shows the results from a low swirl ($\Omega_0 = 0.4$), low heat release ($\phi_1 = \phi_2 = 0.2$) case, while Figure 2-6b shows the results from a low swirl, high heat release ($\phi_1 = \phi_2 = 0.8$) case. The values of the inlet parameters for these runs are given in Table 2.4.

Examining Figure 2-6, it is seen that for this low swirl case, the quasi 1-D solution lies entirely in region 1 for both low and high heat release. In region 1, the trends are the same as for the zero swirl case. Therefore, there exists an inlet swirl ratio below which the zero inter-stream mixing quasi 1-D case will exhibit the same general behavior as the zero swirl case.

Figure 2-7 shows two flow regime maps for a low swirl ($\Omega_0 = 0.4$), high heat release ($\phi_1 = \phi_2 = 0.8$) case with different mixing rates. As was done for the high swirl case of Figure 2-5, the mixing rate for Figure 2-7a was chosen to be equal to that predicted by the planar shear layer growth rate of Hermanson and Dimotakis. The mixing rate for Figure 2-7b was chosen to be ten times that mixing rate.

Comparing Figures 2-6b and 2-7a, there is little difference between the no mixing case and the low mixing case. Comparing Figures 2-7a and b, one sees that the shape of the regions has been altered for the high mixing rate case, but once again, the overall effect on the quasi 1-D solution is small. Therefore, as was found for the high swirl case, mixing does not change the parametric behavior for the low swirl case.

A case for a typical lean-premixed gas turbine geometry and operating condition was run with the quasi 1-D model. As noted before, the analysis cannot be used to address a recirculating case, but the solution may be obtained up to the point of recirculation zone formation. Figure 2-8 shows this on a flow regime map. The conditions are for a typical geometry with swirl ratio of $\Omega_0 = 1.0$ and heat release of $\phi_1 = \phi_2 = 0.55$. Due to the high swirl and high divergence of the walls, the local swirl ratio reaches the critical swirl ratio at $z/R_0 = 1.3$. The local swirl ratio starts in region 3 which is the high swirl regime with respect to heat release. The solution crosses Ω_1 briefly, and then climbs back above the threshold again. Therefore, at a typical gas turbine operating point, the flow regime map says that before the recirculation zone forms, adding heat to the flow will bring the

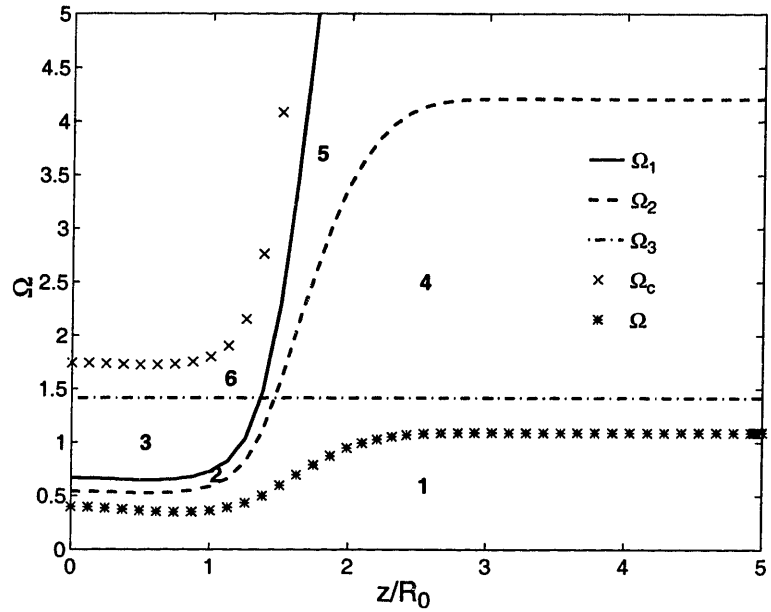

a)

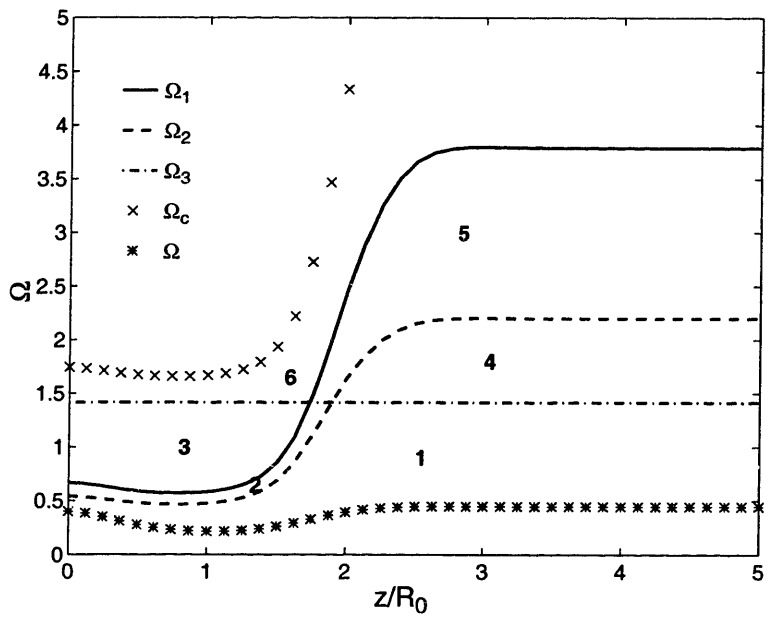

b)

Figure 2-6: Flow regime maps for low swirl ($\Omega_0 = 0.4$) with a) low heat release ($\phi_1 = \phi_2 = 0.2$) and b) high heat release ($\phi_1 = \phi_2 = 0.8$).

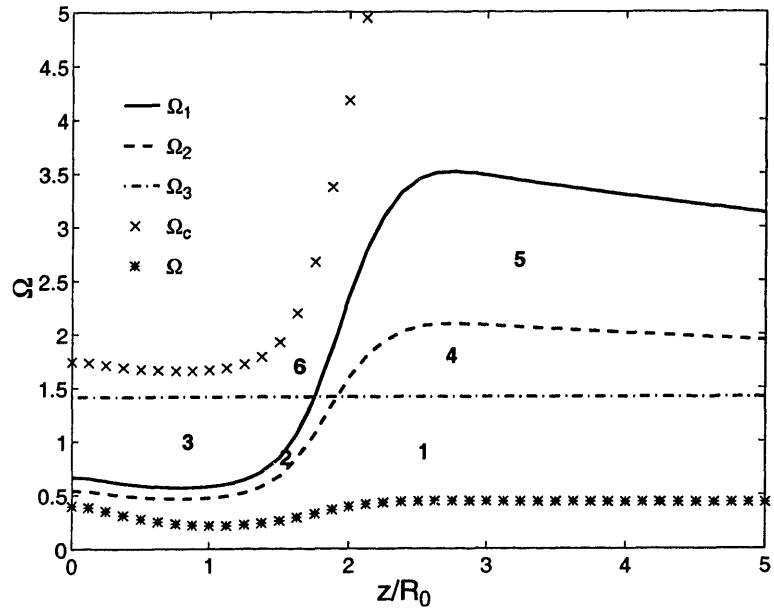

a)

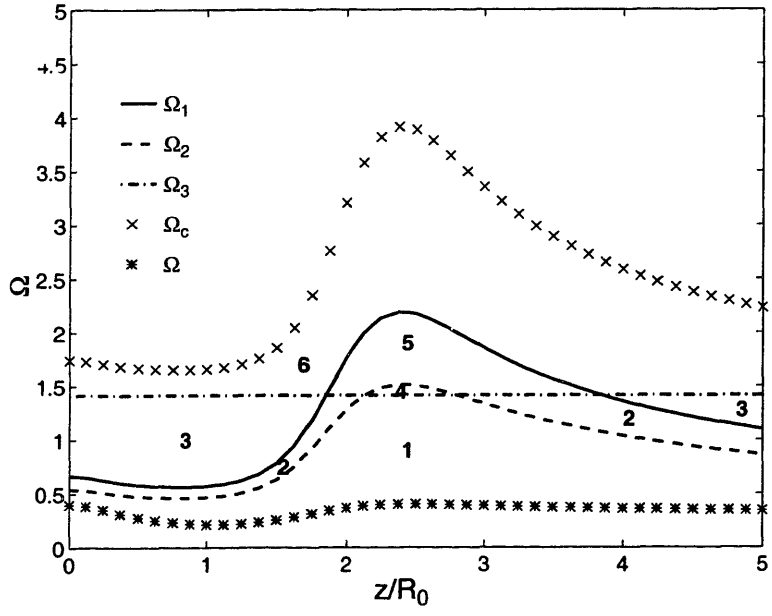

b)

Figure 2-7: Flow regime maps for low swirl ($\Omega_0 = 0.4$) and high heat release ($\phi_1 = \phi_2 = 0.8$) with a) low mixing rate (ν_t) and b) high mixing rate ($10\nu_t$).

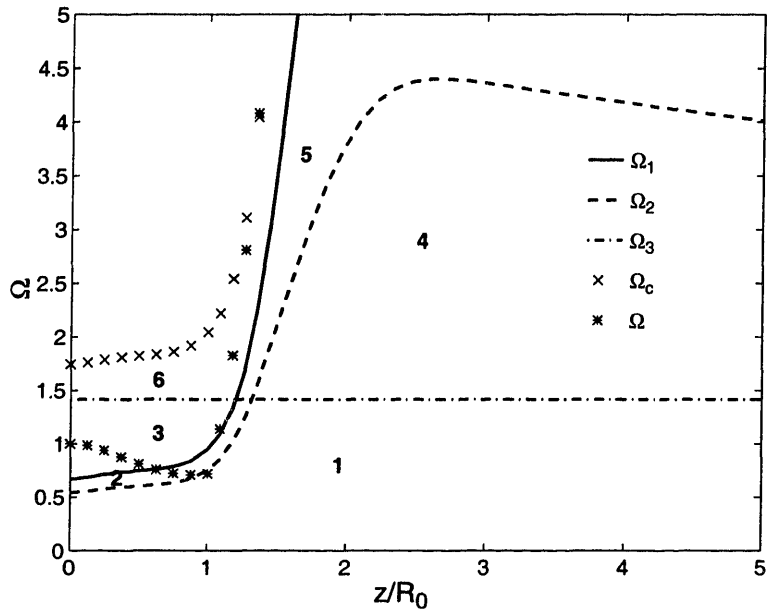

Figure 2-8: Flow regime map for a typical gas turbine combustor operating point, $\Omega_0 = 1.0$, $\phi_1 = \phi_2 = 0.55$.

flow closer to recirculating.

The flow regime maps presented in Figures 2-4 through 2-7 show that although the influence coefficient analysis yields local trends only, these trends can be shown in a global context. Flow regime maps provide a useful tool for viewing regions of differing flow behavior and their relation to the local swirl ratio at a given point in the duct.

Chapter 3

Quasi 1-D Control Volume Model With Recirculation (CFLOW)

The quasi 1-D control volume model with recirculation (CFLOW) is based on the previous quasi 1-D formulation described in Chapter 2. However, the model has been made more general in several respects. It also employs an implicit solver using a Newton method, where the previous solver was explicit. This was necessary due to the elliptic nature of the problem. Use of a Newton method was chosen to facilitate incorporation of the model into an optimization routine in the future and to enable detailed sensitivity studies as will be discussed in Section 3.5.

The chapter begins with a description of the assumptions and their implications in Section 3.1, followed by a discussion of the governing equations in Section 3.2. Section 3.3 describes the solver, while Section 3.4 presents the results from the model. A discussion of the sensitivity study is presented in Section 3.5 along with some instructive results. Section 3.6 describes the extension of the model to handle radial jet injection at the wall, while the limitations of the model are discussed in Section 3.7.

3.1 Assumptions

As stated previously, several assumptions made for the quasi 1-D model without recirculation have been discarded, allowing for a more general treatment of the flowfield of interest. The mass exchange between streams was assumed to be equal and opposite in the previous formulation. This assumption has been relaxed, allowing for mass to accumulate or deplete within a control volume. This allows a control volume to completely close if enough mass is removed, thus making it possible to model the closing of a recirculation zone. The interface between control volumes is thus not a streamline as before, but rather the line of maximum shear stress. It also implies that circulation is not

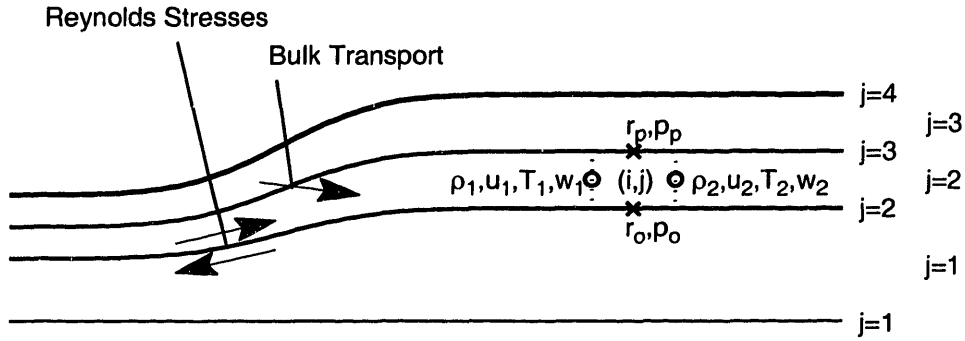

Figure 3-1: Schematic of a three stream CFLOW case. Mixing due to Reynolds stresses and bulk transport is shown. Cell-face (o) and cell-edge (x) quantities shown for cell (i,j). Ordering of control volumes and edges is indicated along right side.

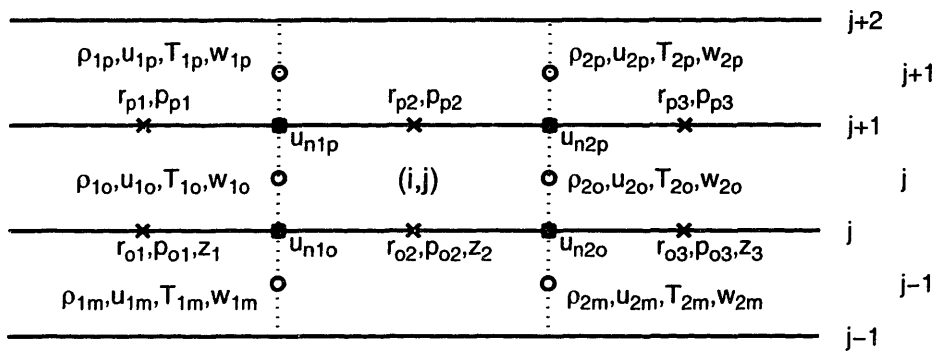

Figure 3-2: Discretization of conservation equations. Cell-face (o) and cell-edge (x) quantities shown for cell (i,j). Ordering of control volumes and edges is indicated along right side.

conserved within a stream, as was previously assumed. This necessitates an additional variable to track circulation which for this analysis was swirl velocity. The additional variable makes it necessary to include a tangential momentum equation which takes account of the tangential shear stress at the interface between control volumes. The allowance for mass depletion in a stream also provides for the possibility of negative axial velocities within a stream. Thus, a recirculating flow may be modeled.

3.2 Governing Equations

Applying conservation of mass, momentum, and energy, as well as the state equation yields the following system of equations. Figure 3-1 shows a schematic of this quasi 1-D model for a three stream case. Density (ρ), axial velocity (u), temperature (T), and tangential velocity (w) are defined constant within a control volume (denoted by o) with a possible discontinuity across the interface. In contrast, radius (r) and pressure (p) are defined on the interface (denoted by x), and vary across the interior of a control volume.

The subscripting scheme in Figures 3-1 and 3-2 uses numbers to refer to the axial direction and letters to refer to the radial direction. The numbers increase in the downstream direction, and the letters increase in the radially outward direction. The equations are developed to represent the flow in cell (i,j). Figure 3-2 shows the discretization used to write the conservation equations for cell (i,j). The ordering on the right side of Figures 3-1 and 3-2 shows how the control volumes and their edges are numbered. To avoid $1/r$ singularities at $r = 0$, a small non-zero radius is specified on the centerline. For these studies, the centerline of the duct occurred at $r_\epsilon = 10^{-5}$.

The duct radius was specified to be the same as the quasi 1-D model without recirculation for comparisons to the quasi 1-D and axisymmetric Navier-Stokes solutions in Chapter 5. This geometry is specified by Equation 2.12. Heat release profiles, $dh_{pr_i}(z)$, were also the same as in the quasi 1-D model without recirculation. These profiles are given by Equation 2.14. Figure 2-2 shows these profiles schematically.

3.2.1 Continuity

The continuity equation for cell (i,j) is

$$\rho_{2o} u_{2o} A_{2o} - \rho_{1o} u_{1o} A_{1o} = \tilde{m}_o - \tilde{m}_p, \tag{3.1}$$

where $\tilde{m}_o$ and $\tilde{m}_p$ are the mass transport across the j and $j+1$ control volume edges, respectively. The bulk transport of mass, momentum, and energy is defined as positive in the radially outward direction (*i.e.*, $\tilde{m}_o$ is positive if mass is transported from control volume $j-1$ to control volume j). Expressions for the bulk transport terms will be developed after presentation of the conservation equations.

The areas A_{2o} and A_{1o} are defined as the cell face areas. These areas are computed using the average radius at the cell face, thus

$$A_{1o} = \frac{1}{4}\pi \left[(r_{p2} + r_{p1})^2 - (r_{o2} + r_{o1})^2 \right], \tag{3.2}$$

$$A_{2o} = \frac{1}{4}\pi \left[(r_{p3} + r_{p2})^2 - (r_{o3} + r_{o2})^2 \right]. \tag{3.3}$$

3.2.2 Axial Momentum

The axial momentum equation for cell (i,j) is

$$(\rho_{2o}{u_{2o}}^2 + p_{2o})A_{2o} - (\rho_{1o}{u_{1o}}^2 + p_{1o})A_{1o} - p_{p2}\Delta A_p + p_{o2}\Delta A_o = M_{xo} - M_{xp} + \tilde{M}_o - \tilde{M}_p. \quad (3.4)$$

The pressures p_{2o} and p_{1o} are defined as $\rho_{2o}R_{2o}T_{2o}$ and $\rho_{1o}R_{1o}T_{1o}$, respectively. The other pressure terms are a result of the swirl-induced radial pressure gradient. The area changes ΔA_o and ΔA_p are defined as the areas over which these swirl-induced pressures act. They are computed by

$$\Delta A_o = \frac{1}{4}\pi\left[(r_{o3} + r_{o2})^2 - (r_{o2} + r_{o1})^2\right], \quad (3.5)$$

$$\Delta A_p = \frac{1}{4}\pi\left[(r_{p3} + r_{p2})^2 - (r_{p2} + r_{p1})^2\right]. \quad (3.6)$$

The bulk transport terms $\tilde{M}_o$ and $\tilde{M}_p$ represent the flux of axial momentum across the j and $j+1$ control volume edges, respectively. The terms M_{xo} and M_{xp} represent the transfer of axial momentum due to viscous and Reynolds stresses at the j and $j+1$ control volume interfaces. Axial shear stresses acting on cell (i,j) at the j control volume edge are defined as positive if the axial velocity of control volume $j-1$ is greater than the axial velocity of control volume j. Expressions for these mixing terms will be developed after presentation of the conservation equations.

3.2.3 Tangential Momentum

The tangential momentum equation for cell (i,j) is

$$\rho_{2o}u_{2o}A_{2o}w_{2o}r_2 - \rho_{1o}u_{1o}A_{1o}w_{1o}r_1 = T_{ro} - T_{rp} + \tilde{T}_o - \tilde{T}_p, \quad (3.7)$$

where A_{1o} and A_{2o} are given by Equations 3.2 and 3.3, and where r_1 and r_2 are the average radii of the cell faces. These are given by

$$r_1 = \frac{1}{4}(r_{o1} + r_{p1} + r_{o2} + r_{p2}), \quad (3.8)$$

$$r_2 = \frac{1}{4}(r_{o2} + r_{p2} + r_{o3} + r_{p3}). \quad (3.9)$$

The bulk transport terms $\tilde{T}_o$ and $\tilde{T}_p$ represent the tangential momentum transport across the j and $j+1$ control volume edges, respectively. The terms T_{ro} and T_{rp} represent the transfer of tangential momentum due to Reynolds stresses at the j and $j+1$ control volume interfaces. Tangential shear stresses acting on cell (i,j) at the j control volume edge are defined as positive if the tangential velocity of control volume $j-1$ is greater than the tangential velocity of control volume j. Expressions for these mixing terms will be developed after presentation of the conservation equations.

3.2.4 Radial Momentum

The radial momentum equation for cell (i,j) is

$$\rho_{2o}u_{2o}A_{2o}v_{2o} - \rho_{1o}u_{1o}A_{1o}v_{1o} + p_{p2}A_p - p_{o2}A_o - \frac{1}{2}\left(\rho_{2o}{w_{2o}}^2 + \rho_{1o}{w_{1o}}^2\right)\Delta A = 0, \tag{3.10}$$

where v_{1o} and v_{2o} are computed as the approximate radial velocities and given by

$$v_{1o} = u_{1o}\frac{dr_1}{dz_1} - \frac{1}{2}(u_{n1o} + u_{n1p}), \tag{3.11}$$

$$v_{2o} = u_{2o}\frac{dr_2}{dz_2} - \frac{1}{2}(u_{n2o} + u_{n2p}). \tag{3.12}$$

The dr/dz terms represent the expansion of a control volume and are defined as

$$\frac{dr_1}{dz_1} = \frac{\frac{1}{2}(r_{o2} + r_{p2} - r_{o1} - r_{p1})}{z_2 - z_1}, \tag{3.13}$$

$$\frac{dr_2}{dz_2} = \frac{\frac{1}{2}(r_{o3} + r_{p3} - r_{o2} - r_{p2})}{z_3 - z_2}. \tag{3.14}$$

The additional term in Equations 3.11 and 3.12 is the average radial velocity associated with the bulk transport of mass across the control volume edges in the plane of a cell face. An expression for u_n will be developed after presentation of the conservation equations.

The remainder of the radial momentum equation represents the radial equilibrium terms (*i.e.*, $dp/dr = \rho w^2/r$). The area terms A_o, A_p, and ΔA are given by

$$A_o = \frac{1}{4}\pi(r_{o1} + 2r_{o2} + r_{o3})(z_3 - z_1), \tag{3.15}$$

$$A_p = \frac{1}{4}\pi(r_{p1} + 2r_{p2} + r_{p3})(z_3 - z_1), \tag{3.16}$$

$$\Delta A = \pi(r_{p2} - r_{o2})(z_3 - z_1). \tag{3.17}$$

3.2.5 Energy

The energy equation for cell (i, j) is

$$\begin{aligned}
&\left(C_{p_{2o}}T_{2o} + \frac{1}{2}{u_{2o}}^2 + \frac{1}{2}{v_{2o}}^2 + \frac{1}{2}{w_{2o}}^2 - h_{pr_{2o}}\right)\rho_{2o}u_{2o}A_{2o} \\
&- \left(C_{p_{1o}}T_{1o} + \frac{1}{2}{u_{1o}}^2 + \frac{1}{2}{v_{1o}}^2 + \frac{1}{2}{w_{1o}}^2 - h_{pr_{1o}}\right)\rho_{1o}u_{1o}A_{1o}, \\
&= H_{to} - H_{tp} + H_{xo} - H_{xp} + H_{ro} - H_{rp} + \tilde{H}_o - \tilde{H}_p
\end{aligned} \tag{3.18}$$

where the chemical source term is denoted by h_{pr} and modeled as previously described in Section 2.2. The bulk transport terms $\tilde{H}_o$ and $\tilde{H}_p$ represent the energy transport across the j and $j+1$ control volume edges, respectively. The terms H_{xo}, H_{xp}, H_{ro}, and H_{rp} represent the transfer of energy due to shear work done by the axial and tangential Reynolds stresses at the j and $j+1$ control volume interfaces. Sign conventions for the shear work terms are the same as for their shear stress counterparts in the axial and tangential momentum equations. The terms H_{to} and H_{tp} represent the transfer of energy due to conduction at the j and $j+1$ control volume interfaces. Conduction terms for cell (i, j) at the j control volume edge are defined as positive if the temperature of control volume $j-1$ is greater than the temperature of control volume j. Expressions for these mixing terms will be developed after presentation of the conservation equations.

3.2.6 State

The state equation for cell (i, j) is

$$p_{2o} + p_{1o} - p_{p2} - p_{o2} = 0, \tag{3.19}$$

where the pressures p_{2o} and p_{1o} are again defined as $\rho_{2o}R_{2o}T_{2o}$ and $\rho_{1o}R_{1o}T_{1o}$, respectively.

3.2.7 Bulk Transport

The bulk transport terms for control volume edge j in cell (i,j) are defined here. Construction of transport terms for the $j+1$ control volume edge can be constructed in a similar fashion. The bulk transport of mass across a control volume interface can be defined in terms of an implied normal velocity at the interface (*i.e.*, the normal velocity at the shear layer centerline)

$$\tilde{m}_o = C_m \bar{\rho}_o u_{n1o}\, dA_o, \tag{3.20}$$

where dA_0 is the area of the interface along the j edge

$$dA_o = \pi(r_{o3} + r_{o2})(z_3 - z_2), \tag{3.21}$$

and where $\bar{\rho}_o$ is defined as

$$\bar{\rho}_o = \frac{1}{2}(\rho_{1m} + \rho_{1o}). \tag{3.22}$$

The normal velocity is given by

$$u_{n1o} = C_{dif}\frac{1}{4}(u_{1o} + u_{1m})\left[\frac{1}{u_{1o}} + \frac{1}{u_{1m}}\right] v_{D1o}, \tag{3.23}$$

where v_{D1o} is the average normal velocity across the shear layer and is given by

$$v_{D1o} = s\,C_1\sqrt{{u_{dif}}^2 + {w_{dif}}^2 + k_l\left(\frac{\nu_l}{r_{ref}}\right)^2}. \tag{3.24}$$

The last term in the radical is a small, non-zero laminar mixing term needed to prevent the Newton matrix from becoming singular. In Equation 3.24, u_{dif} and w_{dif} are defined as

$$u_{dif} = u_{1m} - u_{1o}, \tag{3.25}$$

$$w_{dif} = w_{1m} - w_{1o}, \tag{3.26}$$

$$\tag{3.27}$$

and s is the sign of either u_{dif} or w_{dif} as given by

$$s = \begin{cases} sign(u_{dif}) & |u_{dif}| \geq |w_{dif}| \\ \\ sign(w_{dif}) & |u_{dif}| < |w_{dif}| \end{cases} . \tag{3.28}$$

The value of C_{dif} in Equation 3.23 is specified by the user. It is parameterized as a multiple of the mixing given by the planar shear layer growth rate of Hermanson and Dimotakis[30], described in Section 2.2 (*e.g.*, $C_{dif} = 10$ corresponds to 10 times the mixing in a planar shear layer). The constant C_1 in Equation 3.24 is found by assuming an error function for the axial velocity profile across the shear layer and using the 5% and 95% points to compute C_1, yielding a value of $C_1 = 0.092$, as in Section 2.2. The coefficient C_m in Equation 3.20 is a function of the control volume areas above and below the control volume interface, denoted as A_u and A_l, respectively. It enables the mass transport across a control volume interface to be reduced to zero smoothly, an important step in capturing the closure of a recirculation zone as described in Section 3.2.9. The function C_m is described by

$$C_m = \frac{1 - \exp(-C_e C_f)}{1 - \exp(-C_e)}, \tag{3.29}$$

where C_f is given by

$$C_f = \frac{2A_u A_l}{{A_u}^2 + {A_l}^2}, \tag{3.30}$$

and where $C_e = 0.1$ has been chosen to give the desired profile. The areas A_u and A_l are defined as

$$A_u = \pi \left({r_{p2}}^2 - {r_{o2}}^2 \right), \tag{3.31}$$

$$A_l = \pi \left({r_{o2}}^2 - {r_{m2}}^2 \right). \tag{3.32}$$

The bulk axial momentum exchange ($\tilde{M}_o$) is

$$\tilde{M}_o = \bar{u}\tilde{m}_o, \tag{3.33}$$

where $\bar{u}$ is the average axial velocity of the adjacent control volumes, $(u_{1m} + u_{1o})/2$. The bulk tangential momentum exchange ($\tilde{T}_o$) is

$$\tilde{T}_o = \bar{w}\tilde{m}_o, \tag{3.34}$$

where $\bar{w}$ is the average tangential velocity of the adjacent control volumes, $(w_{1m} + w_{1o})/2$. The bulk enthalpy exchange ($\tilde{H}_o$) is

$$\tilde{H}_o = \bar{H}\tilde{m}_o, \tag{3.35}$$

where $\bar{H}$ is the average energy of the adjacent control volumes, given by

$$\bar{H} = \frac{1}{2}C_{p_{1o}}(T_{1m} + T_{1o}) + \frac{1}{2}({u_{1m}}^2 + {u_{1o}}^2) + \frac{1}{2}({v_{1m}}^2 + {v_{1o}}^2) + \frac{1}{2}({w_{1m}}^2 + {w_{1o}}^2). \tag{3.36}$$

3.2.8 Diffusion and Conduction

The diffusion and conduction terms for control volume edge j in cell (i, j) are defined here. Construction of terms for the $j + 1$ control volume edge can be constructed in a similar fashion.

The diffusion terms in the axial momentum equation (Equation 3.4) are due to axial shear stresses (M_x). An implied diffusion mass flow can be defined as

$$\dot{m}_{do} = C_d \bar{\rho}_o u_{n1o}\, dA_o, \tag{3.37}$$

where dA_o and $\bar{\rho}_o$ are defined as before in Equations 3.21 and 3.22. The coefficient C_d is a function of the control volume areas above and below the control volume interface. It enables the diffusion due to Reynolds stresses across a control volume interface to be increased smoothly, an important

step in capturing the closure of a recirculation zone as described in Section 3.2.9. The function is related to the coefficient C_m in Equation 3.29 by

$$C_d = \frac{1}{C_m}. \tag{3.38}$$

The diffusion term in the axial momentum equation is then

$$M_{xo} = u_{dif}\dot{m}_{do}, \tag{3.39}$$

where u_{dif} is defined as before in Equation 3.27.

The diffusion term in the tangential momentum equation (Equation 3.7) is due to tangential shear stresses and is given by

$$T_{ro} = w_{dif}\dot{m}_{do}, \tag{3.40}$$

where w_{dif} is defined as before in Equation 3.27.

The energy equation (Equation 3.19) contains two diffusion terms and one conduction term. They represent heat conduction between control volumes (H_t), shear work due to axial shear stresses (H_x), and shear work due to tangential shear stresses (H_r). The conduction term is given by

$$H_{to} = T_{dif}\dot{m}_{do}, \tag{3.41}$$

where T_{dif} is a function of the temperatures above and below the control volume interface, T_{1o} and T_{1m}, respectively and is given by

$$T_{dif} = \frac{C_{p_{1c}}}{Pr_t}(T_{1m} - T_{1o}). \tag{3.42}$$

The shear work terms are given by

$$H_{xo} = \frac{1}{2}u_{dif}M_{xo}, \tag{3.43}$$

$$H_{ro} = \frac{1}{2} w_{dif} T_{ro}. \tag{3.44}$$

3.2.9 Recirculation Zone Closure

Recirculation zone closure is obtained due to mass transport across control volume interfaces. The function C_m defined in Equation 3.29 is used to smoothly reduce the mass exchange between control volumes as the area of the recirculating control volume becomes small relative to the adjacent control volume area. Concurrently, the diffusion terms are smoothly increased by the function C_d in Equation 3.38. This allows the smaller control volume to be linked to the larger adjacent control volume, thus creating one stream from two.

3.2.10 Boundary Conditions

Boundary conditions for the inner and outer boundaries as well as the inlet and outlet planes are specified as follows. The inner radius is set to a small, non-zero value in order to avoid $1/r$ singularities at $r = 0$. The inner radius was specified as $r_\epsilon = 10^{-5}$. The outer radius was specified as the outer wall radius. Residuals were constructed as cell-centered quantities, therefore, J control volume edges exist, but only $J-1$ control volumes. The extra face variables (ρ, u, T, w) at J outside the duct wall were represented by a set of dummy face variables, resulting in continuity, axial and tangential momentum, and energy residuals that are zero by definition. Additionally, mass transport across the J control volume edge was set to zero due to zero normal velocity at the wall. Shear stresses were set based on zero axial and tangential velocities above the J edge, and conduction was set to zero due to equal temperatures above and below the J control volume edge.

For the inflow boundary conditions, the residuals for mass, axial momentum, energy, and tangential momentum were set to allow the inlet conditions to change. This was done done by setting the new values of the residuals to the difference between the old values and the new inlet conditions. The residuals for radial momentum and pressure were set to zero.

For the outflow boundary conditions, the residuals for mass, axial momentum, energy, and tangential momentum were set to zero due to these cell-centered residuals lying downstream of the exit plane. A zero slope boundary condition was applied to the radial momentum equation, *i.e.*, the slope of the control volume interfaces was zero at the outflow plane. The residual on the state equation (*i.e.*, the pressure) was set to zero.

3.3 Solver

Due to the elliptic nature of a recirculating flowfield, Equations 3.1-3.19 are solved using a Newton method. The state at the inlet is specified, along with the heat release profile for each stream, the global mixing coefficient (C_{dif}), and the duct geometry. The solver iterates until a converged solution is reached. Computation time is on the order of one minute.

The first step in the solution process is setting up the Newton matrix. This involves discretizing the conservation equations and placing the terms in their proper positions inside the Newton matrix. Since the problem is elliptic, the entire flowfield is set up at once. The Newton matrix represents the partial derivatives of the conservation equations with respect to the state variables (*i.e.*, the Jacobian). The system to be solved is

$$\frac{\partial R}{\partial U}\delta U = \delta R, \tag{3.45}$$

where U is the state vector and R is the residual vector. Details of the Newton matrix are discussed in Appendix B.

Once the Newton matrix has been set up, the system is solved for the state vector change using a tri-diagonal block solver. The change in the solution is relaxed, and the value of the state vector is updated. Iteration continues until the maximum change in the state vector is below a specified tolerance, typically set at 10^{-10}.

3.4 Results from CFLOW

Recirculation zone volume was determined to be the metric for evaluating the performance of CFLOW. This choice was driven by a need for accurate estimates of recirculation zone volume in a PFR/PSR combustor model (a network of plug flow and perfectly stirred reactors).

Figures 3-3 and 3-4 show the computed recirculation zone sizes for a combustor with high swirl ($\Omega = 1.0$). The combustor is a constant area axisymmetric duct with an inner and an outer rearward-facing step at the inlet plane. Figure 3-3 shows a combustor flow with no heat release, while Figure 3-4 shows the recirculation zone boundaries (*i.e.*, the lines of maximum shear stress) for a combustor at typical heat release ($\phi = 0.55$). These are the same conditions used to compute the flow regime map of Figure 2-8 for a typical gas turbine combustor, and are also the conditions for 3-D Navier-Stokes computations of a lean-premixed combustor discussed in Chapter 6. The heat release profile was determined from the Navier-Stokes solutions and used as an input to CFLOW. The mixing coefficient was set to an empirically determined value of $\Xi = 4.0\nu_t$ as described in Section 5.3.

These cases were chosen to be representative of a lean-premixed combustor for cold and hot

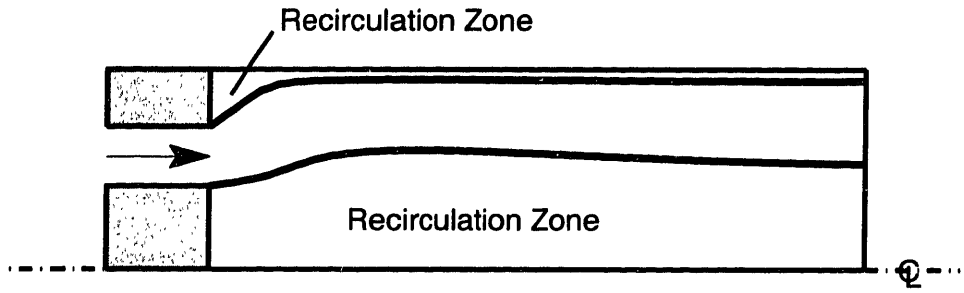

Figure 3-3: Recirculation zone boundaries computed by CFLOW for a lean-premixed combustor at high swirl ($\Omega = 1.0$) and zero heat release ($\phi = 0.0$).

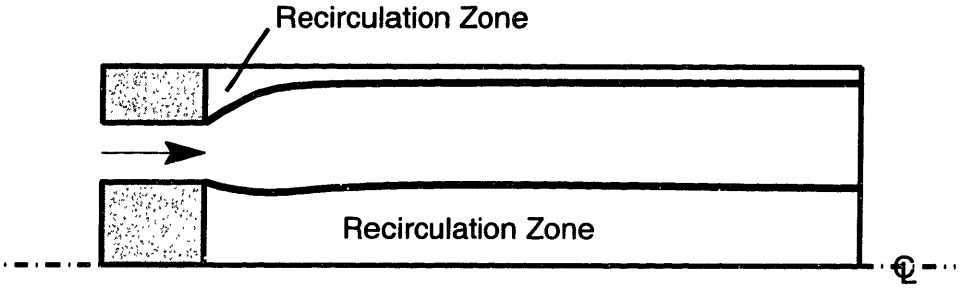

Figure 3-4: Recirculation zone boundaries computed by CFLOW for a lean-premixed combustor at high swirl ($\Omega = 1.0$) and typical heat release ($\phi = 0.55$).

flows. A centerbody is present on the centerline of the duct, causing the immediate formation of a recirculation zone. Figure 2-8 showed that the swirl ratio for the hot flow should be such that the effect of heat addition causes the recirculation zone to grow. However, in the case of Figures 3-3 and 3-4, the recirculation zone decreases. This is caused by the presence of the centerbody which necessitates that zero axial velocity be specified at the inlet for the innermost stream. This causes the inlet swirl ratio defined in terms of the influence coefficients to approach infinity at the inlet, exceeding the critical swirl ratio. Since the influence coefficient trends are valid only in regions of the flow where the swirl ratio is below the critical swirl ratio, the influence coefficient trends may not be valid for flows where a recirculation zone is set up at the inlet by a rearward-facing step. In this case, a more appropriate tool for determining trends is the sensitivity analysis discussed next in Section 3.5.

Comparison of these results with a 3-D Navier-Stokes solution in Chapter 6 will show that the recirculation zone volumes computed by CFLOW are within 20% of those given by the 3-D code.

3.5 Sensitivity Study

Use of a Newton solver, as described in Section 3.3 and Appendix B, enabled a detailed sensitivity study of CFLOW to be performed. In particular, three sensitivities can be computed for each run.

The sensitivities are described, as is their formulation. Following this is a presentation of some instructive results from the sensitivity analysis.

The first of the sensitivities that can be computed is the sensitivity of an objective function to the user-specified variables available in the code. For the present work, the primary objective function is the inner recirculation zone volume. The user-specified variables in CFLOW that have been examined are mixing coefficient and magnitude of the heat release. The sensitivity is a single number for the flowfield, computed given inlet and boundary conditions. As a result, the effect of modeling error in mixing or heat release on a quantity of interest (*i.e.*, inner recirculation zone volume) can be calculated each time CFLOW is run.

The second sensitivity is the sensitivity of an objective function to changes in a residual, as specified by one of the six equations being solved. These values are obtained as a function of axial and radial location, so that a contour map of these local sensitivities can be constructed for each run. This information could be used in two different ways. First, it can point to areas where errors in the modeling of source terms in the conservation equations could have a relatively large (or small) impact on a figure of merit (*i.e.*, inner recirculation zone volume). It can also point to areas where one might be able to affect the objective function by adding a source of some sort. For example, it could point to a region where adding radial momentum, perhaps through use of dilution jets at the wall, could have the most impact on recirculation zone volume.

The third sensitivity gives the effect of changes in the user-specified variables available in the code on the state variables. These values are obtained locally as the previous sensitivity was. Results can point to areas where modeling errors in mixing or heat release could affect the state variables the most (or the least). It could also point to areas where adding mixing or heat could have the greatest impact on the flow variables.

3.5.1 Formulation

Given a system analysis in the form

$$R(U, \alpha) = 0, \tag{3.46}$$

where R is the residual for the system, U is the state vector determined by solving $R = 0$, and α is the geometric and modeling parameters, U can be solved for using a Newton approach

$$\begin{aligned} R(U^{n+1}, \alpha) &= R(U^n + \Delta U, \alpha) \\ &\approx R(U^n, \alpha) + \frac{\partial R}{\partial U}\Delta U = 0. \end{aligned} \tag{3.47}$$

This is the solution method used in CFLOW to solve for the state vector. Solving the above equation yields

$$\Delta U = -\left(\frac{\partial R}{\partial U}\right)^{-1} R(U^n). \tag{3.48}$$

Given a change in geometry or modeling parameters, $\Delta\alpha$, the solution changes such that

$$R(U + \Delta U, \alpha + \Delta\alpha) \approx \frac{\partial R}{\partial U}\Delta U + \frac{\partial R}{\partial \alpha}\Delta\alpha = 0. \tag{3.49}$$

Solving for ΔU

$$\Delta U = -\left(\frac{\partial R}{\partial U}\right)^{-1} \frac{\partial R}{\partial \alpha}\Delta\alpha, \tag{3.50}$$

which is the third sensitivity listed above. Rewriting this slightly, we see that this is indeed the sensitivity of the state variables to changes in user-specified variables

$$\frac{dU}{d\alpha} = -\left(\frac{\partial R}{\partial U}\right)^{-1} \frac{\partial R}{\partial \alpha}. \tag{3.51}$$

Looking at the impact on a system metric, f, gives the first sensitivity listed above (*i.e.*, the sensitivity of an objective function to a change in a user-specified variable)

$$\Delta f = \frac{\partial f}{\partial U}\Delta U + \frac{\partial f}{\partial \alpha}\Delta\alpha, \tag{3.52}$$

or

$$\frac{df}{d\alpha} = -\psi^T \frac{\partial R}{\partial \alpha} + \frac{\partial f}{\partial \alpha}, \tag{3.53}$$

where ψ is the adjoint matrix satisfying

$$\frac{\partial R}{\partial U}^T \psi = \frac{\partial f}{\partial U}^T. \tag{3.54}$$

Table 3.1: Sensitivity of recirculation zone volume to mixing coefficient and heat release for the cases presented in Figures 3-3 and 3-4.

	$\Omega = 1.0, \phi = 0.0$	$\Omega = 1.0, \phi = 0.55$
$\partial f / \partial C_{dif}$	-2.4E-3	-1.2E-3
$\partial f / \partial h_{pr}$	-1.8E-4	-6.8E-4

Examining ψ further, it is seen that the adjoint is the second sensitivity listed above, giving the sensitivity of an objective function to local residual source terms.

3.5.2 Instructive Results

Sensitivity information can provide insight into the flow behavior, pointing to maximum leverage points within the flowfield. In addition, sensitivity information can provide estimates for modeling errors. Results of the sensitivity study are presented for the same cases shown in Figures 3-3 and 3-4. The global sensitivity of inner recirculation zone volume to changes in mixing and heat release is given for the cold and hot flow cases in Table 3.1. This is the first of the sensitivities outlined at the beginning of this section. The recirculation zone volume is normalized by the volume of the duct. The mixing coefficient is normalized by its value for a planar shear layer, and the heat release is normalized by the peak heat release at stoichiometric conditions.

Comparing the values in Table 3.1, we see that for hot flow, the sensitivity of recirculation zone volume to mixing is half that for the cold flow case. This result is expected due to the reduction in mixing rate with heat release shown for planar shear layers[30, 34]. This reduction is caused by a volumetric expansion of the hot gases in the shear layer, reducing the overall volume of fluid entrained into the mixing region. For both the reacting and non-reacting cases, the recirculation zone volume is less sensitive to changes in heat release than to changes in mixing. Therefore, the effect of modeling errors in mixing are greater than the effect of errors in heat release modeling.

As noted in Section 2.3, the centerline axial velocity can be linked to recirculation zone formation on the centerline (*i.e.*, if the axial velocity decreases, recirculation is more likely). Away from the recirculation zone, heat release dominates mixing as the influence coefficient for the effect of heat addition on axial velocity dominates the coefficient for the effect of mixing on axial velocity. This occurs due to low radial gradients of axial velocity away from the recirculation zone. However, on the downstream side of the recirculation zone boundary, shear stresses are large due to large axial velocity gradients in the radial direction. Hence, the local velocity ratio is large, and the influence coefficient for the effect of mixing on centerline axial velocity dominates that for heat release.

The sensitivity of recirculation zone volume to changes in the radial momentum residual is shown in Figure 3-5 for the reacting case of Figure 3-4. There are two visible regions where recirculation

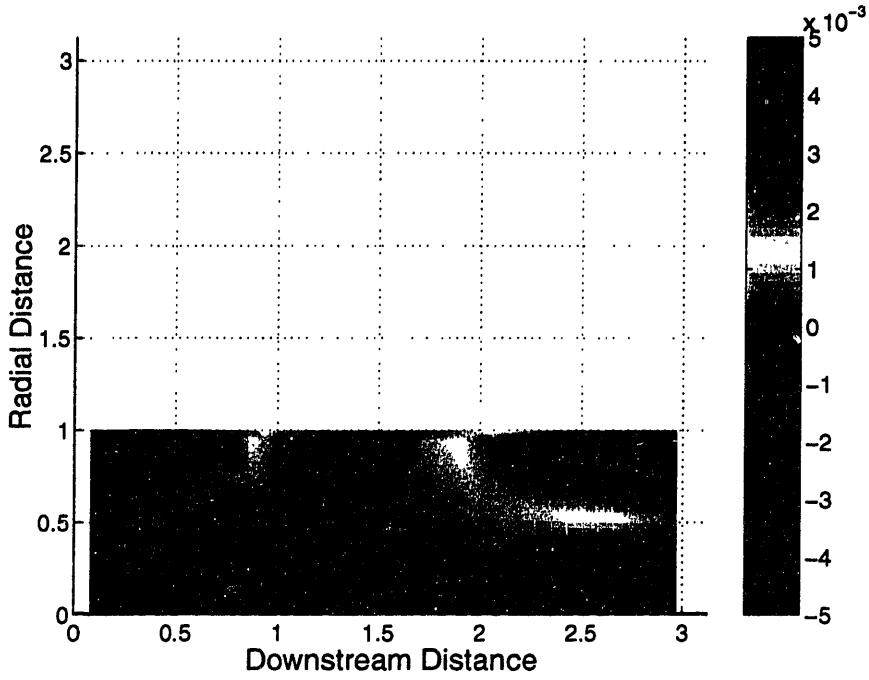

Figure 3-5: Sensitivity of recirculation zone volume to changes in the radial momentum residual ($\partial f/\partial R$) for a lean-premixed combustor with high swirl ($\Omega = 1.0$) and typical lean heat release ($\phi = 0.55$).

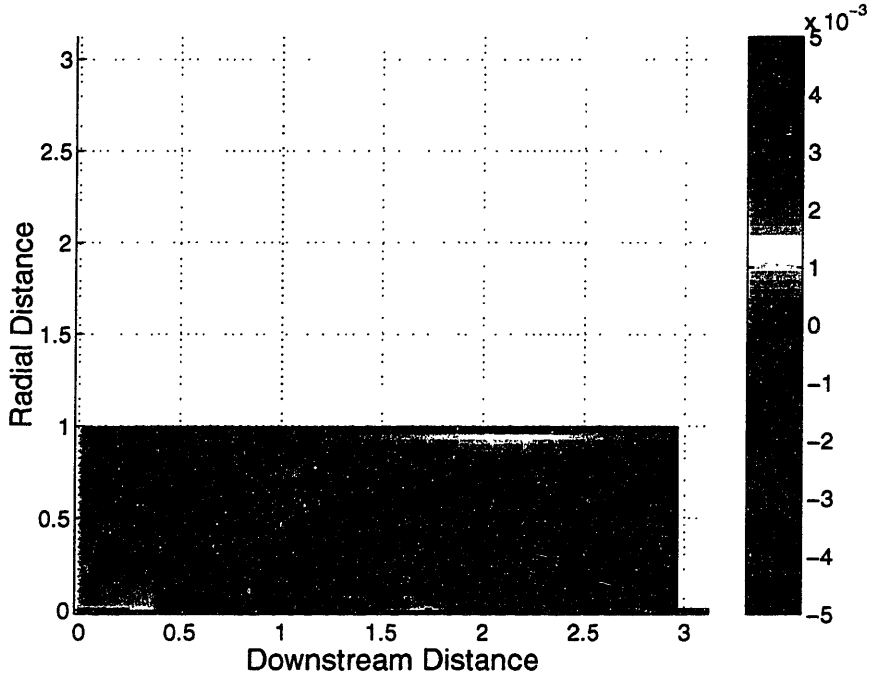

Figure 3-6: Sensitivity of static pressure to changes in heat release ($\partial U/\partial \alpha$) for a lean-premixed combustor with high swirl ($\Omega = 1.0$) and typical lean heat release ($\phi = 0.55$).

zone volume is either not affected or strongly affected by a change in radial momentum. For example, if a wall dilution jet were placed at 2.5 duct radii downstream, the negative radial momentum would have a large negative impact on the recirculation zone size. Therefore, Figure 3-5 yields the location of the maximum leverage points for dilution jet placement. The information is arrived at with almost no extra computational expense.

The sensitivity of static pressure to heat release is shown in Figure 3-6 for the reacting case of Figure 3-4. Two regions can be seen where a local increase in heat release could have either a strong positive impact or a strong negative impact. The area of strong positive impact occurs inside the inner recirculation zone near the upstream boundary. Therefore, an increase in heat addition inside the upstream region of the recirculation zone will cause an increase in the static pressure at the centerline of the duct. This corresponds to a lowering of the axial velocity on the centerline, and therefore, a trend toward a stronger recirculation zone. Inside the recirculation zone near the downstream boundary, and also in the region outside the recirculation zone, a strong negative impact on static pressure is suggested, indicating an acceleration of the fluid with heat addition, and therefore, a trend toward a weaker recirculation zone. Due to the greater extent of this region, the overall effect of adding heat to the flow should be to reduce the recirculation zone volume as shown by Figures 3-3 and 3-4 and Table 3.1.

3.6 Extension to Dilution Jet Mixing

CFLOW has been extended to handle dilution jet injection at the outer wall. The code accounts for the additional radial momentum, and possibly axial momentum, injected as well as enthalpy changes due to injection of colder fluid. The results will be compared to the sensitivity analysis of Figure 3-5 in order to validate the maximum leverage point for radial momentum injection.

3.6.1 Governing Equations

The implementation scheme for dilution jet injection is shown in Figure 3-7. Jet injection was simulated by adding an outer stream of fluid (represented by control volume j) with inlet conditions typical of a dilution jet. The stream flows axially outside the duct wall with no mixing until the injection point. The stream is then turned radially inward over a small axial distance and allowed to mix with the fluid in the $j-1$ control volume. In conjunction with this, the outer boundary of the jet control volume is turned inward to match the wall geometry downstream of the injection point.

If the $j-1$ control volume is being used to model a wall recirculation zone, as is the case in Figure 3-5, then the jet is added to the next radially inward control volume (*i.e.*, the $j-2$ control volume). Jet injection in gas turbine combustors is normally performed near the downstream edge of the recirculation zone. At the downstream plane of the recirculation zone in a CFLOW solution,

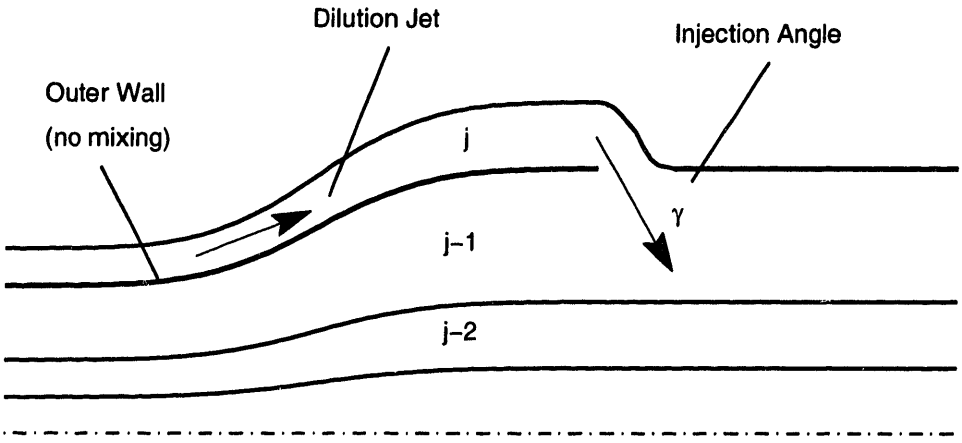

Figure 3-7: Schematic of dilution jet injection in CFLOW.

the mass transport has been decreased to zero and the Reynolds stresses increased, thus tying the $j-1$ and $j-2$ control volumes together. As these two control volumes are effectively acting as one control volume, the injected mass can be added to either.

The conservation equations for the $j-1$ control volume are modified with an additional source term. The jet state is specified at the inlet. The only additional parameter is the injection angle. This can be varied from 0 degrees (axial injection) to 90 degrees (radial injection). The magnitudes of the axial and radial momentum source terms are calculated consistent with the injection angle as

$$\tilde{M}_j = \rho_j {u_j}^2 A_j \cos\gamma, \tag{3.55}$$

$$\tilde{R}_j = \rho_j {u_j}^2 A_j \sin\gamma. \tag{3.56}$$

Continuity for cell $(i, j-1)$ in the $j-1$ control volume becomes

$$\rho_{2o} u_{2o} A_{2o} - \rho_{1o} u_{1o} A_{1o} = \tilde{m}_o - \tilde{m}_p - \tilde{m}_j, \tag{3.57}$$

where the mass source term is defined as

$$\tilde{m}_j = \rho_j u_j A_j, \tag{3.58}$$

and where the values for ρ_j, u_j, and A_j are specified at the inflow plane and do not varying between

the inflow plane and the injection point.

The axial momentum equation for cell $(i, j-1)$ in the $j-1$ control volume becomes

$$(\rho_{2o}{u_{2o}}^2 + p_{2o})A_{2o} - (\rho_{1o}{u_{1o}}^2 + p_{1o})A_{1o} - p_{p2}\Delta A_p + p_{o2}\Delta A_o = M_{xo} - M_{xp} + \tilde{M}_o - \tilde{M}_p - \tilde{M}_j. \quad (3.59)$$

The radial momentum equation for cell $(i, j-1)$ in the $j-1$ control volume becomes

$$\rho_{2o}u_{2o}A_{2o}v_{2o} - \rho_{1o}u_{1o}A_{1o}v_{1o} + p_{p2}A_p - p_{o2}A_o - \frac{1}{2}\left(\rho_{2o}{w_{2o}}^2 + \rho_{1o}{w_{1o}}^2\right)\Delta A = -\tilde{R}_j. \quad (3.60)$$

The energy equation equation for cell $(i, j-1)$ in the $j-1$ control volume becomes

$$\left(C_{p_{2o}}T_{2o} + \frac{1}{2}{u_{2o}}^2 + \frac{1}{2}{v_{2o}}^2 + \frac{1}{2}{w_{2o}}^2 - h_{pr_{2o}}\right)\rho_{2o}u_{2o}A_{2o}$$

$$-\left(C_{p_{1o}}T_{1o} + \frac{1}{2}{u_{1o}}^2 + \frac{1}{2}{v_{1o}}^2 + \frac{1}{2}{w_{1o}}^2 - h_{pr_{1o}}\right)\rho_{1o}u_{1o}A_{1o}, \quad (3.61)$$

$$= H_{to} - H_{tp} + H_{xo} - H_{xp} + H_{ro} - H_{rp} + \tilde{H}_o - \tilde{H}_p - \tilde{H}_j$$

where the energy source term is defined as

$$\tilde{H}_j = \left(C_{p_j}T_j + \frac{1}{2}{u_j}^2\right)\rho_j u_j A_j, \quad (3.62)$$

and where the values for C_{p_j} and T_j are specified at the inflow plane and do not vary between the inflow plane and the injection point. The tangential momentum and state equations are left unchanged by the jet injection.

3.6.2 CFLOW Dilution Jet Injection Results

Two cases were run for the same conditions as those in Figures 3-4 and 3-5 with the jet injection turned on. The jet was injected at 90 degrees (purely radial) with mass flows of 1% and 25% of the inlet mass flow. The case with 1% mass flow injection was chosen to evaluate the sensitivity results within a linear regime. Injection of 1% of the combustor inlet mass flow is typical of dilution jets downstream of the primary zone[35]. The case with 25% mass flow injection was chosen to represent

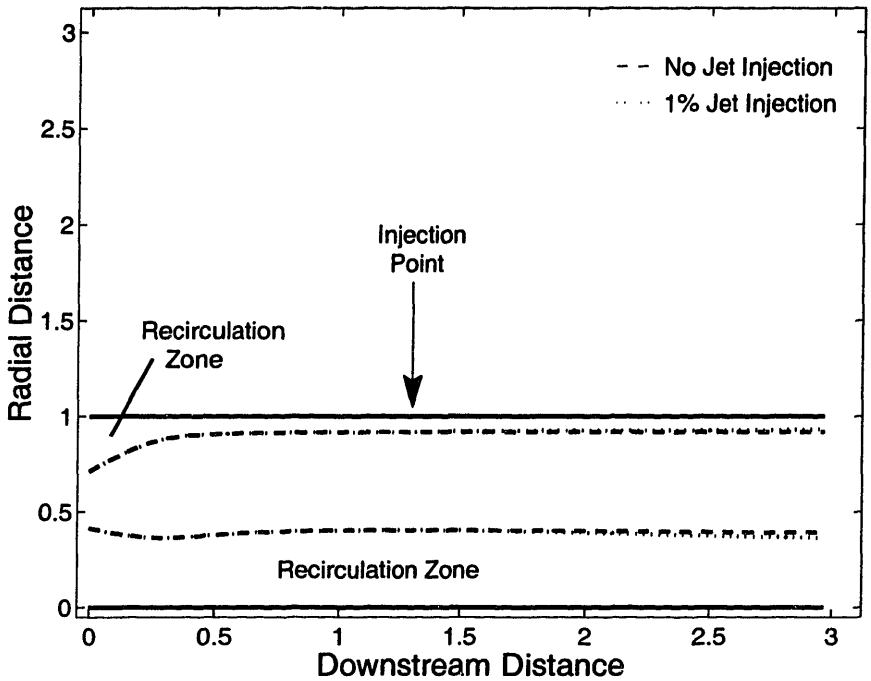

Figure 3-8: Recirculation zone boundaries computed by CFLOW for radial jet injection of 1% inlet mass flow at $z/R_0 = 1.3$ with high swirl ($\Omega = 1.0$) and typical heat release ($\phi = 0.55$).

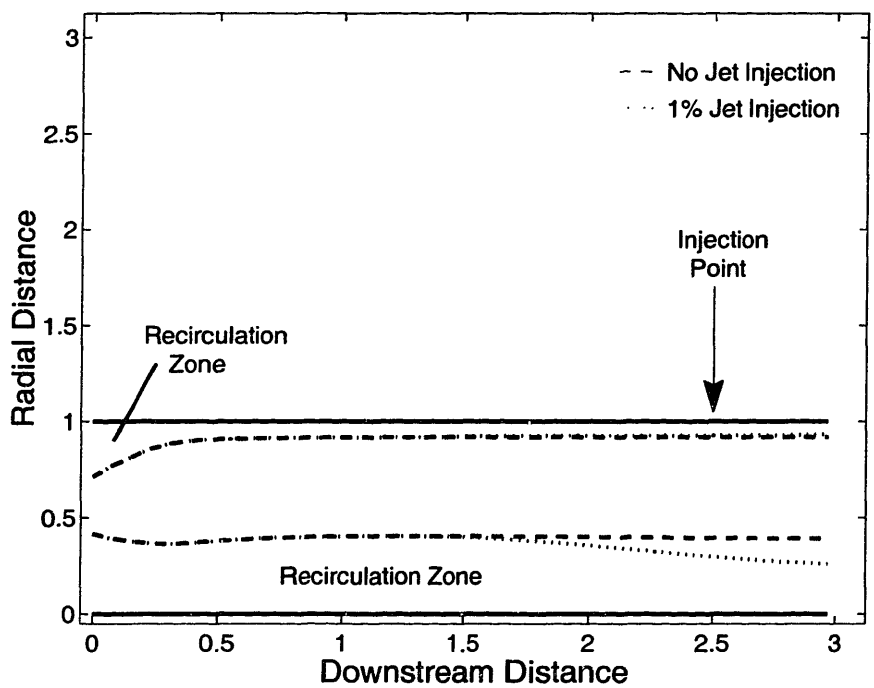

Figure 3-9: Recirculation zone boundaries computed by CFLOW for radial jet injection of 1% inlet mass flow at $z/R_0 = 2.5$ with high swirl ($\Omega = 1.0$) and typical heat release ($\phi = 0.55$).

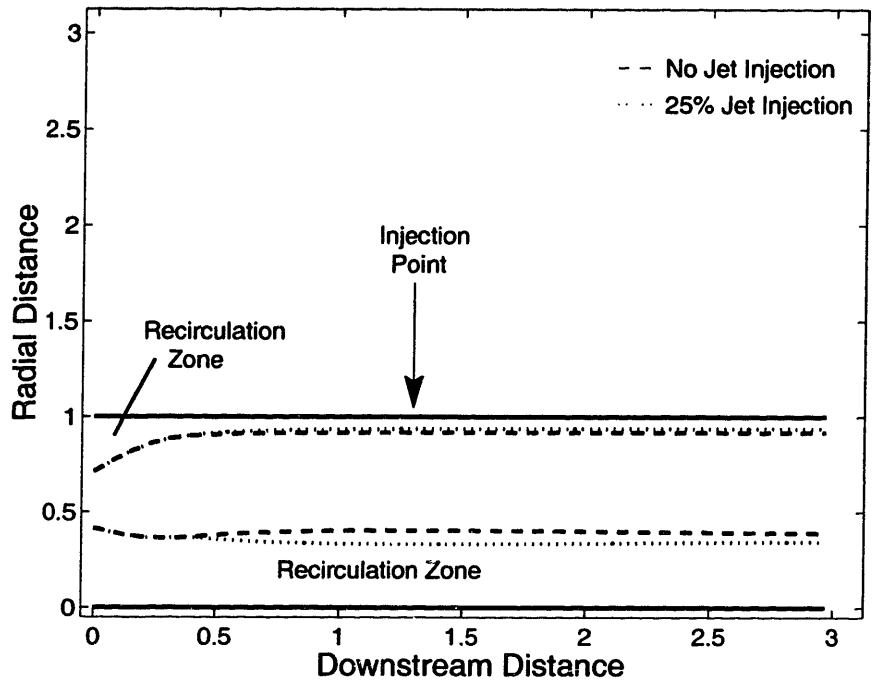

Figure 3-10: Recirculation zone boundaries computed by CFLOW for radial jet injection of 25% inlet mass flow at $z/R_0 = 1.3$ with high swirl ($\Omega = 1.0$) and typical heat release ($\phi = 0.55$).

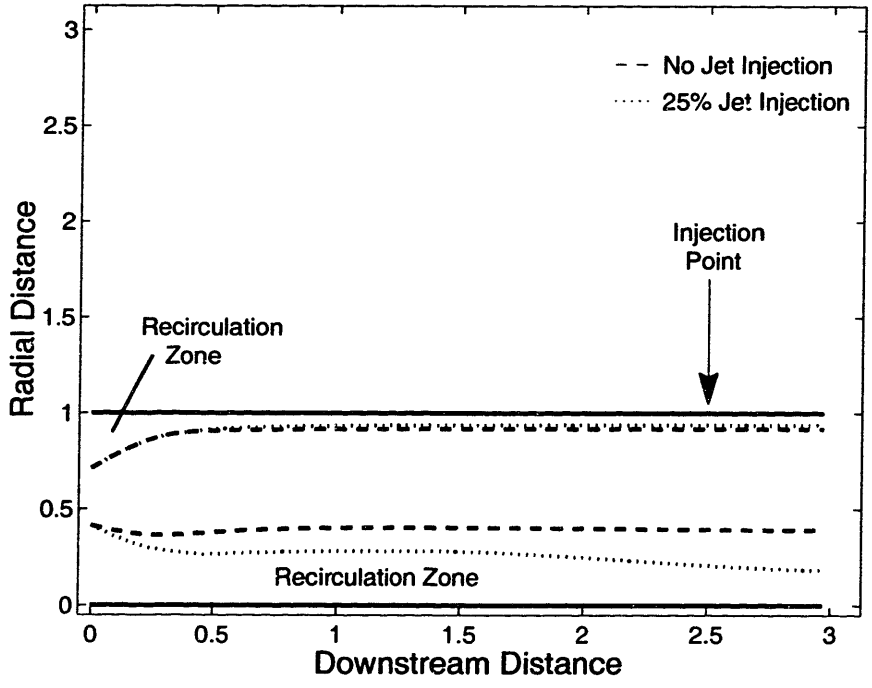

Figure 3-11: Recirculation zone boundaries computed by CFLOW for radial jet injection of 25% inlet mass flow at $z/R_0 = 2.5$ with high swirl ($\Omega = 1.0$) and typical heat release ($\phi = 0.55$).

the conditions for primary jet injection used to aid in primary zone closure[36]. It was not possible to run these cases for the axisymmetric or 3-D Navier-Stokes codes, as they do not allow for inflow through the walls.

Figures 3-8 and 3-9 show the recirculation zone boundary for a case with 1% mass flow injection at 1.3 and 2.5 duct heights downstream, respectively. The inner recirculation zone volume does not change for injection at $z/R_0 = 1.3$, as suggested by the sensitivity field plotted in Figure 3-5. However, for radial jet injection at $z/R_0 = 2.5$, the inner recirculation zone volume decreases by 13%. The magnitude of the decrease suggested by the sensitivity analysis is 11%. Therefore, the effect of jet injection on the inner recirculation zone volume given by the sensitivity analysis compares well with the computed values for small injection mass flows.

Figures 3-10 and 3-11 show the recirculation zone boundary for a case with 25% mass flow injection at 1.3 and 2.5 duct heights downstream. The inner recirculation zone volume decreases by 8% for injection at $z/R_0 = 1.3$. This disagrees with the sensitivity analysis which suggests no change. However, the sensitivity analysis is a linearized computation and strictly speaking, is only valid for small changes. For radial jet injection at $z/R_0 = 2.5$, the inner recirculation zone volume decreases by 56% (compared to the 271% decrease suggested by the sensitivity analysis). The discrepancy is a result of applying a linearized model to a non-linear regime. However, the trend given by the sensitivity analysis is correct.

Comparisons of CFLOW, quasi 1-D, and UTNS in Chapter 5 will show that the strength and location of a recirculation zone depends on the behavior of the low total pressure stream tube at the centerline of the duct. Jet injection should thus have the greatest impact on the recirculation zone at the point in the flowfield where a pressure rise due to mass injection and mixing has the greatest impact on the centerline axial velocity. This point occurs at the trailing edge of the recirculation zone, due to the large axial pressure gradients present. This agrees with the results of the jet injection study presented here.

3.7 Limitations

While CFLOW will be shown to perform very well against Navier-Stokes solutions in Chapter 5, it also has limitations. First, it should not be run for fewer than two streams due to the format of the Newton matrix setup routines. Also, as the number of streams decreases, resolution of the the radial swirl profile decreases. This effect is evaluated at the end of Section 5.3.

Accuracy of recirculation zone boundary computation decreases rapidly for swirl ratios above 2.0. Above swirl ratios of 2.0, the tangential momentum begins to dominate the axial momentum. This causes the differences in swirl velocity to drive the mixing instead of differences in axial velocity. However, recirculation zone closure requires large axial velocity gradients to drive the mixing.

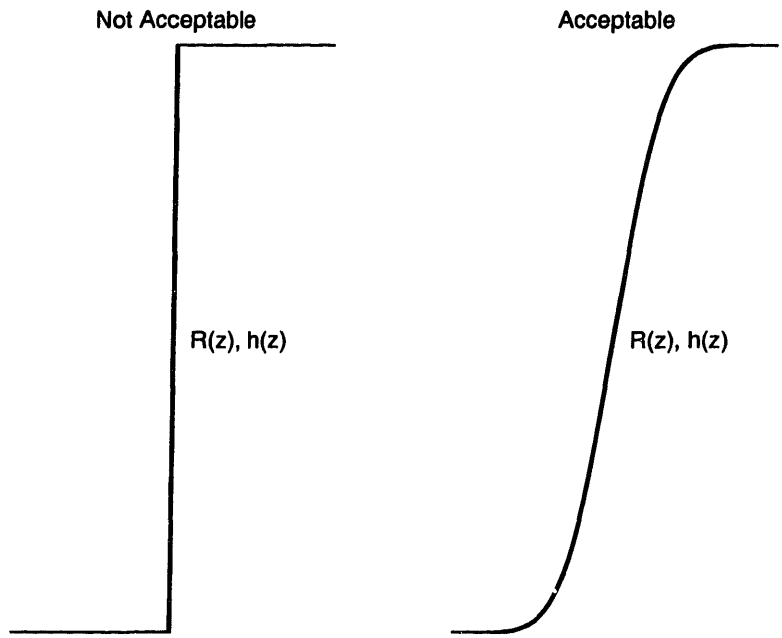

Figure 3-12: Acceptable and nonacceptable duct and heat addition profiles.

Therefore, cases with swirl ratios of 2.0 or greater will not be able to model recirculation zone closure properly.

Heat releases above that for a stoichiometric flame should not be specified as this could cause unrealistic temperature rises. Mixing rates down to zero may be specified without harm. However, mixing coefficients above roughly 10 times that of a planar shear layer are unrealistic and may result in the damping of mass transfer. This occurs due to Reynolds stresses being high enough to immediately mix out any velocity differences, thus eliminating the driver for mass transport out of the recirculation zone. This will cause the recirculation zone to not close properly.

The simplified mixing and heat release models used have limitations caused by the need to specify empirically-based parameters prior to calculation of the flowfield. This limitation is typical for most CFD codes as well due to the use of simplified turbulence and heat transfer models. The sensitivity of recirculation zone volume to mixing and heat release is addressed in Chapters 5 and 6. These results showed that increasing or decreasing the level of mixing by a factor of two caused a change in recirculation zone volume of between 10% and 30% depending on the flow conditions and geometry. In addition, increasing or decreasing the slope of the heat release profile by a factor of two caused a change in recirculation zone volume of between 5% and 15%.

Sharp area changes downstream of the inlet should be smoothed. At present CFLOW will not handle a rearward facing step whose face occurs downstream of the inlet. Also sharp increases that approach step functions in heat release will cause the Newton solver to decrease the iteration step size significantly, greatly increasing computational times. For example, across a single axial grid

cell, heat addition source terms equal in magnitude to the stream enthalpy will cause CFLOW to decrease the maximum change in temperature per Newton iteration by an order of magnitude. In turn, this will increase computational times by at least an order of magnitude. A smooth, high-gradient region is recommended instead. This is likely to be more realistic as well. Figure 3-12 gives examples of acceptable and nonacceptable duct and heat addition profiles.

Chapter 4

Axisymmetric Navier-Stokes Code (UTNS)

The Navier-Stokes code UTNS (Upwinding-based, Time-dependent Navier-Stokes) was used for comparison to the reduced order models described in Chapters 2 and 3. The code was originally developed for turbine blade heat transfer prediction, and it has been extended for use in more general applications[37].

UTNS solves the axisymmetric compressible Reynolds-averaged Navier-Stokes equations with a two-equation (k-ϵ) turbulence model. Combustion and flame tracking is handled with a flame sheet model. A flame sheet model orients the flame such that the normal velocity is equal to the flame speed. Flame speeds are specified consistent with those for premixed methane-air combustion. As a consequence of the flame sheet approximation, specification of a no-slip wall boundary causes the flame front to propagate upstream to the inlet in the wall boundary layer, and a slip velocity at the wall is thus allowed.

The Navier-Stokes equations are discretized onto multi-block structured grids. The numerical scheme is a cell-based finite volume technique and uses upwind-biased differencing. An Euler implicit time-dependent scheme is used to reach steady-state solutions. For unsteady problems, a Newton method is used with sub-iterations based on a dual-time stepping. The accuracy of convection terms varies from first to ninth order. The various orders of accuracy are achieved by interpolation of the characteristic variables to the cell faces.

At the upstream boundary, the total pressure, total temperature, and flow angle distributions are specified. The exit boundary condition consists of a specified static pressure at the centerline and a radial pressure distribution based on the assumption of radial equilibrium. Other quantities are extrapolated from the interior of the domain. The state variables include axial, radial, and tangential velocities, temperature, density, static pressure, and a reaction progress variable following the mass

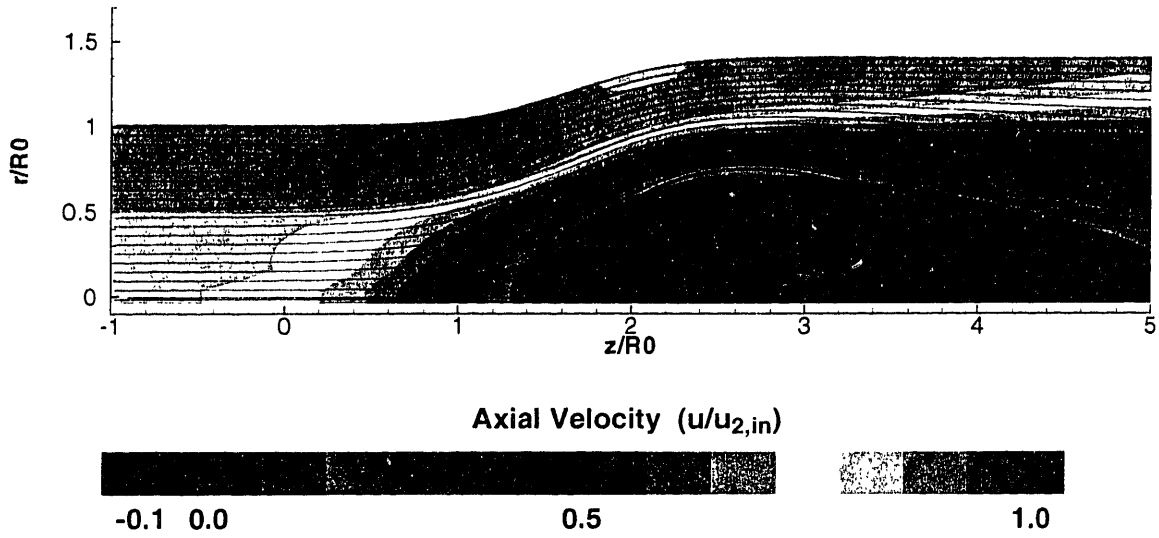

Figure 4-1: Axial velocity contours and streamlines from UTNS for a high swirl ($\Omega = 0.8$), high heat release ($\phi = 0.8$) case.

fraction of fuel.

Figure 4-1 shows an example of the output from UTNS. Shown are axial velocity contours as well as streamlines highlighting the recirculation zone. The case shown had high swirl ($\Omega = 0.8$) and high heat release ($\phi = 0.8$). The axial velocity ratio was 0.8. The density and temperature ratios at the inlet were 1.0.

Solutions such as the case in Figure 4-1 are obtained by first solving the non-reacting case to provide an initial converged solution for the reacting case at low heat release. Heat release is then increased by changing the inlet fuel-air distribution. Without the aid of a pre-converged restart file, a solution of this type requires computational times on the order of one day. To obtain a solution for the reacting case, an additional day of computational time is required.

Chapter 5

Comparison of Models

To assess the relative merits of the models developed, a four-tiered comparison has been adopted. This includes a quantitative comparison of the models for swirling non-recirculating flows, a quantitative comparison of recirculation onset boundary, and both qualitative and quantitative comparisons for recirculating flows. The models to be compared will be the quasi 1-D model described in Chapter 2, the quasi 1-D model with recirculation (CFLOW) described in Chapter 3, and the axisymmetric Navier-Stokes code (UTNS) described in Chapter 4. Because the quasi 1-D model does not compute recirculating flows, only qualitative comparison to higher-fidelity models is possible. The results from these comparisons will be summarized briefly before describing each comparison in detail.

Quantitative comparison for the non-recirculating case involves comparison of flow regime maps similar to those presented for the quasi 1-D model in Figures 2-4 through 2-8. The figure of merit is the difference in the local swirl ratio and its relation to the various flow regimes. The flow regime map for the Navier-Stokes solution was constructed by determining the influence coefficients numerically. This was accomplished by defining an effective core interface based on the radial location of the maximum in swirl velocity and then mass-averaging the flow quantities and their ratios for use in computing values for the influence coefficients. It will be shown that the flow regime maps for all three models agree to within 10% of the local swirl ratio and the swirl ratios defining the flow regime boundaries.

Quantitative comparison of the recirculation onset boundary involves comparison of the axial location of the recirculation zone leading edge computed by each model. The leading edge is defined as the axial station where the centerline axial velocity first reaches zero. The figure of merit is the difference in the axial location of the recirculation zone leading edge. It will be shown that the axial location of the onset boundary for CFLOW and UTNS agrees to within 10% for the cold and hot flow cases. The quasi 1-D model can be tuned to agree with the UTNS solution to within 5% for

cold flow, but computes no recirculation for hot flow.

Qualitative comparison for a recirculating flow involves comparison of the trends suggested by quasi 1-D and the influence coefficients concerning the size and location of a recirculation zone computed by CFLOW and UTNS for varying heat release and inlet swirl. The figure of merit is the agreement of the trends. It will be shown that the trends given by the influence coefficients are borne out in both UTNS and CFLOW.

Quantitative comparison for a recirculating flow involves comparison of the size and location of a recirculation zone. There are several ways of defining the recirculation zone boundary, including the bounding streamline, the line of maximum shear stress, and the line of zero axial velocity. The last definition is most often used in experimental studies and yields the smallest recirculation zone. The first is most often used in CFD and yields the largest recirculation zone. The second definition was used in this comparison and yields a recirculation zone size somewhere in between the other two. This definition was chosen based on the formulation of CFLOW where a control volume interface is defined by the maxima in shear stress between two co-flowing streams. The figure of merit is the difference between the recirculation zone volume computed by CFLOW and UTNS. It will be shown that the recirculation zone volume computed by CFLOW agrees to within 25% of that given by UTNS for all cases run.

The remainder of the chapter is broken into four sections. In Section 5.1, the quasi 1-D model is compared with the Navier-Stokes code (UTNS). Only the first three comparisons are presented since the quasi 1-D model cannot give quantitative information about a recirculating flowfield. Section 5.2 presents the comparison of CFLOW to UTNS and quasi 1-D. A comparison of UTNS to experimental data is given in Section 5.3, while Section 5.4 presents a summary of the model comparisons.

5.1 Quasi 1-D Analysis vs. UTNS

Discussion of the quasi 1-D model and influence coefficient analysis in Chapter 2 showed that these tools may provide insight into the physical processes present in swirling flows with combustion. However, it remains to be shown that these tools can reproduce the results of higher-fidelity models. Therefore, a comparison of the quasi 1-D model and resulting influence coefficients with the results of the axisymmetric Navier-Stokes code (UTNS) is thus performed to demonstrate the utility of a quasi 1-D analysis.

A quantitative comparison of flow regime maps was performed for a non-recirculating case and is shown in Figure 5-1. For this flow regime map, as well as the one presented in Figure 5-5, the boundaries are represented by colors. The yellow represents the local values of Ω_1, while red represents Ω_2. The value of Ω_3 is represented by blue, and the critical swirl ratio (Ω_{crit}) is denoted by green. The local swirl ratio (Ω) is in black. The flow regime map for the UTNS solution was

Table 5.1: Conditions for the non-recirculating case of Figure 5-1.

Inlet Parameter	Value
Swirl Ratio, Ω_0	0.3
Velocity Ratio, r_0	0.8
Density Ratio, s_0	1
Area Ratio, α_0	4
Equivalence Ratio, ϕ_1, ϕ_2	0.8
Mixing Coefficient, Ξ	2.3 ν_t

constructed by determining the influence coefficients numerically. An effective core interface was defined based on the radial location of the maximum in swirl velocity. The flow quantities and their ratios were mass-averaged for use in computing values for the influence coefficients. The circles represent the mass-averaged solution and trend boundaries as described in Chapter 2. Table 5.1 gives the inlet conditions for this case.

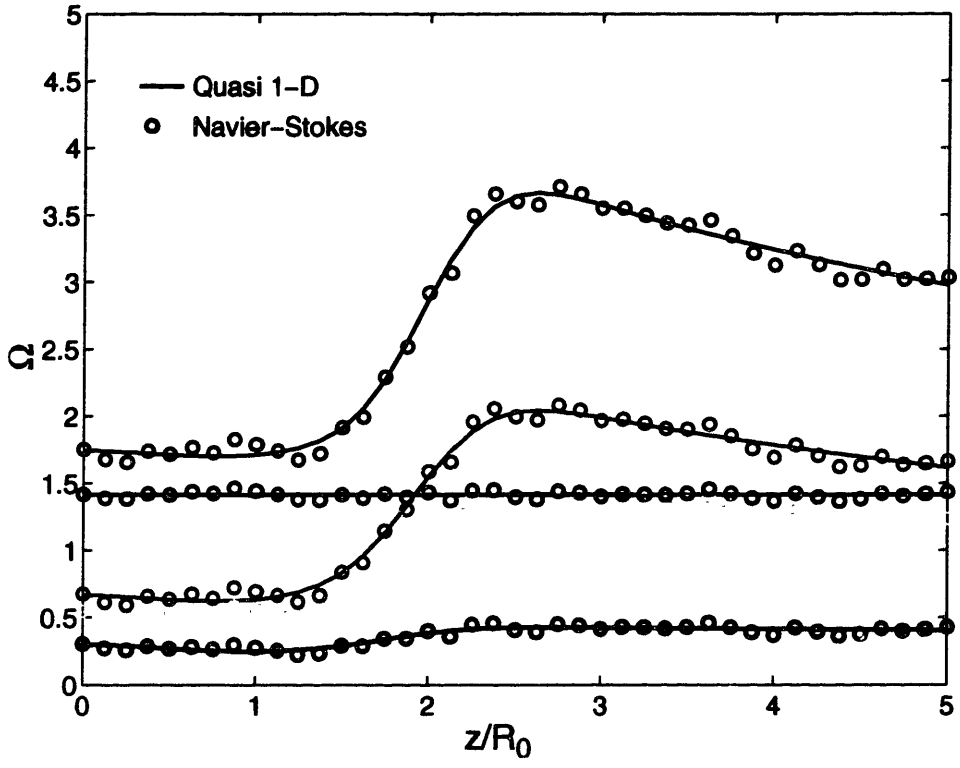

Figure 5-1: Comparison of quasi 1-D (–) and mass-averaged UTNS (o) flow regime maps. Swirl ratios include Ω_1 (yellow), Ω_2 (red), Ω_3 (blue), Ω_{crit} (green), Ω (black).

The local swirl ratio for the quasi 1-D and mass-averaged UTNS solutions agrees to within 5%. The swirl ratios defining the boundaries of the flow regimes agree to within 10%. Since the solution remains in region 1 for the entire flowfield, it can be concluded that the quasi 1-D model

Table 5.2: Conditions for the weakly recirculating cases of Figure 5-2.

	Zero Heat Release, $\phi_1 = \phi_2 = 0.0$	High Heat Release, $\phi_1 = \phi_2 = 0.8$
Swirl Ratio, Ω_0	0.47	0.61
Velocity Ratio, r_0	0.8	0.8
Density Ratio, s_0	1	1
Area Ratio, α_0	676	676
Mixing Coefficient, Ξ	2.3 ν_t	2.3 ν_t

compares well with mass-averaged UTNS. This result is expected since a weakly swirling flow with no recirculating flow is not a severe test of the model's performance.

The second comparison between quasi 1-D and UTNS is a quantitative comparison of the recirculation onset boundary (*i.e.*, the axial location of the recirculation zone leading edge computed by each model). The leading edge is defined as the axial station where the centerline axial velocity first reaches zero. The initial vortex core area and the mixing coefficient were varied to yield the best match in recirculation onset point for the quasi 1-D model and UTNS. Once these values were set, heat was added to the quasi 1-D model. Good performance of the model would be defined as its ability to compute the hot flow onset point using the cold flow values for core area and mixing.

The results of this comparison are shown in Figure 5-2 for swirling flow with a weak recirculation at zero and high heat release. The inlet values used for the quasi 1-D model are given in Table 5.2 for both the cold and hot flow cases. Note that the inlet swirl ratio was higher for the high heat release case than for the cold flow. This was necessary due to the impact of heat addition on recirculation zone formation in the UTNS solutions. Simply put, the addition of heat resulted in no recirculation zone being formed at the cold flow swirl ratio. Therefore, in order to obtain a weakly recirculating flow, the inlet swirl had to be raised for the high heat release case.

The quasi 1-D model can be tuned to agree with the UTNS solution to within 5% for zero heat release. However, when heat is added, the quasi 1-D model computes that no recirculation zone is formed using the cold flow values for core area and mixing. Physically, the heat addition causes acceleration in the outer flow as suggested by the influence coefficients for all swirls. Due to the small area of the vortex core, the influence coefficients suggest that the behavior of the outer flow will determine the behavior of the vortex core. Essentially, heat addition in the outer flow causes the outer flow to expand, squeezing the vortex core, and causing the vortex core to accelerate. This keeps the vortex core axial velocity from approaching zero and allowing a recirculation zone to form. Therefore, the quasi 1-D model is not a useful tool for quantitative computation of the recirculation zone onset point. Due to the presence of a recirculation zone, this comparison is a more severe test of the quasi 1-D model's ability. However, the recirculation zone was of limited extent and strength, making this a less severe case than the next comparison.

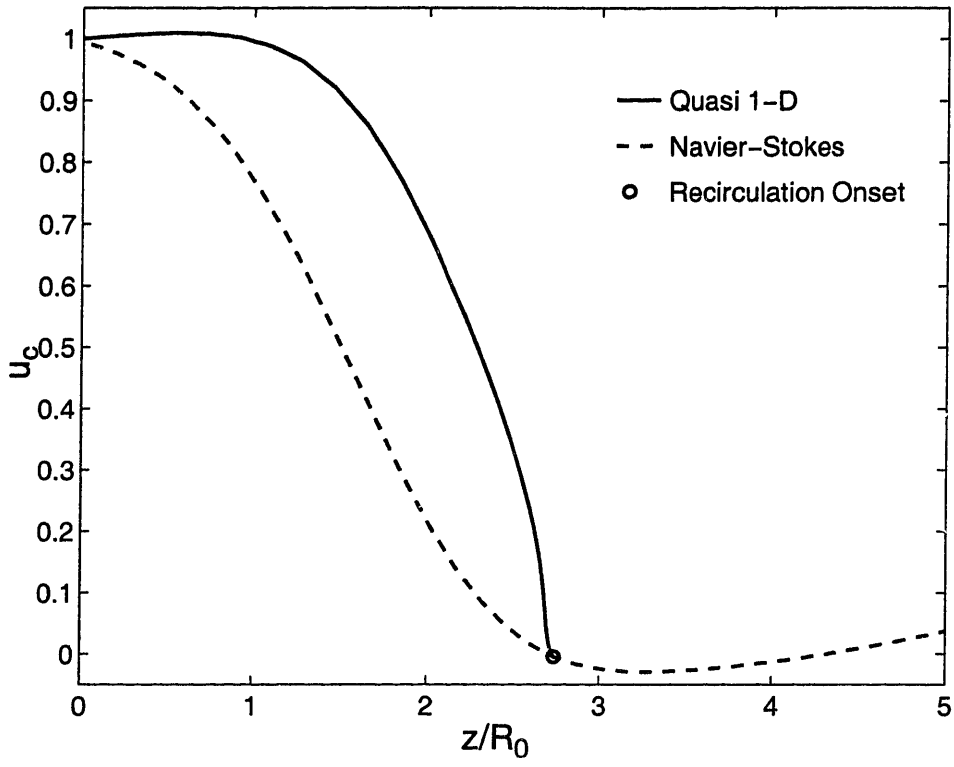

a) Zero Heat Release

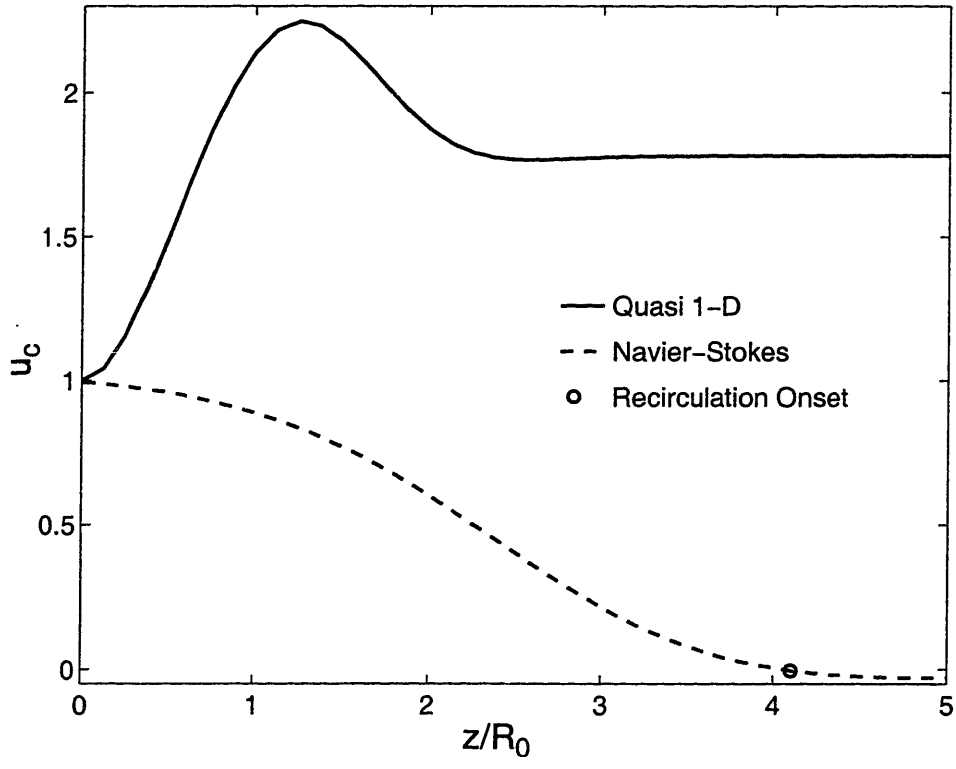

b) High Heat Release

Figure 5-2: Comparison of quasi 1-D (–) and UTNS (– –) centerline axial velocities for a) zero heat release ($\phi = 0.0$) and b) high heat release ($\phi = 0.8$). The recirculation onset point is marked (o).

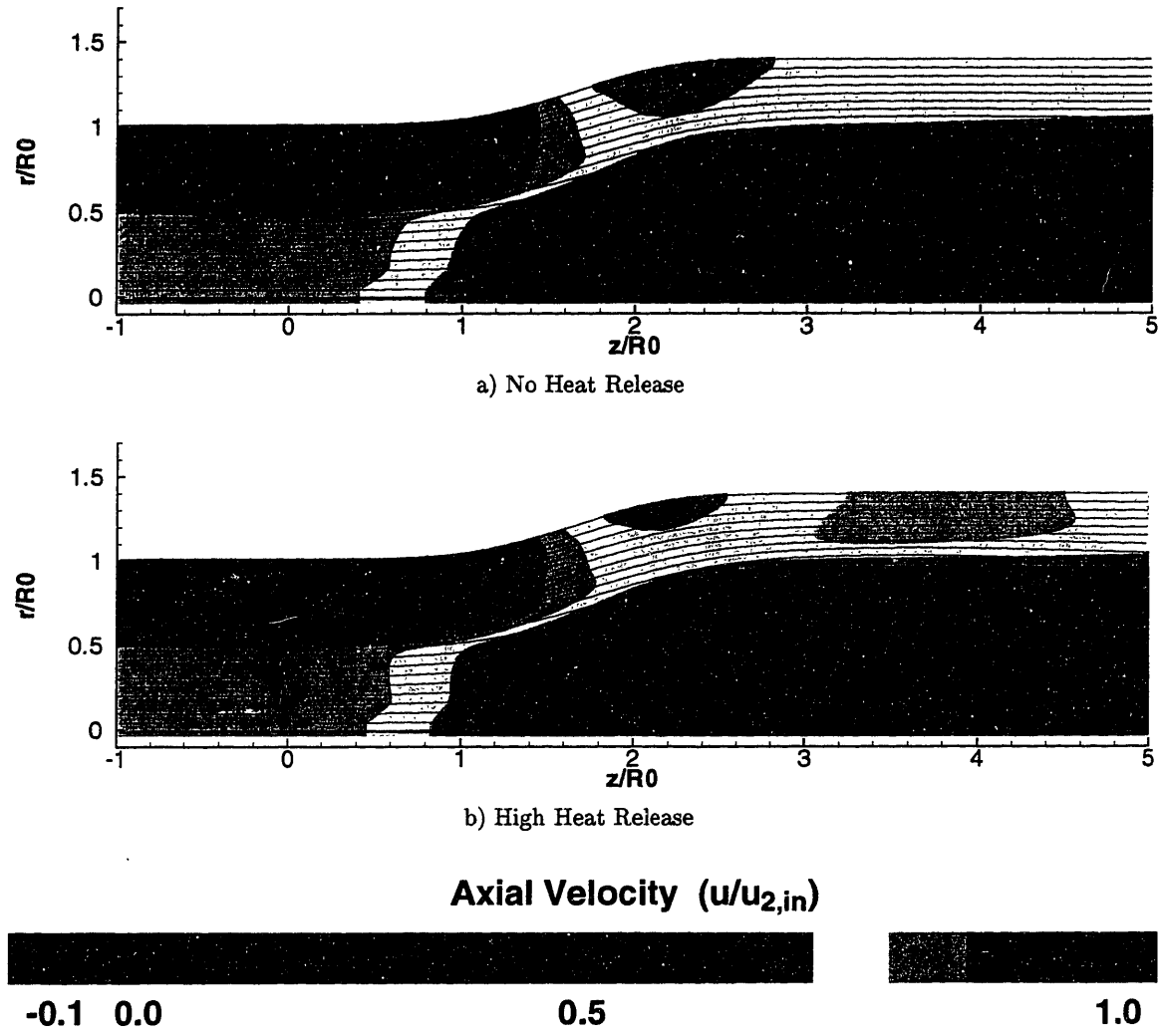

Figure 5-3: Axial velocity contours and streamlines for a UTNS solution with low swirl ($\Omega = 0.5$) at a) zero heat release ($\phi = 0.0$) and b) high heat release ($\phi = 0.8$).

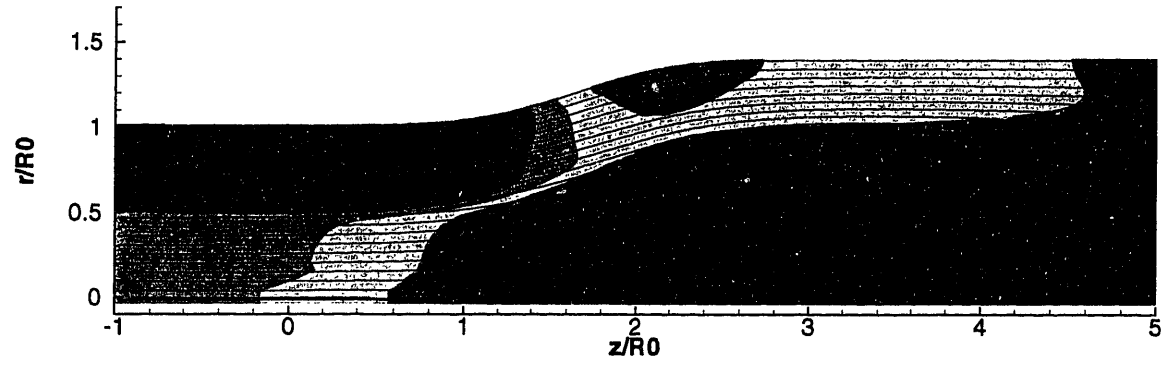

a) No Heat Release

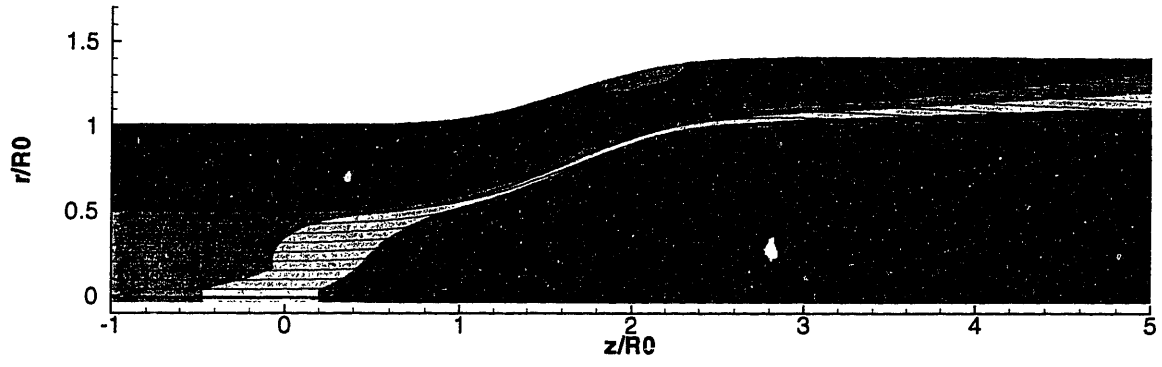

b) High Heat Release

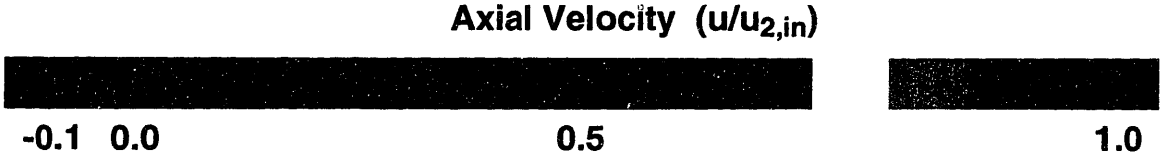

Figure 5-4: Axial velocity contours and streamlines for a UTNS solution with high swirl ($\Omega = 0.8$) at a) zero heat release ($\phi = 0.0$) and b) high heat release ($\phi = 0.8$).

The final comparison between quasi 1-D and UTNS is a qualitative comparison for recirculating flow. The trends suggested by the quasi 1-D model and the resulting influence coefficients are compared with the size and location of a recirculation zone given by UTNS for varying heat release and swirl ratio. Heat release was varied for the same inlet conditions to test the validity of the influence coefficients for suggesting trends in flow behavior. Specifically, the low/high swirl behavior with heat release in the core was examined by observing changes in size and location of the recirculation zone for varying heat release. The results are shown in Figures 5-3 and 5-4 for the low and high swirl behaviors, respectively.

A low swirl ($\Omega_0 = 0.5$) case with zero and high heat release ($\phi = 0, 0.8$) is shown in Figures 5-3a and b, respectively. Contours of axial velocity are plotted along with the streamlines. For low swirl, increasing heat release causes an acceleration of the streamtube on the centerline, resulting in a weaker recirculation zone located further downstream, as would be expected for the limiting case of zero swirl.

A high swirl ($\Omega_0 = 0.8$) case with zero and high heat release ($\phi = 0, 0.8$) is shown in Figures 5-4a and b, respectively. For high swirl, increasing heat release causes deceleration of the streamtube on the centerline, resulting in a stronger recirculation zone which is located further upstream, in accord with the trends from the influence coefficients. These results, coupled with the severity of these flow conditions, support the utility of the quasi 1-D model for providing insight into the parametric trends for swirling flows with combustion.

The comparisons show that the quasi 1-D model can compute the behavior of swirling flow without recirculation. Also, despite the quasi 1-D model's poor performance in computing the onset of recirculation zone formation, the trends given by the influence coefficient analysis are borne out in the solutions of the Navier-Stokes code, UTNS. The ability of the quasi 1-D model to provide design trends supports the utility of this model as a reduced-order analysis tool.

5.2 CFLOW vs. Quasi 1-D and UTNS

The quasi 1-D model lacks the ability to yield quantitative information about a recirculating flowfield. The model developed in order to address this deficiency was CFLOW, described in Chapter 3. The current section will describe a four-tiered comparison between CFLOW and the models discussed in Section 5.1, namely quasi 1-D and UTNS.

A quantitative comparison of flow regime maps was performed for a non-recirculating case. The inlet conditions for the flow regime map shown in Figure 5-5 were the same as those given in Table 5.1. As before, the flow regime map for the UTNS solution was constructed by determining the influence coefficients numerically through mass-averaging of the flow quantities and their ratios. The circles represent the mass-averaged solution and trend boundaries as described in Chapter 2.

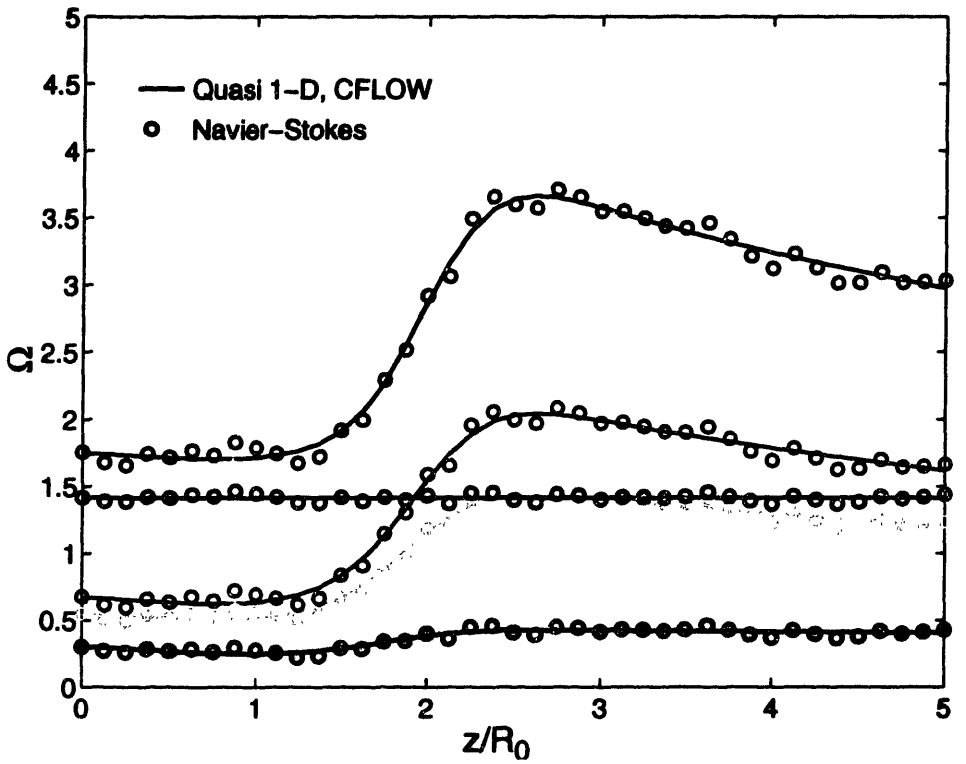

Figure 5-5: Comparison of CFLOW (–), quasi 1-D (–), and mass-averaged UTNS (o) flow regime maps. Swirl ratios include Ω_1 (yellow), Ω_2 (red), Ω_3 (blue), Ω_{crit} (green), Ω (black).

The solid line represents both the quasi 1-D and CFLOW solutions as the models become identical for the non-recirculating case. The boundaries are represented by the various colors as described in Section 5.1.

The local swirl ratio for CFLOW and quasi 1-D are identical and agree with the mass-averaged UTNS solution to within 5%. The swirl ratios defining the boundaries of the flow regimes agree to within 10%, and since the solution remains in region 1 for the entire flowfield, it can be concluded that CFLOW compares well with quasi 1-D and mass-averaged UTNS. This result is expected since a weakly swirling flow with no recirculating flow is not a severe test of the model's performance.

The second comparison between CFLOW, quasi 1-D, and UTNS was a quantitative comparison of the recirculation onset boundary. This involved comparison of the axial location of the recirculation zone leading edge computed by each model as described in Section 5.1. The recirculation onset point for CFLOW was computed by using a third inner control volume on the centerline of the duct to represent the low-total-pressure streamtube that will eventually determine when the recirculation zone forms. The initial area of this control volume was set based on the shear stress field given by the Navier-Stokes code. The remainder of the flowfield was represented by two larger control volumes, representing the remainder of the vortex core and the irrotational outer stream. The mixing coefficient was set to the empirically determined value of $\Xi = 4.0\nu_t$ based on the comparison

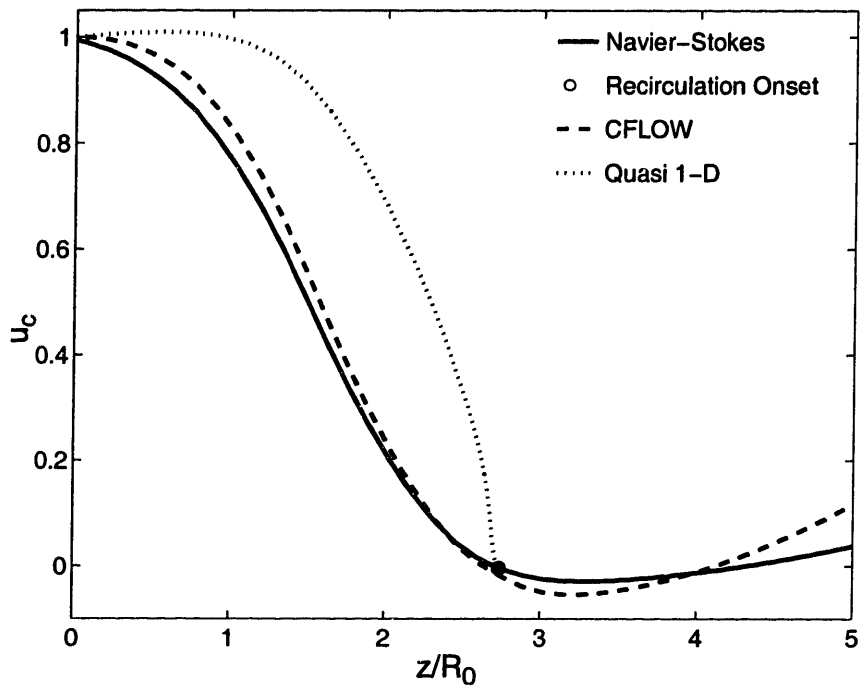

a) Zero Heat Release

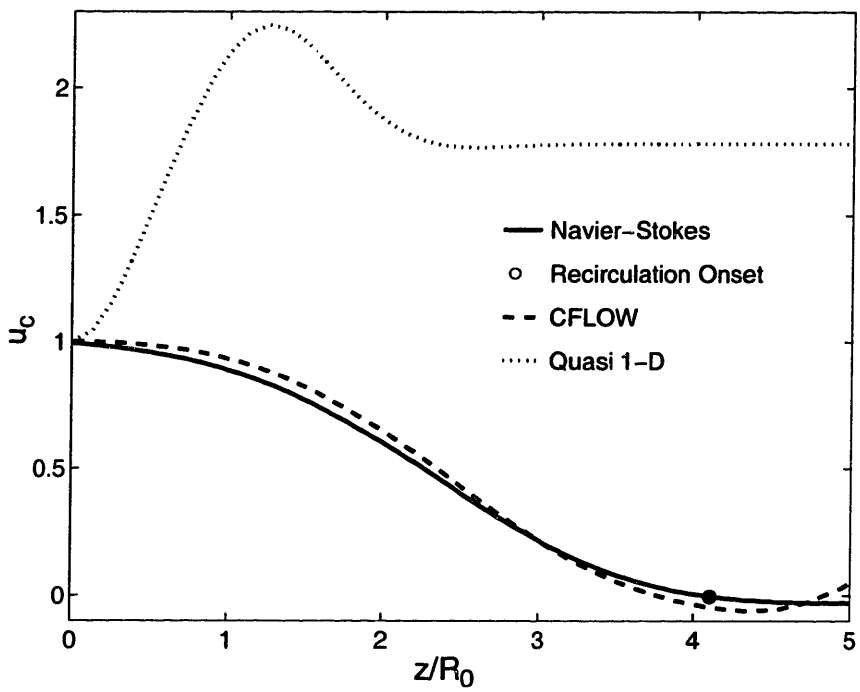

b) High Heat Release

Figure 5-6: Comparison of CFLOW (–), quasi 1-D (–), and UTNS (– –) centerline axial velocities for a) zero heat release ($\phi = 0.0$) and b) high heat release ($\phi = 0.8$). The recirculation onset point is marked (o).

of CFLOW to experimental data discussed in Section 5.3. This mixing coefficient differs from that used in the non-recirculating comparison discussed above due to the increased level of mixing present in a recirculating flow. Heat was added to CFLOW while keeping everything else constant. As before, good performance of the model would be defined by the ability to compute a hot flow onset point using the cold flow values for core area and mixing. The results of this comparison are shown in Figure 5-6 for swirling flow with a weak recirculation at zero and high heat release. The inlet values used for CFLOW are the same as those given in Table 5.2 for the quasi 1-D model with the exception of the mixing coefficient.

For CFLOW, agreement to within 5% can be achieved for zero heat release, with the onset point computed to be just upstream of that given by UTNS. When heat is added, CFLOW computes a shift downstream of the onset point that agrees with the UTNS solution to within 10%. Again, the onset point was computed to be upstream of that given by UTNS. Thus, CFLOW may be used to compute the location of recirculation onset. Due to the presence of a recirculation zone, this comparison is a more severe test of the quasi 1-D model's ability. However, the recirculation zone was of limited extent and strength, making this a less severe case than the next comparison.

The final comparison between CFLOW, quasi 1-D, and UTNS was both a qualitative and quantitative comparison for a recirculating flow. It involved comparison of the trends suggested by the quasi 1-D model and the resulting influence coefficients with the size and location of a recirculation zone computed by both CFLOW and UTNS for varying heat release and swirl ratio. It also involved quantitative comparison of the recirculation zone size and location computed by CFLOW and UTNS.

The recirculation zone was modeled in CFLOW by a low-mass-flow control volume on the centerline. This control volume represented the low-total-pressure streamtube that eventually determined when the recirculation zone formed. The initial area of this control volume was set based on the shear stress field given by the Navier-Stokes code. The remainder of the flowfield was represented by two larger control volumes, representing the remainder of the vortex core and the irrotational outer stream. The mixing coefficient was set to the empirically determined value of $\Xi = 4.0\nu_t$ for all cases. Heat was added to CFLOW while keeping everything else constant, and the reacting flow comparison was made.

CFLOW was run for the low and high swirl cases of Figures 5-3 and 5-4 with varying heat release. Since CFLOW uses the line of maximum shear stress to define the recirculation zone boundary, the locus of shear stress maxima for the UTNS solution is plotted along with the CFLOW computations for recirculation zone size and location. The recirculation zone boundaries from UTNS for a low swirl ($\Omega_0 = 0.5$) case with zero and high heat release ($\phi = 0,\ 0.8$) are shown in Figures 5-7a and b as solid lines. Recirculation zone boundaries from CFLOW are shown as the dashed lines. For low swirl, CFLOW computes recirculation zone volume to within 8% of that given by UTNS for zero

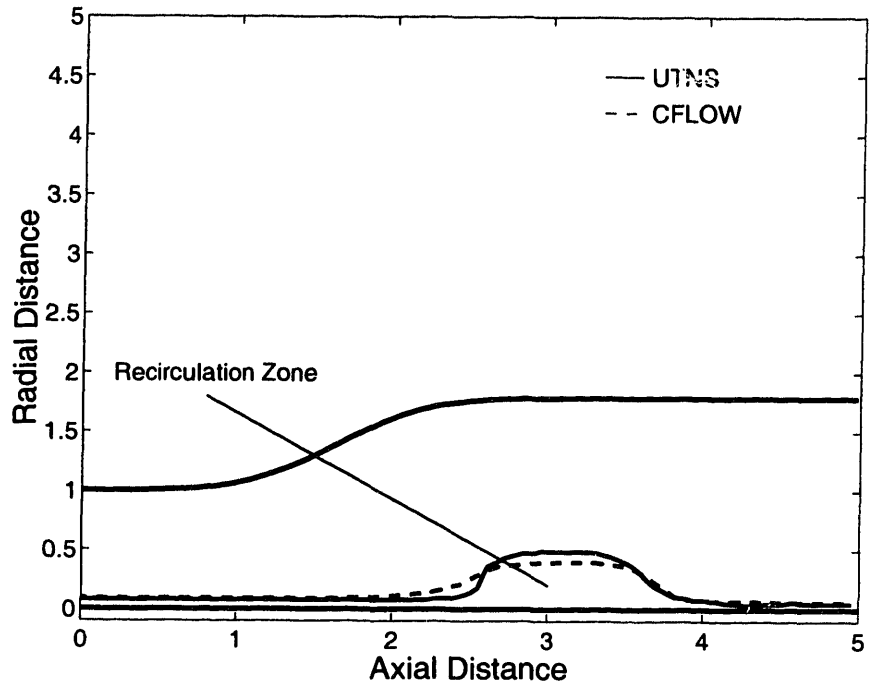

a) Zero Heat Release

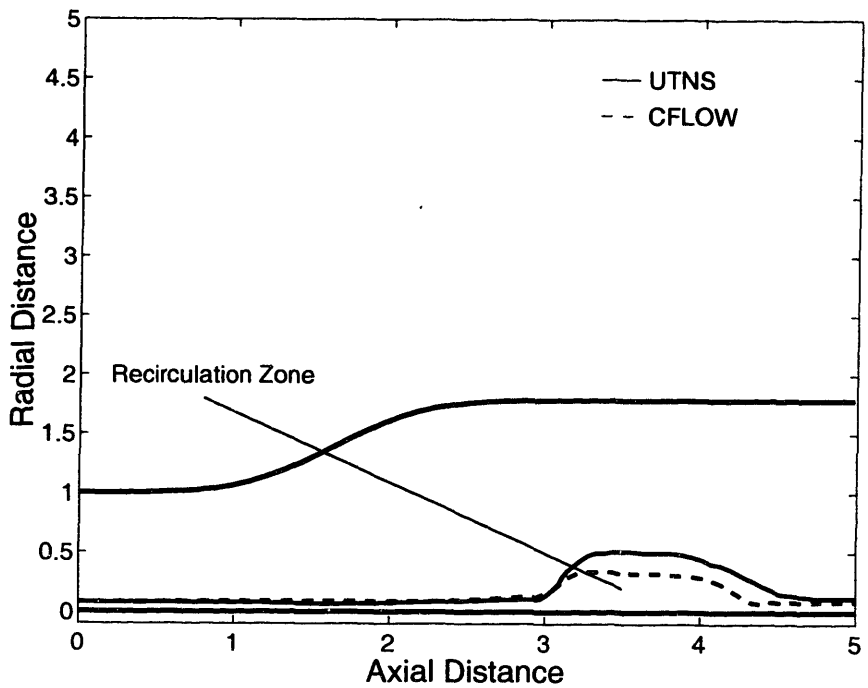

b) High Heat Release

Figure 5-7: Comparison of recirculation zone boundaries (shear stress maxima) from CFLOW (– –) and UTNS (–) for low swirl ($\Omega = 0.5$) at a) zero heat release ($\phi = 0.0$) and b) high heat release ($\phi = 0.8$).

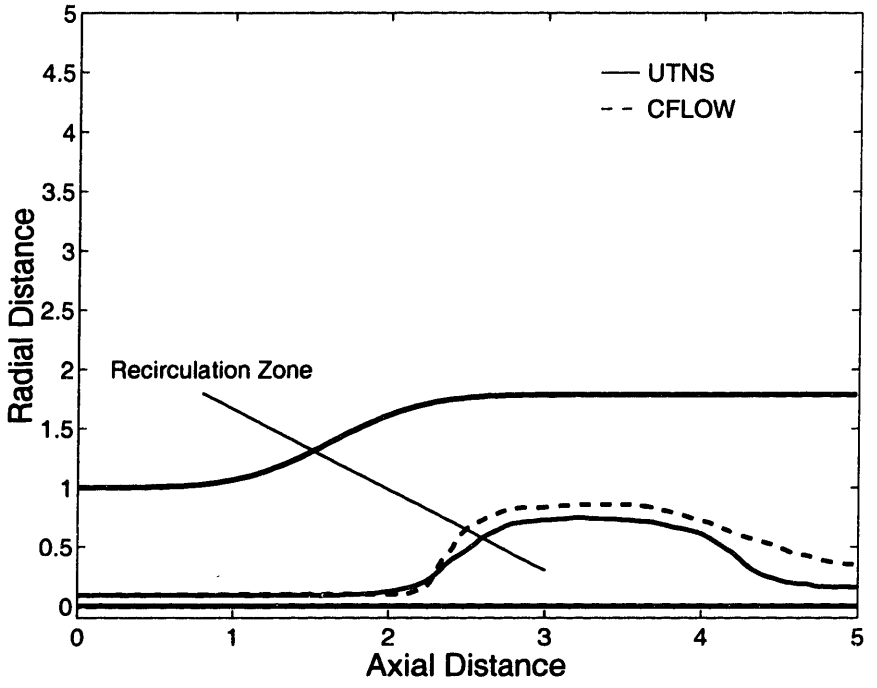

a) Zero Heat Release

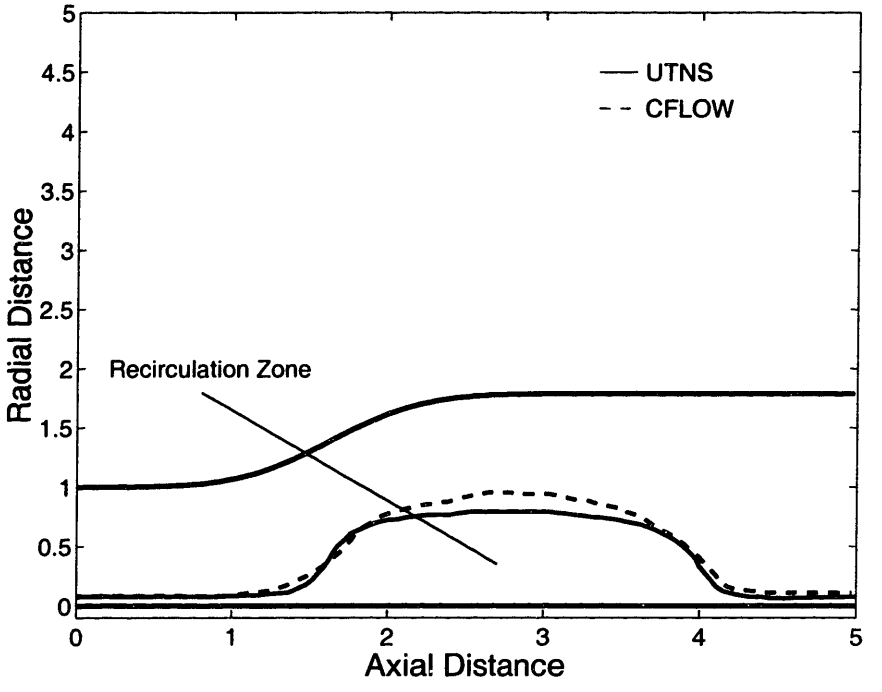

b) High Heat Release

Figure 5-8: Comparison of recirculation zone boundaries (shear stress maxima) from CFLOW (- -) and UTNS (-) for high swirl ($\Omega = 0.8$) at a) zero heat release ($\phi = 0.0$) and b) high heat release ($\phi = 0.8$).

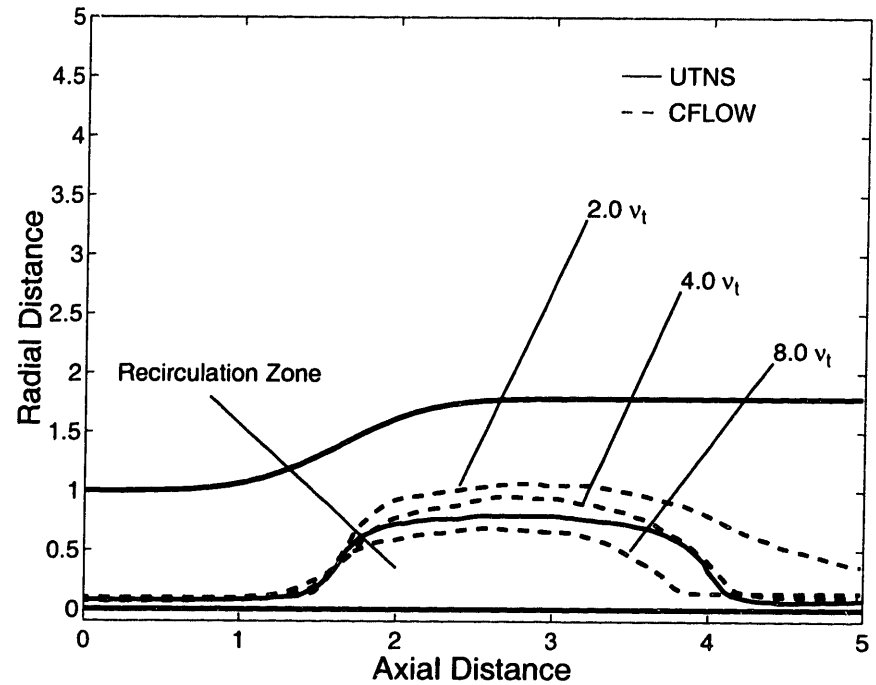

a) Mixing Sensitivity

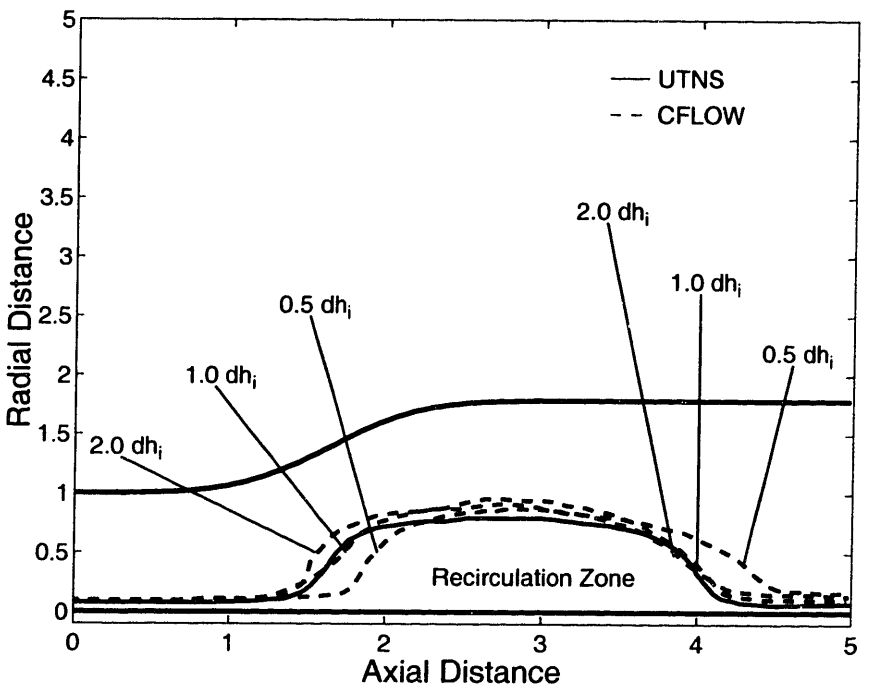

b) Heat Release Profile Sensitivity

Figure 5-9: Comparison of recirculation zone boundaries (shear stress maxima) from CFLOW (- -) and UTNS (-) for high swirl ($\Omega = 0.8$) and high heat release ($\phi = 0.8$) with a) variable mixing coefficient ($\Xi = 2.0, 4.0, 8.0\,\nu_t$) and b) variable heat release profile ($dh/dz = 0.5, 1.0, 2.0\,dh_i$).

heat release and to within 23% for high heat release. In addition, the low swirl behavior with heat release in the core as suggested by the influence coefficients is also seen in the CFLOW solutions.

A high swirl ($\Omega_0 = 0.8$) case with zero and high heat release ($\phi = 0, 0.8$) is shown in Figures 5-8a and b, respectively. For high swirl, CFLOW computes recirculation zone volume to within 12% of that given by UTNS for zero heat release and to within 11% for high heat release. In addition, the high swirl behavior with heat release in the core as suggested by the influence coefficients is also seen in the CFLOW solutions. These results, coupled with the severity of a highly recirculating flowfield, support the utility of CFLOW as a reduced-order design tool.

The sensitivity of the recirculation zone volume computed by CFLOW to changes in the mixing coefficient and differing heat release profiles was examined for the high swirl ($\Omega = 1.0$), high heat release ($\phi = 0.8$) case of Figure 5-8b. Mixing coefficient was run for the empirically determined value and both one-half and twice this value (*i.e.*, $\Xi = 2.0, 4.0, 8.0\,\nu_t$). The results are shown in Figure 5-9a. For the high mixing case ($\Xi = 8.0\nu_t$), the recirculation zone volume is less than that given by UTNS by 17%, giving a total change in recirculation volume of 28%. The linear sensitivity analysis suggests the change should be 26%. For the low mixing case ($\Xi = 2.0\nu_t$), the recirculation zone volume is 36% greater than that given by UTNS, yielding a total change in recirculation zone volume of 25%. The linear sensitivity analysis suggests the change should again be 26%. Thus, the computed sensitivities compare well with those from the sensitivity analysis.

The effect of changes in the heat release profile was examined by varying the slope of the heat release profile. The slope was specified to be one-half and double that of the normal heat release profile (*i.e.*, $dh/dz = 0.5, 1.0, 2.0\,dh_i$). For the more gradual heat release profile ($dh/dz = 0.5dh_i$), CFLOW computes a recirculation zone volume 13% greater than that given by UTNS, giving an overall change in recirculation zone volume of 2% for a decrease in the slope of one-half. For the sharper heat release profile ($dh/dz = 2.0dh_i$), CFLOW computes a recirculation zone volume 16% greater than that given by UTNS. This gives an overall change in recirculation zone volume of 5% for an increase in the slope of the heat release profile by a factor of two. It could be argued from these results, that while the magnitude of the heat release can have a large impact on the flowfield, recirculation zone volume is relatively insensitive to changes in the slope of the heat release profile for the range of profiles investigated.

5.3 CFLOW and UTNS vs. Experiment

A comparison of UTNS and CFLOW with a limited set of experimental data was carried out. The data chosen was that of Johnson, Roback, and Bennett[38]. This data set was chosen due to a closure of the recirculation zone well upstream of the duct exit plane. In many available data sets, non-closure of the recirculation zone at the duct exit makes computation of the flowfield difficult

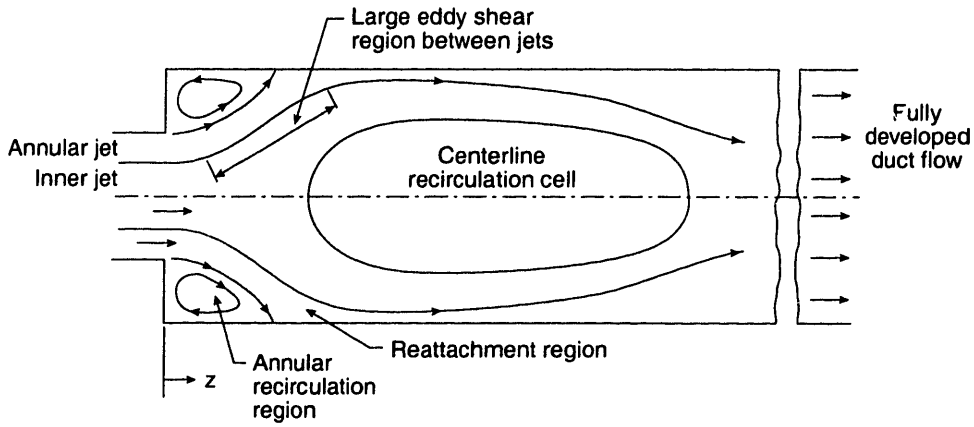

Figure 5-10: Schematic of the experimental facility and flowfield.

due to an undetermined pressure exit boundary condition. As a result, only a very limited data set was deemed appropriate.

Figure 5-10 shows a schematic of the experimental facility and a sketch of the flowfield set up for high swirl. For the swirling case, the inlet swirl ratio was $\Omega = 1.25$ with an inlet axial velocity ratio of 0.44. Both cases were for cold flow only. Laser velocimetry data for the centerline axial velocity was available for both swirling and nonswirling cases. In addition, radial profiles of axial and tangential velocity near the inlet ($z/R_0 = 0.2$) were available for the swirling case, and are shown in Figures 5-11 and 5-12. These conditions were used to compute the flowfield with both UTNS and CFLOW. The results are shown in Figure 5-13. The nonswirling case is represented by the upper set of curves, while the swirling case is represented by the lower set of curves. The x's and o's identify the experimental data points while the lines show the solutions from UTNS and CFLOW for each case.

For the nonswirling Navier-Stokes computation, the inlet total temperature and total pressure profiles were specified to be uniform, and the flow angle profile was set to zero. The exit static pressure was set to achieve the desired inlet mass flow. For the swirling Navier-Stokes computation, the inlet total temperature profile was set to uniform, and the total pressure and flow angle profiles were set to give the correct swirl and axial velocity profiles. The exit static pressure was set to achieve the desired inlet mass flow.

For the swirling CFLOW computation, a four control volume configuration was used. For the inner nonswirling stream, two control volumes were used, one which accounted for almost all of the inlet mass flow and a low-area, low-mass-flow control volume on the centerline which was used to model the recirculation zone. The flow splits between the two control volumes were chosen to have the same mass flow ratio utilized for the comparisons to UTNS solutions in Figures 5-6 through 5-8. The axial and tangential velocities were set equal to the experimental inner stream axial and tangential velocities. One control volume was used to model the swirling inlet stream. The axial

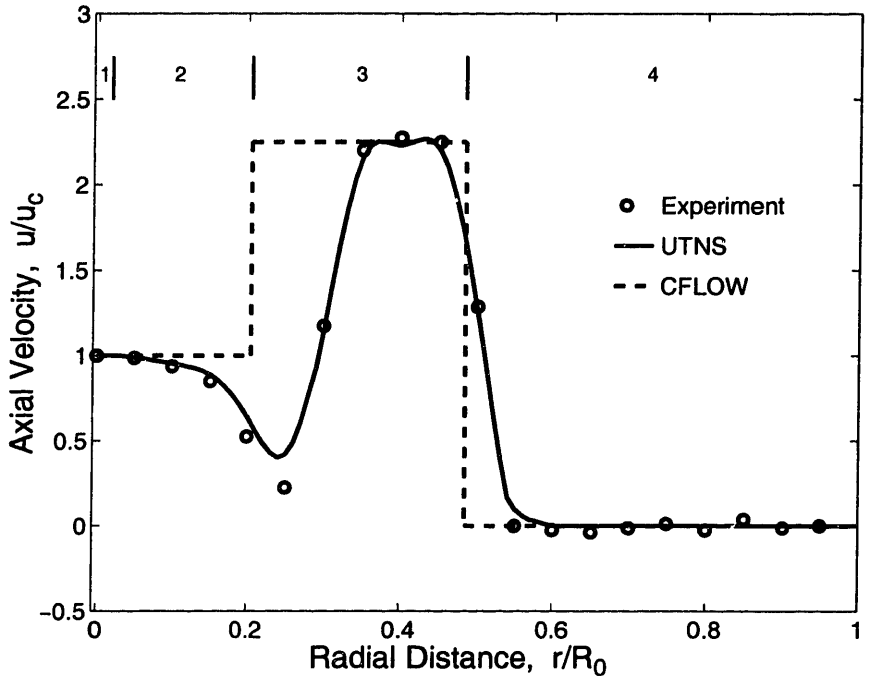

Figure 5-11: Comparison of Johnson, Roback, and Bennett inlet axial velocity data (o) to UTNS (-) and CFLOW (– –) for the swirling case with four control volumes in CFLOW (indicated by numbers at top).

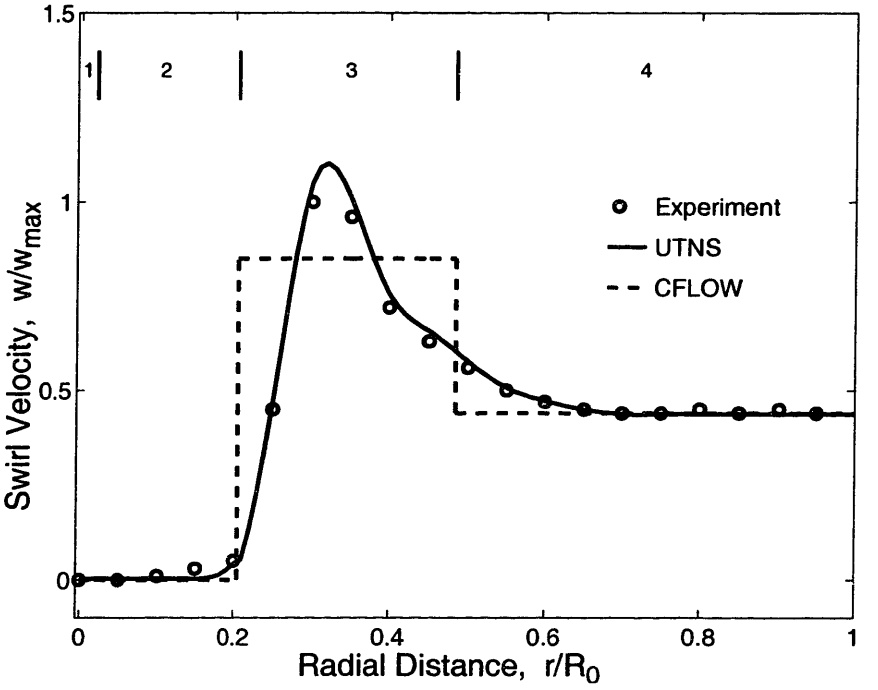

Figure 5-12: Comparison of Johnson, Roback, and Bennett inlet tangential velocity data (o) to UTNS (-) and CFLOW (– –) for the swirling case with four control volumes in CFLOW (indicated by numbers at top).

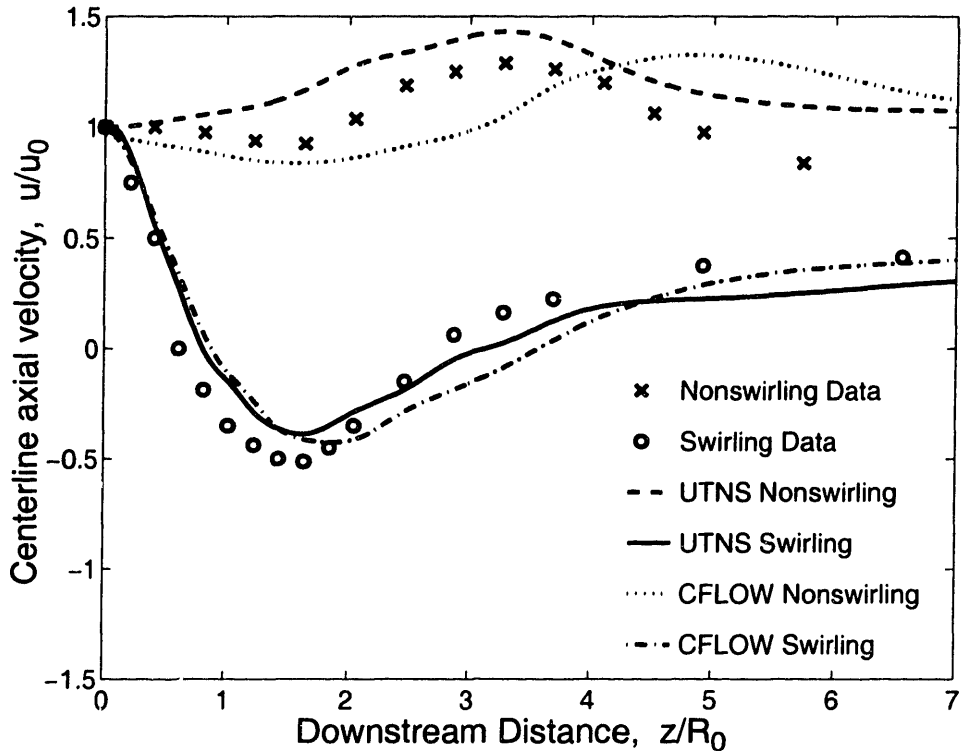

Figure 5-13: Comparison of Johnson, Roback, and Bennett centerline axial velocity data (o) to UTNS (-) and CFLOW (- -) for nonswirling and swirling cases with four control volumes in CFLOW.

velocity was set equal to the outer stream axial velocity, while the tangential velocity was set equal to the mass-averaged tangential velocity of the swirling stream. The outer rearward-facing step region was modeled using one control volume. The axial velocity was set to zero, and the tangential velocity was set to match the inlet swirl profile.

For the nonswirling CFLOW computation, a four control volume configuration was used with the flow splits equal to those for the swirling case. For the inner stream, two control volumes were used. Use of a low-mass-flow control volume on the centerline was not necessary since no recirculation zone forms on the centerline. However, this low-mass-flow control volume was retained to allow modeling with the same radial resolution as in the swirling case. The axial velocities were set equal to the experimental inner stream axial velocity. Zero tangential velocity was specified in all control volumes. One control volume was used to model the outer inlet stream. The axial velocity was set equal to the experimental outer stream axial velocity. The outer rearward-facing step region was modeled using one control volume. The axial velocity was set to zero.

The mixing coefficient was varied in CFLOW for the nonswirling and swirling cases. A mixing coefficient of $\Xi = 4.0\nu_t$ was determined to give the best match between CFLOW and the data for both nonswirling and swirling flows. This mixing coefficient was used in the comparison of CFLOW and UTNS described in Section 5.2.

Examining Figure 5-13, we see that the recirculating velocity at the centerline is half of the inlet free stream velocity, indicating a strong recirculation zone. The extent of the recirculation zone is several outer duct radii in length, indicating a large recirculation zone. Turning first to the nonswirling case, the maximum error in centerline axial velocity between the experimental data and UTNS is 34%. Although the trend in axial velocity is given by UTNS, the centerline axial velocity is computed to be greater than the experimental data at all points. For CFLOW, the maximum error in centerline axial velocity is 49%. The trend given by CFLOW is shifted downstream from the data by 1.5 duct radii. While neither UTNS nor CFLOW give accurate quantitative estimates for the centerline axial velocity in a nonswirling flow, trends are seen.

Looking now at the swirling case, we first examine the performance of the codes in computing the location of the recirculation zone leading edge (*i.e.*, the location of the first zero axial velocity point). Comparison with UTNS shows that the leading edge is computed to be 26% further downstream than measured, while comparison with CFLOW shows that the leading edge is computed to be 27% further downstream. Examining the location of the recirculation zone trailing edge (*i.e.*, the location of the second zero axial velocity point), UTNS computes a closure point 25% downstream of the measured closure point, while CFLOW computes the point to be 57% further downstream. The maximum error in the computed centerline axial velocity between the experimental data and UTNS is 22%, occurring downstream of the recirculation zone. For CFLOW, the maximum error in centerline axial velocity is 35%, occurring downstream of the recirculation zone. For the swirling case, the trends for recirculation zone size and location are given by UTNS and CFLOW. Therefore, while quantitative estimates of recirculation zone size and location are lacking, the overall behavior of the centerline axial velocity is captured.

The effect of varying the number of control volumes in CFLOW was examined for the experimental comparison described above. The number of streams was doubled from four to eight. Three control volumes were used to model the inner nonswirling stream (denoted as 1, 2, and 3 at the top of Figures 5-14 and 5-15). Control volume one is the low-area, low-mass-flow control volume used to model the recirculation zone. The flow splits between control volume one and control volumes 2 and 3 were chosen to have the same mass flow ratio utilized for the four control volume comparison. Four control volumes were used to model the swirling inlet stream (denoted as 4 through 7 at the top of Figures 5-14 and 5-15). The outer rearward-facing step region was modeled using one control volume. The axial and tangential velocities were set to match the experimental axial and tangential velocities. The mixing coefficient was varied in CFLOW for the nonswirling and swirling cases. A mixing coefficient of $\Xi = 4.0\nu_t$ was determined to give the best match between CFLOW and the data for both nonswirling and swirling flows. This mixing coefficient was the same as the empirically-determined mixing coefficient giving the best match to the experimental data for the four control volume model.

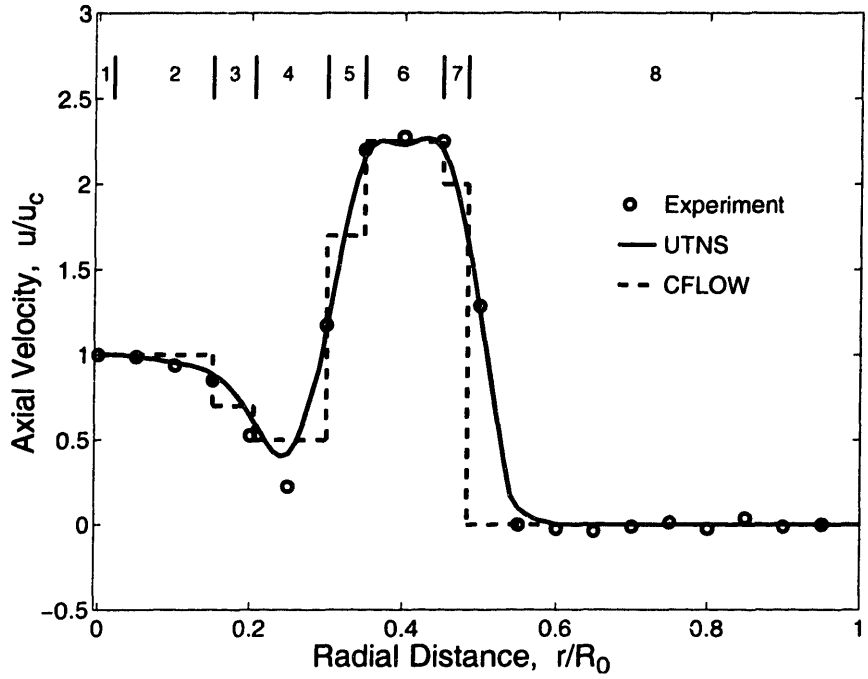

Figure 5-14: Comparison of Johnson, Roback, and Bennett inlet axial velocity data (o) to UTNS (-) and CFLOW (- -) for the swirling case with eight control volumes in CFLOW (indicated by numbers at top).

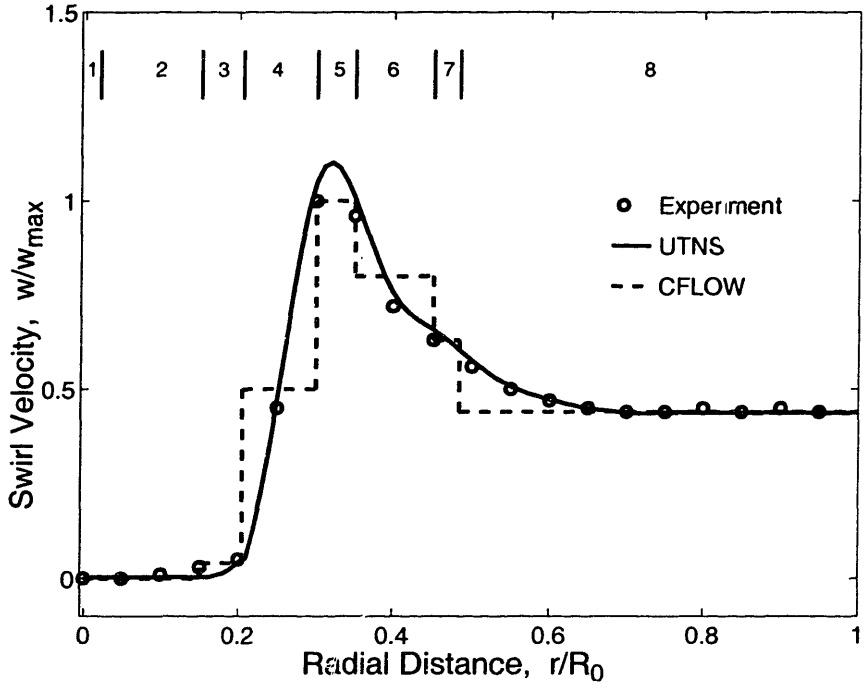

Figure 5-15: Comparison of Johnson, Roback, and Bennett inlet tangential velocity data (o) to UTNS (-) and CFLOW (- -) for the swirling case with eight control volumes in CFLOW (indicated by numbers at top).

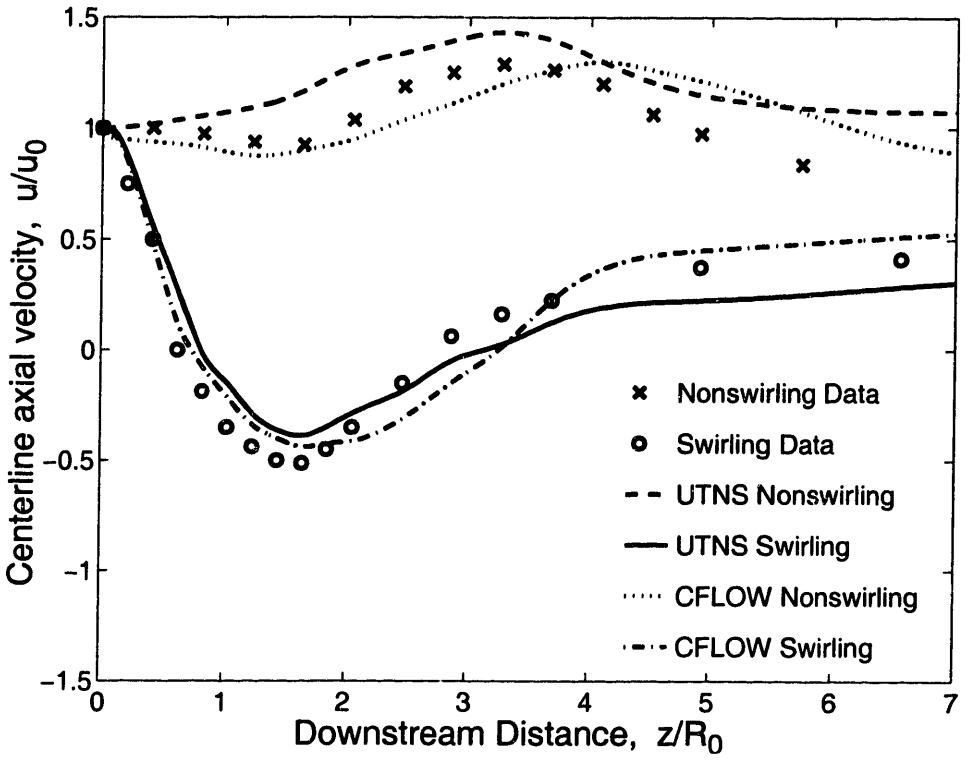

Figure 5-16: Comparison of Johnson, Roback, and Bennett centerline axial velocity data (o) to UTNS (–) and CFLOW (- -) for nonswirling and swirling cases with eight control volumes in CFLOW.

Examining Figure 5-16 for the the nonswirling case, the maximum error in centerline axial velocity between the experimental data and CFLOW is 36%. The trend given by CFLOW is shifted downstream from the data by 1.0 duct radii, but the magnitude of the peak in axial velocity agrees to within 5% of the experimental value. While CFLOW still does not give accurate quantitative estimates for the centerline axial velocity in a nonswirling flow, trends are again seen. The maximum error was also decreased from 49% to 36%.

Looking now at the swirling case, CFLOW computed the leading edge to be 7% further downstream than that given from the experimental data. Examining the location of the recirculation zone trailing edge, CFLOW computes the point to be 24% further downstream. The maximum error in the computed centerline axial velocity between the experimental data and CFLOW is 21%, occurring within the recirculation zone. For the swirling case, the trends for recirculation zone size and location are given by CFLOW. The comparison is better for the eight control volume model than for the four control volume model. This is expected due to the increased resolution in the radial direction. Therefore, while quantitative estimates of recirculation zone size and location are still lacking, the overall behavior of the centerline axial velocity is captured. The maximum error was decreased from 35% to 21%, and the computed onset point closely matched the experimental onset point.

5.4 Summary of Model Comparison

Summarizing the comparisons described above, it was shown that quasi 1-D analysis performed well for non-recirculating flows. In addition, the trends from the influence coefficients were apparent in the Navier-Stokes solutions. The quasi 1-D analysis thus has utility in yielding design trends.

CFLOW was shown to perform well in all comparisons with UTNS, yielding quantitative information on recirculation zone size and location for varying swirl and heat release. Comparison of UTNS and CFLOW with cold flow experimental data showed both models to capture the overall trends of the centerline axial velocity, and thus the trends in size and strength of a recirculation zone. CFLOW thus shows promise as a physics-based, reduced-order design tool.

Chapter 6

Application of CFLOW to a Lean-Premixed Combustor

CFLOW was applied to a lean premixed combustor for which solutions from a 3-D Navier-Stokes code were available at several operating conditions. The figure of merit in this comparison was the ability to compute recirculation zone size. For the current geometry, both inner and outer recirculation zones were present. However, examination of the 3-D solutions showed that the inner recirculation zone is the more important of the two in terms of flame stability.

This chapter begins with a description of the combustor flowfield in Section 6.1, followed by a discussion of the 3-D Navier-Stokes code in Section 6.2. Section 6.3 gives a discussion of how CFLOW was implemented for this flowfield. Finally, Section 6.4 presents the results of the comparison between CFLOW and the 3-D Navier-Stokes solutions.

6.1 Flowfield Description

The combustor being studied is an axisymmetric lean-premixed combustor running on natural gas. The section of the combustor where flame anchoring due to recirculation zone formation occurs is shown in Figure 6-1. There exists an inner and an outer step, both setting up recirculation zones for the zero swirl case. When swirl is added, the inner recirculation zone (*i.e.*, the recirculating region on the centerline of the duct) grows in extent and ensures a well-anchored flame.

The inlet flow is heated and the speeds are low enough for the flow to be taken as incompressible ($M < 0.3$). The combustor continues beyond the computational domain shown. However, the region of the combustor modeled contains the flame stabilization region, *i.e.*, the primary zone. Additionally, the presence of another rearward facing step downstream of the computational domain precluded computation of this region with CFLOW. Therefore, regions of the combustor downstream

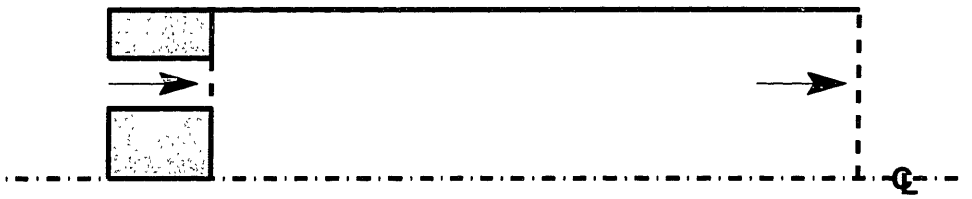

Figure 6-1: CFLOW computational domain for a lean-premixed combustor.

of the stated computational domain were not examined in this effort. Swirl is imparted to the entering flow upstream of the inlet plane. The swirl profile is that of a free vortex (*i.e.*, $1/r$ behavior).

6.2 Navier-Stokes Computations

The 3-D Navier-Stokes solver was a compressible, unsteady solver using an unstructured grid. Turbulence modeling employed a standard k-ϵ turbulence model. Combustion was handled by a global reaction mechanism for natural gas and air. The time dependent equations were discretized with a finite volume scheme and advanced temporally by a time-stepping procedure until steady state was reached. Total pressure and total temperature profiles were specified at the inlet, upstream of the swirler. Swirl was specified in the inlet duct by a vane angle in a potential swirler. Static pressure was specified at the exit.

6.3 Application of CFLOW

For the geometry and flowfield described in Section 6.1, three control volumes were used in CFLOW. One control volume represented the flow behind each of the rearward-facing steps, and the third control volume represented the swirling inlet flow. The axial and tangential velocities at the inlet were specified to be the same as the mass-averaged values from the 3-D Navier-Stokes solutions.

Heat release profiles were determined from the Navier-Stokes solutions and used as inputs to CFLOW. The profiles were similar to the typical heat release profile shown in Figure 2-2 for the quasi 1-D model. The mixing coefficient was set equal to the empirically determined value of $\Xi = 4.0\nu_t$ from Section 5.3.

6.4 Results of Comparison

The shear stress field was computed for the 3-D solutions and used to determine the recirculation zone boundaries based on the maxima in shear stress. The 3-D solutions were compared to the results from CFLOW. Figures 6-2 and 6-3 show these comparisons

Figures 6-2 and 6-3 are for a high swirl case with swirl ratio of $\Omega = 1.0$. Figure 6-2 shows the comparison for a zero heat release case, while Figure 6-3 shows the comparison for a typical lean heat release ($\phi = 0.55$). CFLOW computes the inner recirculation zone volume for the zero heat release case to be less than that given by the 3-D code by 18%. This is regarded as quite good for a three stream control volume model. For the case with heat release, CFLOW computes the inner recirculation zone volume to be less than that given by the 3-D code by 11%. The 3-D solutions suggest an overall change in recirculation zone volume between the cold and hot flows of 78%. Results of a sensitivity analysis for these cases were presented in Section 3.5.

These comparisons show that CFLOW is a useful reduced-order model, able to compute recirculation zone volumes to within 20%. This, coupled with a large difference in computational efficiency between CFLOW and a 3-D Navier-Stokes code (minutes vs. weeks), identifies CFLOW as a promising combustor front-end analysis tool.

The sensitivity of the recirculation zone volume computed by CFLOW to changes in the mixing coefficient and differing heat release profiles was examined for the high swirl ($\Omega = 1.0$), typical heat release ($\phi = 0.55$) case of Figure 6-3. Mixing coefficient was run for the empirically determined value and both one-half and twice this value (*i.e.*, $\Xi = 2.0, 4.0, 8.0\,\nu_t$). The results are shown in Figure 6-4a. For the high mixing case ($\Xi = 8.0\nu_t$), the recirculation zone volume is less than that given by the 3-D code by 19%, giving a total change in recirculation volume of 8%. The linear sensitivity analysis suggests the change should be 11%. For the low mixing case ($\Xi = 2.0\nu_t$), the recirculation zone volume is 9% greater than that given by the 3-D code, yielding a total change in recirculation zone volume of 20%. The linear sensitivity analysis suggests the change should again be 11%. Thus, the computed sensitivities compare reasonably well with those from the sensitivity analysis.

The effect of changes in the heat release profile was examined by varying the slope of the heat release profile, shown schematically in Figure 2-2. The slope was specified to be one-half and double that of the normal heat release profile (*i.e.*, $dh/dz = 0.5, 1.0, 2.0\,dh_i$). For the more gradual heat release profile ($dh/dz = 0.5dh_i$), CFLOW computed a recirculation zone volume 7% greater than that given by the 3-D code, giving an overall change in recirculation zone volume of 18% for a decrease in the slope of one-half. For the sharper heat release profile ($dh/dz = 2.0dh_i$), CFLOW computes a recirculation zone volume 25% less than that given by the 3-D code. This gives an overall change in recirculation zone volume of 14% for an increase in the slope of the heat release profile by a factor of two.

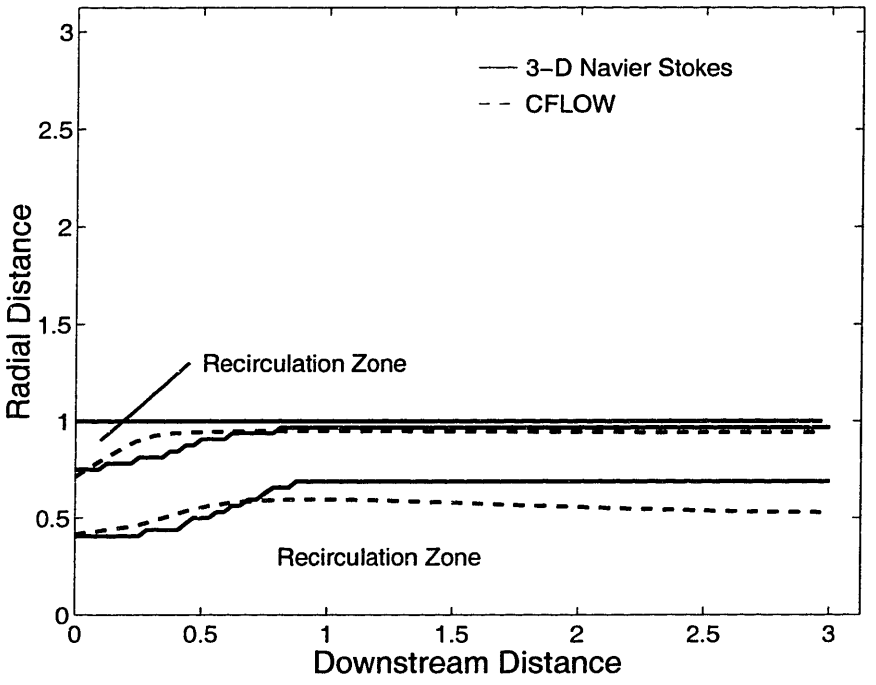

Figure 6-2: Comparison of recirculation zone boundaries (shear stress maxima) from CFLOW (– –) and 3-D Navier-Stokes (–) for high swirl ($\Omega = 1.0$) and zero heat release ($\phi = 0.0$).

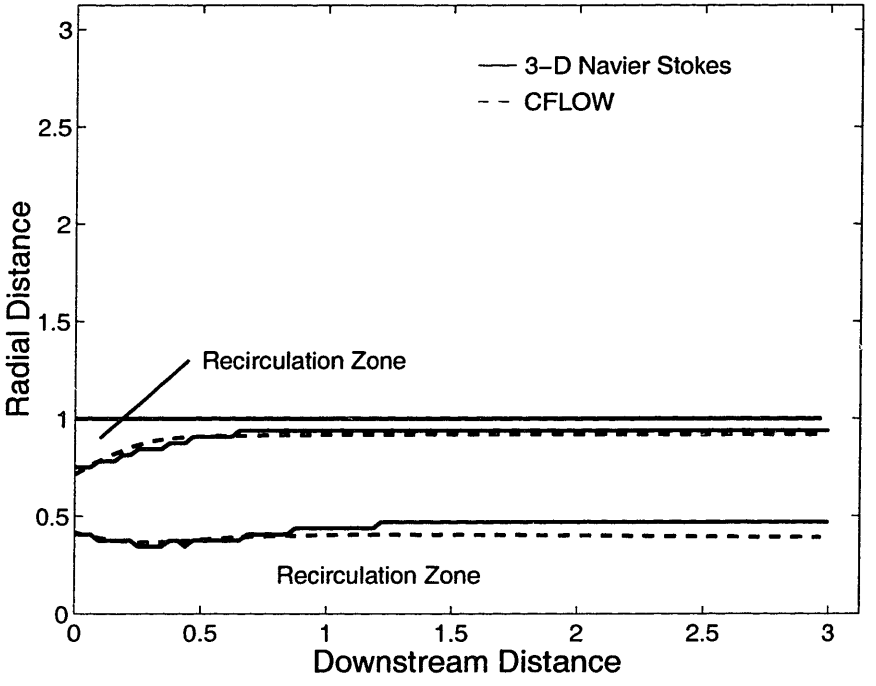

Figure 6-3: Comparison of recirculation zone boundaries (shear stress maxima) from CFLOW (– –) and 3-D Navier-Stokes (–) for high swirl ($\Omega = 1.0$) and typical lean heat release ($\phi = 0.55$).

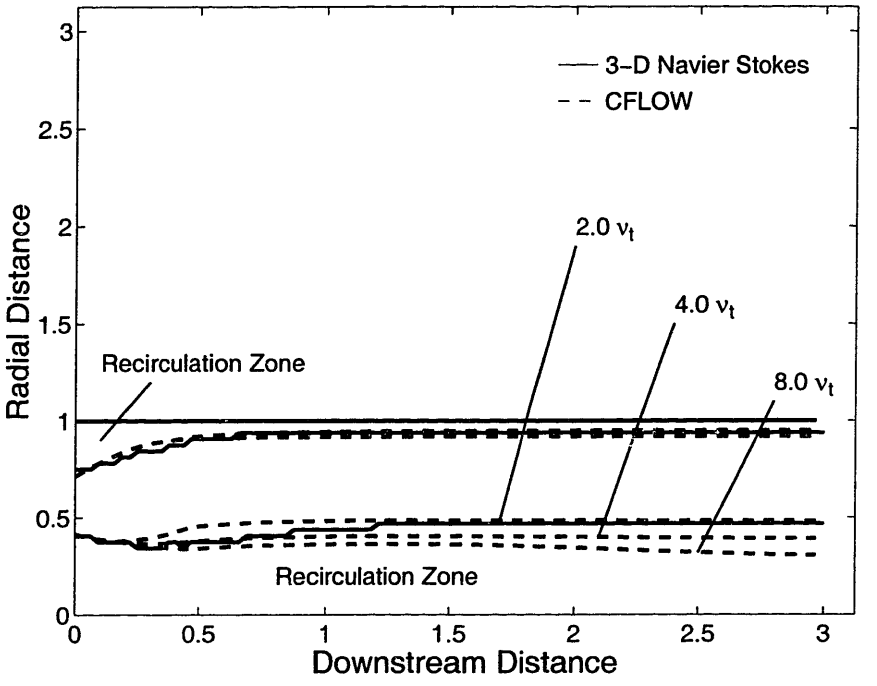

a) Mixing Sensitivity

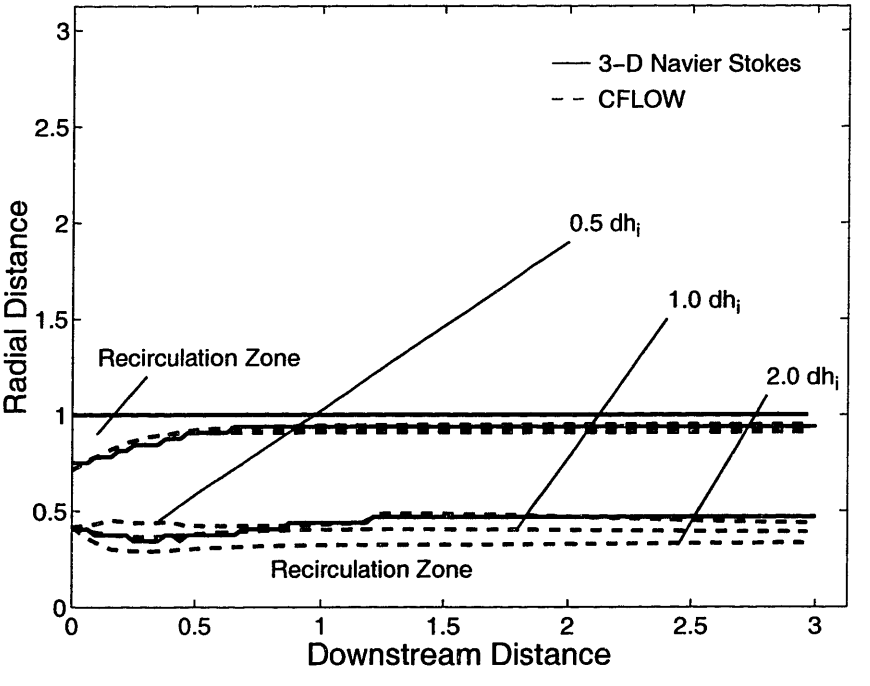

b) Heat Release Profile Sensitivity

Figure 6-4: Comparison of recirculation zone boundaries (shear stress maxima) from CFLOW (– –) and 3-D Navier-Stokes (–) for high swirl ($\Omega = 0.8$) and typical lean heat release ($\phi = 0.55$) with a) variable mixing coefficient ($\Xi = 2.0, 4.0, 8.0\,\nu_t$) and b) variable heat release profile ($dh/dz = 0.5, 1.0, 2.0\,dh_i$).

Chapter 7

Summary, Conclusions, and Recommendations

Reduced-order models of primary zone flows have been developed and evaluated. These include *(i)* a quasi-one-dimensional (quasi 1-D) control volume analysis including a set of influence coefficients, *(ii)* a streamline curvature code, *(iii)* a quasi 1-D control volume analysis with recirculation (CFLOW), and *(iv)* a Reynolds-averaged axisymmetric Navier-Stokes code (UTNS). The differing levels of approximations in the models were assessed through their inter-comparison, as well as through comparison with experimental data. The utility of these models as a preliminary design tool was then evaluated through application of the models to a combustor.

7.1 Conclusions

Several conclusions can be drawn from the work presented here.

1. *Reduced-order models can provide a useful tool for increasing the physical insight and understanding of confined swirling flows with heat release across flow regimes of interest in gas turbine combustors.* In the present work, for example, the quasi 1-D model and influence coefficients helped elucidate counter-intuitive high swirl behavior of recirculation zone size with respect to heat release, behavior which had been observed, but not explained until this analysis. Further, trends for all flow variables as a function of area change, heat release, and mixing were described.

2. *Reduced-order models can provide useful combustor front-end analysis tools.* The comparison of CFLOW and a 3-D Navier-Stokes solution of a lean-premixed combustor showed that after calibration of the heat release and mixing models this reduced-order model can compute

recirculation zone size and location in agreement with higher-order methods. Computational efficiency and the availability of sensitivity information enable this model as a parametric analysis tool.

3. *Accurate modeling of the mixing on the downstream boundary of a recirculation zone is necessary for computation of confined recirculating flows with heat addition.* For the current formulation, mixing models must account for both Reynolds stresses and bulk transport across the interface. Neglecting the transport terms results in non-closure of recirculation zones.

4. *Accurate modeling of the heat release over the entire flowfield is necessary for computation of confined recirculating flows with heat addition.*

5. *Simplified mixing and heat release models have limitations arising from the need to input the amount of mixing or heat release present.* Calibration of these parameters with higher-fidelity computations and experiments allowed comparison of the models across the flow regimes of interest. This calibration was similar to that necessary in higher-fidelity CFD codes. Following calibration of the mixing and heat release models, CFLOW was able to compute recirculation zone volumes to within 25% of those given by both the axisymmetric and three-dimensional Navier-Stokes codes for swirl ratios between 0.5 and 1.0 and equivalence ratios between 0.0 and 0.8.

7.2 Recommendations

CFLOW has shown potential for further development, and there are several possible directions in which to take the code. These possibilities and a brief discussion of each will be presented next.

7.2.1 Flame Sheet Model

Currently heat release must be specified in CFLOW. However, this could be eliminated through use of a flame sheet model. This entails orienting the flame such that the normal velocity to the flame front is equal to the flame speed. This could be written as a separate module that would be called by subroutine RCELL. The flame sheet module would orient the flame based on the current velocity field, returning the locus of the flame front. This would be used by RCELL to compute the heat release field and specify the value of the chemical source term at each point in the flowfield.

7.2.2 k-ϵ Model

Currently mixing must be specified in CFLOW based on a planar shear layer growth rate. However, a k-ϵ model or similar higher-order mixing model could be incorporated. The model could be incorporated into subroutine RSTRM for calculation of the mixing terms.

7.2.3 Heat Transfer Model

In a real gas turbine flowfield, other heat transfer considerations exist. In particular, radiation from soot could contribute a significant amount in the total heat transfer of the fluid. This could be handled by determining the emissivity of the soot particles and using the Stefan-Boltzmann law to relate the temperature of the soot particles to the heat transfer. This heat transfer would then become another term in the energy equation.

7.2.4 Combustor Exit Model

CFLOW could be coupled to a separate model for the dilution zone and exit of a combustor. The pressure at the inlet to this model could be passed to CFLOW in the subroutine RCELL and specified as the exit pressure in the primary zone calculation. This would provide a global model of the combustor.

7.2.5 Recirculation Zone Dynamics

Recirculation zone dynamics could be studied by examining the sensitivity of the flowfield to changes in the downstream pressure at a given radial location. This would involve modification of the existing sensitivity analysis to give information about recirculation volume changes as a function of changes in pressure at a given radial location in the exit plane. A brief outline of the formulation for this sensitivity is given in Appendix D.

7.2.6 Unsteady CFLOW

The potential exists to extend the steady-state CFLOW formulation to unsteady flows. A steady analysis similar to that of CFLOW has been extended to unsteady flows. A brief description of this extension and the modifications necessary for inclusion of mixing terms is given in Appendix E.

7.2.7 Sensitivity to Design Variables

The capability exists to extend CFLOW for design variable optimization purposes. The first step in this extension involves a linear sensitivity analysis of the optimization variables. These variables could include parameters such as the geometry or the inlet distributions of swirl velocity, axial velocity, or fuel-air ratio. Each optimization variable is stored in a separate column of the δR matrix. This is called D in CFLOW. When the system is solved, the sensitivities of the optimization variables are returned along with the flowfield solution.

Bibliography

[1] Gupta, A. K., Beér, J. M., Swithenbank, J., "Concentric Multi-Annular Swirl Burner: Stability Limits and Emission Characteristics," *Sixteenth Symposium (International) on Combustion*, The Combustion Institute, 1976, pp. 79-91.

[2] Gupta, A. K., Modarres-Razavi, M. R., Marchionna, N., "Experimental and Theoretical Studies in the Controlled Mixing Variable Geometry Combustor," *Joint Propulsion Conference*, Boston, MA, July 1988, AIAA Paper 88-2857.

[3] Gupta, A. K., Ramavajjala, M., Taha, M., "The Effect of Swirl and Nozzle Geometry on the Structure of Flames and NO_x Emission," *Aerospace Sciences Meeting*, Reno, NV, January 1992, AIAA Paper 92-0766.

[4] Gupta, A. K., Ramavajjala, M., "Swirl Combustor Design Effects on Emission and Combustion Characteristics," *Aerospace Sciences Meeting*, Reno, NV, January 1990, AIAA Paper 90-0548.

[5] Gupta, A. K., Ramavajjala, M., "The Effect of Combustor Dome Geometry on the Structure of Flames and NO_x Emission," *Joint Propulsion Conference*, Nashville, TN, July 1992, AIAA Paper 92-3344.

[6] Milosavljevic, V. D., Taylor, A. M. K. P., Whitelaw, J. H., "The Influence of Burner Geometry and Flow Rates on the Stability and Symmetry of Swirl-Stabilized Nonpremixed Flames," *Combustion and Flame*, Vol. 80, 1990, pp. 196-208.

[7] Bicen, A. F., Tse, D. G. N., Whitelaw, J. H., "Combustion Characteristics of a Model Can-Type Combustor," *Combustion and Flame*, Vol. 80, 1990, pp. 111-125.

[8] Koutmos, P., McGuirk, J. J., "Isothermal Modeling of Gas Turbine Combustors: Computational Study," *Journal of Propulsion and Power*, Vol. 7, no. 6, Nov-Dec 1991, pp. 1064-1071.

[9] Escudier, M., "Confined Vortices in Flow Machinery," *Annual Review of Fluid Mechanics*, Vol. 19, 1987, pp. 27-52.

[10] Gupta, A. K., Lilley, D. G., "Combustion and Environmental Challenges for Gas Turbines in the 1990s," *Joint Propulsion Conference*, Sacramento, CA, June 1991, AIAA Paper 91-1964.

[11] Lilley, D. G., "Turbulent Swirling Reacting Flow," *Aerospace Sciences Meeting*, Reno, NV, January 1994, AIAA Paper 94-0113.

[12] Rizk, N. K., Mongia, H. C., "Gas Turbine Combustor Design Methodology," *Joint Propulsion Conference*, Huntsville, AL, June 1986, AIAA Paper 86-1531.

[13] Mellor, A. M., Fritsky, K. J., "Turbine Combustor Preliminary Design Approach," *Journal of Propulsion and Power*, Vol. 6, no. 3, May-June 1990, pp. 334-343.

[14] Wilson, K. J., Schadow, K. C., Gutmark, E., Smith, R. A., "Effect of Spin on Mixing and Combustion in a Circular Duct," *Joint Propulsion Conference*, Boston, MA, July 1988, AIAA Paper 88-2861.

[15] Sullivan, J. P., Barron, D., Seal, M., Morgan, D., Murthy, S. N. B., "Primary Zone Dynamics in a Gas Turbine Combustor," *Aerospace Sciences Meeting*, Reno, NV, January 1989, AIAA Paper 89-0489.

[16] Richards, C. D., Samuelsen, G. S., "The Interaction of Primary Jets with a Swirl-Induced Recirculation Zone," *Aerospace Sciences Meeting*, Reno, NV, January 1990, AIAA Paper 90-0455.

[17] Roquemore, W. M., Reddy, V. K., Hedman, P. O., Post, M. E., Chen, T. H., Goss, L. P., Trump, D., Vilimpoc, V., Sturgess, G. J., "Experimental and Theoretical Studies in a Gas-Fueled Research Combustor," *Aerospace Sciences Meeting*, Reno, NV, January 1991, AIAA Paper 91-0639.

[18] Anderson, L. R., Heiser, W. H., Jackson, J. C., "Axisymmetric One-Dimensional Compressible Flow-Theory and Applications," *Journal of Engineering for Power*, 1970, Paper No. 70-GT-82.

[19] Nikjooy, M., So, R. M. C., "On the Modelling of Scalar and Mass Transport in Combustor Flows," *International Journal for Numerical Methods in Engineering*, Vol. 28, 1989, pp. 861-877.

[20] Chao, Y. C., "Recirculation Structure of the Coannular Swirling Jets in a Combustor," *AIAA Journal*, Vol. 26, no. 5, May 1988, pp. 623-625.

[21] Sturgess, G. J., Syed, S. A., "Calculation of Confined Swirling Flows," *Aerospace Sciences Meeting*, Reno, NV, January 1985, AIAA Paper 85-0060.

[22] Rizk, N. K., Mongia, H. C., "Gas Turbine Combustor Performance Evaluation," *Aerospace Sciences Meeting*, Reno, NV, January 1991, AIAA Paper 91-0640.

[23] Borissov, A., Shtern, V., Hussain, F., "Modeling Flow and Heat Transfer in Vortex Burners," *AIAA Journal*, Vol. 36, no. 9, September 1998, pp. 1665-1670.

[24] Darmofal, D. L., Khan, R., Greitzer, E. M., Tan, C. S., "A Quasi One-Dimensional Model for Vortex Cores," Internal Gas Turbine Laboratory Report, 1997.

[25] Khan, R., "A Quasi One-Dimensional Analysis for Confined Vortex Cores," S.M. Thesis, Mass. Institute of Tech., 1995.

[26] Beér, J. M., Chigier, N. A., *Combustion Aerodynamics*, Robert E. Krieger Publishing Company, 1972.

[27] Kerrebrock, J. L., *Aircraft Engines and Gas Turbines*, The MIT Press, 1977.

[28] Schlichting, H., *Boundary Layer Theory*, McGraw-Hill Book Company, 1955.

[29] Tew, D. E., "Streamwise Vorticity Enhanced Compressible Mixing Downstream of Lobed Mixers," Ph.D. Thesis, Mass. Institute of Tech., 1997.

[30] Hermanson, J. C., Dimotakis, P. E., "Effects of Heat Release in a Turbulent, Reacting Shear Layer," *Journal of Fluid Mechanics*, Vol. 199, 1989, pp. 333-375.

[31] Shapiro, A. H., Hawthorne, W. R., "The Mechanics and Thermodynamics of Steady, One-Dimensional Gas Flow," *Journal of Applied Mechanics*, Vol. 14, No. 4, December 1947, pp. A-317-336.

[32] Shapiro, A. H., *The Dynamics and Thermodynamics of Compressible Fluid Flow*, The Ronald Press Company, New York, 1953.

[33] Oates, G. C., *Aerothermodynamics of Aircraft Engine Components*, American Institute of Aeronautics and Astronautics, New York, 1985.

[34] Underwood, D. S., "Effect of Heat Release on Streamwise Vorticity Enhanced Mixing," S.M. Thesis, Mass. Institute of Tech., 1995.

[35] Lefebvre, A. H., *Gas Turbine Combustion*, Hemisphere Publishing Corp., New York, 1983.

[36] Mellor, A. M., *Design of Modern Turbine Combustors*, Academic Press Ltd., San Diego, 1990.

[37] Wake, B. E., Choi, D., Hendricks, G., "Numerical Investigation of Pre-Mixed Step-Combustor Instabilities," *Aerospace Sciences Meeting*, Reno, NV, January 1996, AIAA Paper 96-0816.

[38] Johnson, B. V., Roback, R., Bennett, J. C., "Scalar and Momentum Turbulent Transport Experiments with Swirling and Nonswirling Flows," *Experimental Measurements and Techniques in Turbulent Reactive and Non-reactive Flows Meeting*, New Orleans, LA, December 1984, pp.107-119.

[39] Drela, M., *Unsteady MSES Formulation*, MIT Fluid Dynamics Research Laboratory, 1996.

[40] Drela, M., *A User's Guide to MTFLOW 1.2, Multi-passage ThroughFLOW Design/Analysis Program*, MIT Fluid Dynamics Research Laboratory, 1997.

Appendix A

Streamline Curvature Model

The potential of a streamline curvature model (MTFLOW) developed by Drela[40] was investigated for computing recirculating flows with heat release. The model was run for cases with varying swirl and heat release and rejected for further development due to poor performance in computing recirculating cases. The model performed adequately for the non-recirculating case.

The formulation for the streamline curvature is essentially the same as for the quasi 1-D model with the addition of radial curvature terms in the momentum equation. Also, the streamline curvature code does not account for shear stresses, their associated work, or conduction between adjacent streamtubes. Therefore, the streamline curvature model can be thought of as the inviscid multi-streamtube limit of the quasi 1-D model. Figure A-1 shows a schematic for the streamlines in MTFLOW for a non-recirculating case.

The MTFLOW formulation does not solve the differential continuity equation, but instead explicitly prescribes a constant mass flow m along each streamtube. The meridional speed q is then obtained from

$$q = \frac{m}{\rho A(2\pi r - BT_\theta)}, \tag{A.1}$$

where A is the cross-sectional thickness of the streamtube. The B and T_θ field parameters act to restrict the flow area.

As with continuity, MTFLOW does not solve the differential energy equation, but instead ex-

Figure A-1: Schematic of MTFLOW streamlines for a non-recirculating flow.

plicitly prescribes the total enthalpy h_0 at every point in the flowfield using the relation

$$h_0 = h_{inl} + \frac{1}{2}{q_{inl}}^2 + \Delta H. \tag{A.2}$$

A fully-implicit treatment would require solving the energy equation in differential form at a considerable increase in computational time per Newton iteration.

The streamwise momentum equation is taken to have the form

$$dp + \rho q\, dq + \rho V_\theta\, dV_\theta + p\, d(\Delta S) = 0, \tag{A.3}$$

where differentials $d(\,)$ are taken along a streamsurface. The swirl-velocity differential dV_θ is differenced as $d(rV_\theta) - V_\theta\, dr$ to exactly conserve circulation.

The entropy is defined as

$$S \equiv \ln\left[\frac{(h/h_{inl})^{\gamma/(\gamma-1)}}{p/p_{inl}}\right], \tag{A.4}$$

so that $S_{inl} = \ln(1) = 0$ by definition. The total enthalpy is related to the static enthalpy and all velocity components as

$$h_0 \equiv h + \frac{1}{2}V_z^2 + \frac{1}{2}V_r^2 + \frac{1}{2}V_\theta^2 \;=\; h + \frac{1}{2}q^2 + \frac{1}{2}V_\theta^2. \tag{A.5}$$

With these definitions, the streamwise momentum equation can be manipulated into the entropy-convection equation with the imposed source terms due to heat addition and adiabatic loss

$$-p\, dS + p\, d(\Delta S) + \rho\, d(\Delta H) = 0. \tag{A.6}$$

Equation A.6 can optionally replace the momentum equation in all or part of the flowfield. The two equations are formally equivalent in differential form, so this is perfectly legitimate. However, the two equations have different truncation errors on finite grids.

The initial streamline pattern generated by MTFLOW corresponds to incompressible, inviscid flow, which may be quite different from the actual flow if significant swirl or heat release is being imposed. The Newton solver is used to compute the flow only within the inviscid region of the flow. For separated or recirculating regions, an interactive boundary-layer model is used to approximate

the flow within the separated/recirculating region. The flow is then regridded to encompass only the inviscid region, being deflected from the wall by an effective displacement thickness.

The result of this regridding is to approximate the viscous recirculating region, while computing the inviscid, non-recirculating region. For a large swirl ratio, the radial extent of the recirculation zone can approach the duct height. Therefore, for highly recirculating cases, a large fraction of the duct is approximated, and a small portion is computed. This leads to unbounded growth in the recirculation zone due to insufficient modeling of the viscous mixing and mass transfer through the second half of the recirculation zone boundary. In other words, the mechanism for the closure of a recirculation zone is not modeled properly by the streamline curvature code. The poor performance of MTFLOW in modeling recirculating flows in conjunction with the availability of a quasi 1-D model which modeled non-recirculating flow well resulted in rejection of the streamline curvature model for further development.

Appendix B

Details of Newton Matrix

As discussed in Chapter 3, the first step in the CFLOW solution process is setting up the Newton matrix. This involves discretizing the conservation equations and placing the terms in their proper positions inside the Newton matrix. The Newton matrix represents the partial derivatives of the conservation equations with respect to the state variables (*i.e.*, the Jacobian).

Figure B-1 shows the full Newton matrix for a three-stream flowfield (as depicted in Figure 3-1) on a grid with twenty steps in the axial direction. The matrix is tri-diagonal due to upstream and downstream effects on a given cell.

The notation (column #, row #) will be used to index the blocks in the Newton matrix. The first block (1,1) represents the specified inlet conditions. The last block (20,20) represents a set of dummy exit conditions in order to allow for proper discretization of the equations. Block (19,20) represents the imposed pressure exit condition in each stream. On the interior of the matrix, the main diagonal block (i,i) represents the flow at axial grid point i for all three streams ($j = 1, 2, 3$). Block ($i-1$,i) represents the upstream influence from grid point $i-1$ on the solution at i, while block ($i+1$,i) represents the downstream influence from $i+1$ on the solution at i. Thus, the upper diagonal is the downstream influence, and the lower diagonal is the upstream influence.

A blow-up of the first few grid points of the Newton matrix is given in Figure B-2. It shows that within each block, there are 6x6 sub-blocks for each stream at each axial grid point. Within each of these sub-blocks, the value of the derivative of each conservation equation with respect to each state vector (*i.e.*, the Jacobian) is stored. A row represents a conservation equation, and a column represents the influence of a state from the state vector. Therefore, rows one through six within a block represent the continuity, axial momentum, energy, tangential momentum, radial momentum, and state equations, respectively, for the innermost stream. The next six rows represent the second stream, and the last six represent the third stream. The columns are ordered according to state variables. Therefore, columns one through six represent density, axial velocity, temperature,

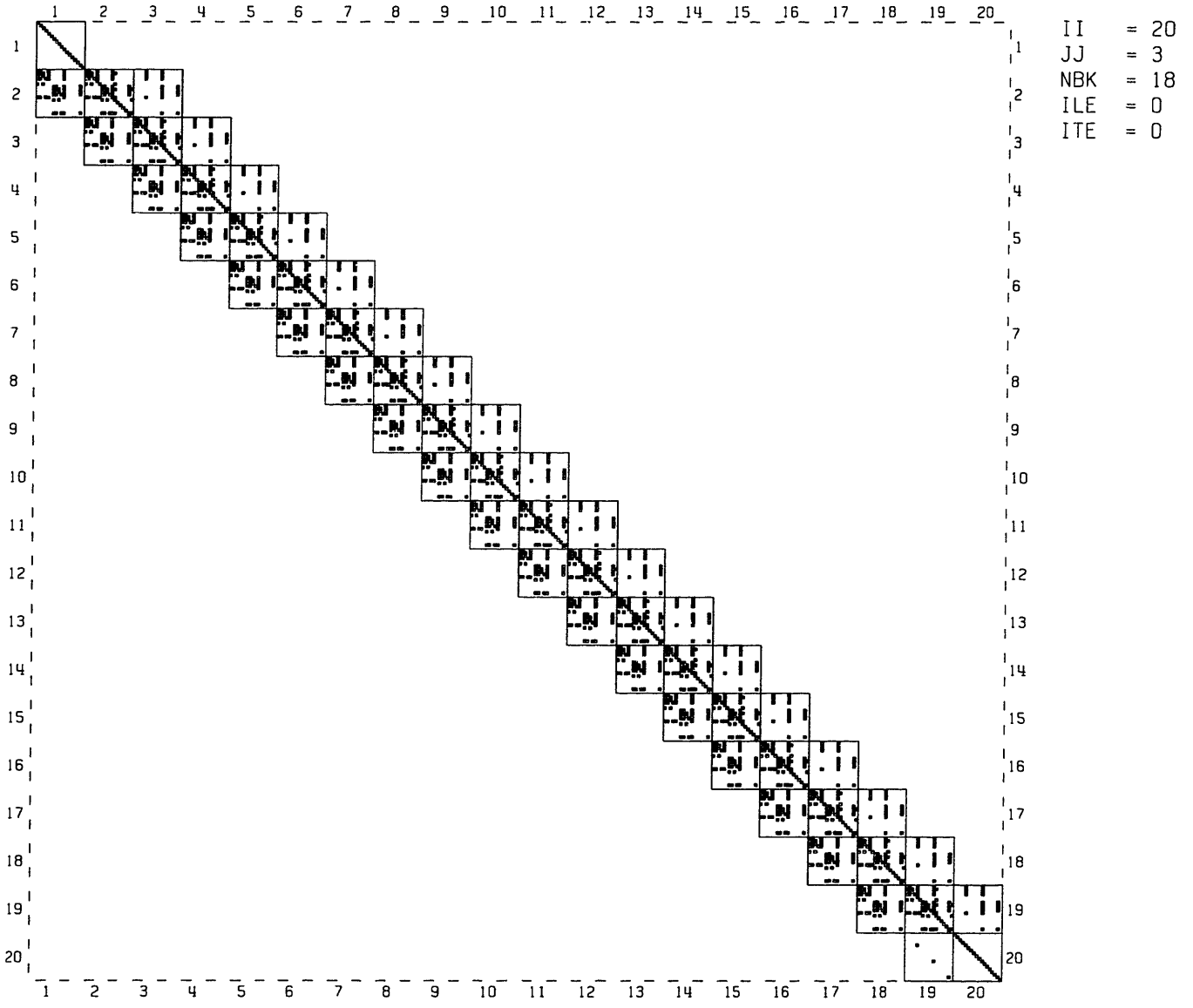

Figure B-1: Full Newton matrix for a three stream flowfield with twenty axial grid points.

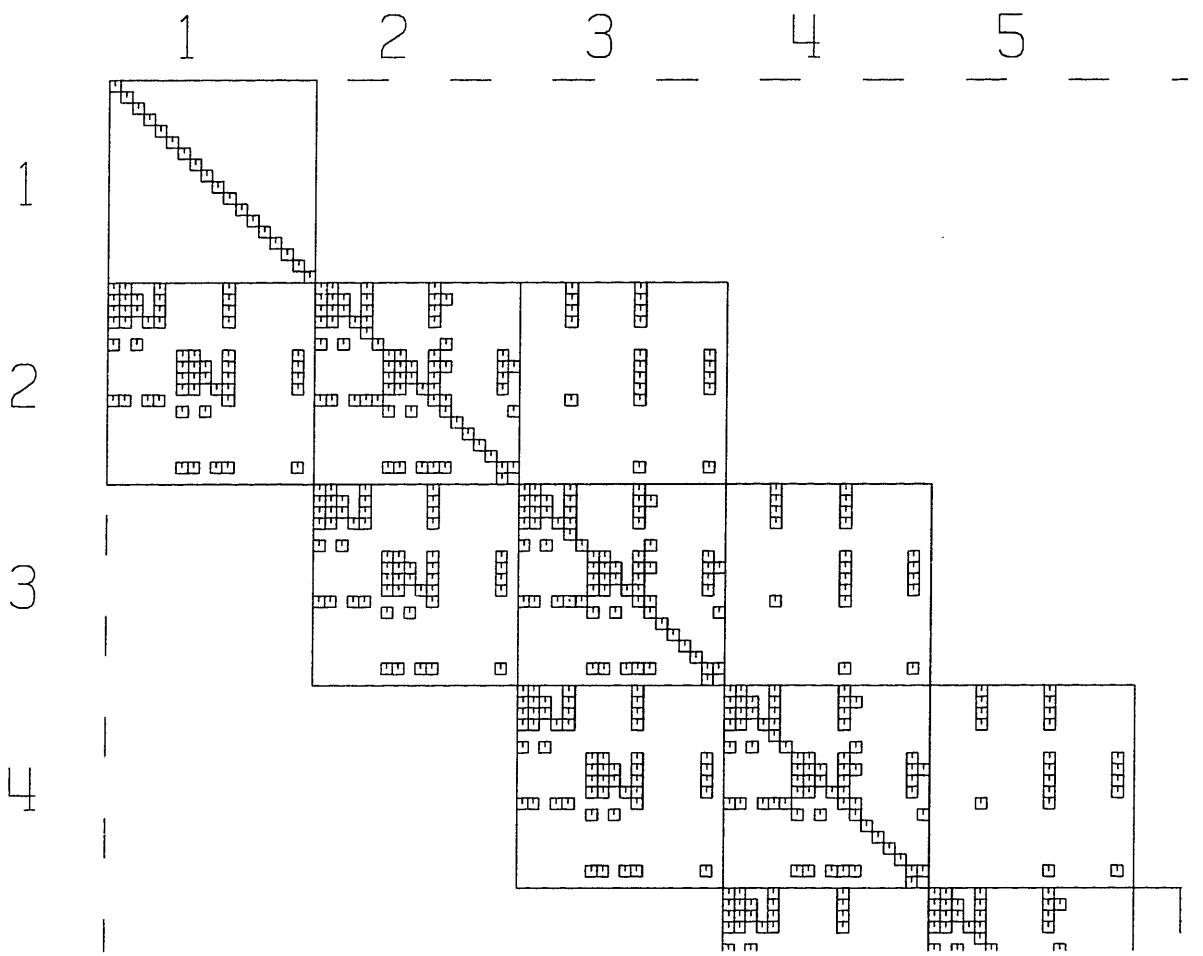

Figure B-2: Portion of Newton matrix for a three stream flowfield with twenty axial grid points.

tangential velocity, radius, and static pressure, respectively, for the first stream. The next six columns represent the state variables in the second stream, and the last six columns represent the variables in the third stream. The elements are set based on a full upwinding scheme (*i.e.*, backward Euler), and only non-zero elements of the Newton matrix are shown in Figures B-1 and B-2.

A count of the number of equations and unknowns can be carried out. As the flowfield is discretized into I axial grid points by J radial grid points. The total number of unknowns is $6IJ$ due to the presence of six state variables. Accounting for the number of equations due to residuals on the interior gives $6(I-1)(J-1)$ or $6IJ-6I-6J+6$ equations. In addition, there are $2I$ equations to account for the inner and outer wall boundary conditions on the radius. This gives a total of $6IJ-4I-6J+6$ equations. There are $4I$ dummy equations for the four face-centered variables at J. Inlet boundary conditions account for another $4(J-1)$ equations for the face variables and J equations for the pressure. Finally, the exit boundary condition of zero slope on radius gives $J-2$ equations. Adding these equations gives $6IJ$ equations, thus equaling the number of unknowns.

Appendix C

CFLOW User's Manual

This appendix contains a user's manual for CFLOW. Section C.1 gives a brief overview of the various modules of the code and their uses. Section C.2 describes the flowfield definition, while Section C.3 presents the input files needed. Program descriptions are given in Section C.4, and the output files are discussed in Section C.5.

C.1 Overview

The CFLOW system is a collection of programs for the analysis of confined combustor flows, including the effects of swirl, heat addition, and mixing. The programs and their summary descriptions are listed below.

INIT Reads the input file `input.dat`, generates the geometry, sets the inlet conditions, initializes the flow to uniform flow, and writes out an initial *state file* named `cdat.xxx`.

CFLOW Reads the `cdat.xxx` state file and the `param.dat` input file, computes the solution, and writes out a modified state file in `cdat.xxx` containing the converged solution. Can be executed repeatedly with a variety of input conditions. Allows interactive plotting of results.

CSTAT Reads the input file `input.dat` and the state file `cdat.xxx`, resets the residuals at the inlet to reflect any changes to the inlet conditions set in `input.dat`, and includes these into the `cdat.xxx` state file for subsequent reconvergence with CFLOW.

The "xxx" extension suffix is used to designate the case being run, and can be chosen arbitrarily provided it does not exceed an imposed three character limit.

An example of how one might use CFLOW is:

Set up initial flowfield in input.dat.

Create initial state file `cdat.xxx` using the command line input `% init xxx`.

Create a converged solution state file `cdat.xxx` using the command line input `% cflow xxx`.

If desired, alter the inlet conditions in `input.dat`.

Incorporate changes into `cdat.xxx` by using the command line input `% cstat xxx`.

Create a reconverged solution state file `cdat.xxx` using the command line input `% cflow xxx`.

Repeat steps 4 through 6 until the desired flowfield has been computed.

C.1.1 File/Directory Structure

The main directory is `cflow`. This contains the source code and executables. It also contains a `plotlib` subdirectory that contains the `Xplot11` routines, documentation, and archive files. Also included in the `cflow` directory is a `runs` subdirectory. The `runs` subdirectory contains subdirectories for each case run. For example, the `dln26611b` subdirectory corresponds to the CORSAIR run of the same name. Within this directory there are input files with the conditions set for this particular case, as well as all the output files from CFLOW. These files will be described below.

C.1.2 Calculation Requirements

The code is currently compiled for running on the Sun platform. Memory requirements are minimal (i.e., on the order of 10 Meg). Computational time varies from system to system, but in the worst case scenario should require no more than one minute. This would be for a case with a high number of streamtubes running on a slow or heavily loaded machine. Best case computational times would be about 5 seconds.

C.2 Flowfield Description

The flowfield is described by a *state*. This state is made up of the state variables at each grid point. The state variables are

density	(kg/m^3)
axial velocity	(m/s)
temperature	(K)
tangential velocity	(m/s)
radius	(m)
static pressure	(N/m^2)

These are divided into two different arrays due to differences in their definition. The first four state variables (density, axial velocity, temperature, tangential velocity) are defined on the interior of a control volume and are assumed constant across the control volume. There is a discontinuity in these variables at the control volume edges. These variables will be referred to as face variables, and are stored in one array. The last two variables (radius, pressure) are defined at the edge of a control volume, and are assumed to vary smoothly across the interior of the control volume. These variables will be referred to as pseudo-streamline (or just streamline for convenience) variables, and are stored in a second array. Naturally, since there is one more control volume edge than there are control volumes, the streamline variable array will be one longer than the face variable array by one in the radial direction, but equal in length in the streamwise direction.

The state variables are governed by the conservation equations. The conservation equations solved are continuity, axial momentum, energy, tangential momentum, radial momentum, and state.

C.3 Input Files

The input files needed to run CFLOW are listed below.

C.3.1 Geometry and Inlet Condition File (`input.dat`)

The geometry and initial flowfield is set up by INIT after reading in `input.dat`. The values specified in `input.dat` are described in order.

JJ	Number of control volume edges (pseudo-streamlines). This will also be equal to the number of streams plus one. JJ should never be less than 3 (a two stream case). Currently, JJ cannot exceed 10. To increase this further, redimension the JDIM variable in `CSTATE.INC`.
II	Number of axial grid points. Can vary from 3 to 50. To increase this further, redimension the IDIM variable in `CSTATE.INC`.
REPS	Small, non-zero radius added to innermost streamline in order to avoid zero radius singularities. Does not need to be changed from current value of 1.0E-5. (m/s)
RGAS	Specific gas constant for air. $(J/kg\,K)$
CP	Specific heat at constant pressure for air. Assumed constant for simplicity. $(J/kg\,K)$
PRT	Turbulent Prandtl number. Should be between 0.75 and 1.0.
CDIFF	Mixing (diffusion) coefficient. A CDIFF of 0.001 is equivalent to the mixing rate of a planar shear layer. There is no theoretical upper limit for CDIFF, although physically, a CDIFF above about 0.1 is unlikely.

BKL	Laminar mixing coefficient. Does not need to be varied, but could be set to something between 1.0 and 100.0. Used to insure at least a small, nonzero value for the mixing at all times in order to avoid singularities.
BNUL	Laminar viscosity. (m^2/s)
BREF	Reference laminar mixing length. Does not need to be changed. (m)
RAD0	Initial duct radius. Converted to meters internally. (in)
AXLEN	Axial length of duct. Converted to meters internally. (in)
UREF	Reference velocity. Typically equal to an average inlet velocity. (m/s)
PREF	Reference pressure. Equal to the centerline inlet pressure. (N/m^2)
TREF	Reference temperature. Equal to the inlet (pre-combustion) temperature. (K)
RREF	Reference length. Usually left at 1.0. (m)
PHI0	Inlet equivalence ratio. (fuel-air ratio/stoich fuel-air ratio)
SR1	Inner radius of DLN inlet. (in)
SR2	Outer radius of DLN inlet. (in)
JINN	Number of streams modeling inner recirculation zone. Should be set to 1.
JMID	Number of streams modeling DLN inlet. Can be varied from 1 to 7. To increase total number of streams beyond 9, increase JDIM in `CSTATE.INC` to that number plus 1.
JOUT	Number of streams modeling outer recirculation zone. Should be set to 1.
U*n*IN	Inlet axial velocity for stream n. Should be set to zero if not used. (m/s)
W*n*IN	Inlet swirl velocity for stream n. Should be set to zero if not used. (m/s)

The values of all variables may be adjusted prior to running INIT. Subsequent changes to `input.dat` may be made to all variables except JJ, II, REPS, RAD0, AXLEN, RREF, SR1, SR2, JINN, JMID, and JOUT. Essentially, once INIT has been run, the geometry is set, and should not be changed unless a new initialized solution is desired. All other variables may be changed and these changes incorporated into `cdat.xxx` by running CSTAT and then reconverging the solution by running CFLOW.

C.3.2 CFLOW Solution/Plotting Options (`param.dat`)

The file `param.dat` includes parameters used for selecting options during the running of CFLOW, as well as variables used during the setup and execution of the Newton solver subroutine. The parameters are described below.

iplot — Selects interactive plotting of the solution with each Newton iteration using Xplot11 subroutines developed by Harold Youngren and Mark Drela at MIT. Set to 1 to turn on, to turn off.

idump — Selects dumping of the Newton matrix to file `fort.22` for plotting by the program MATPL. This is a diagnostic tool for checking that the Newton matrix has been filled correctly. It should not be necessary to use this option. Set to 1 to turn on, 0 to turn off.

icomp — Selects a comparison routine that compares analytic and numerical values of the Jacobian in a global sense. This is another diagnostic for checking that the Jacobian elements have been computed properly. It should not be necessary to use this option. Set to 1 to turn on, 0 to turn off.

NRHS — Number of right hand sides in the Newton solver. Should be set to 1 unless design optimization variables have been specified (not yet an option).

INEWT — Sets a flag for warning message if Newton iterations failed to converge. Leave this set to 0 always.

UPW — Selects type of upwinding for Newton matrix set up.

- 1.0 Backward Euler (fully implicit)
- 0.5 Trapezoidal
- 0.0 Forward Euler

This parameter should always be set to 1.0. Selecting a fully implicit scheme allows the solution to circumvent certain singularities that would otherwise cause the convergence to fail.

PEPS — Sets a small back pressure within each control volume which prevents the area of a control volume from becoming identically zero. Should be left at 0.01, but could be changed from 0.0 to 0.1.

Recommended Settings For `param.dat`

These are the recommended settings for the variables in `param.dat`. Ideally, the only change that should be made is setting iplot to 0 in order to turn off interactive plotting. This might be useful if

recompiling on a non-Xwindow platform.

iplot	1
idump	0
icomp	0
NRHS	1
INEWT	0
UPW	1.0
PEPS	0.01

C.4 Program Descriptions

The descriptions of each program are given below. Starting from scratch, the usual program execution sequence is

```
% init xxx

% cflow xxx

% cstat xxx

% cflow xxx

% cstat xxx

% cflow xxx

.  .

.  .

.  .
```

C.4.1 INIT

INIT is the program which sets up the geometry and initializes the flowfield. It reads in the file `input.dat` and writes out a state file `cdat.xxx`, where `xxx` is an arbitrary three character/digit extension used to identify a particular case. INIT is composed of two routines and two include files. These are

`init.f`	Main program. Reads `input.dat`, sets up state, and writes it out.
`io.f`	Takes care of I/O with respect to the state file `cdat.xxx`.
`CSTATE.INC`	Defines the state and puts it into a common block for easy access in other routines.

`INDEX.INC` Defines indexing into the state arrays.

The indexing into the state arrays is defined by two different indices. The face variables are indexed from 1 to ITOT where ITOT equals 4. The streamline variables are indexed from 1 to JTOT where JTOT equals 2. Specifically the indices for the state variables are

density	IRHO	(= 1)
axial velocity	IUAX	(= 2)
temperature	ITMP	(= 3)
tangential velocity	IUTH	(= 4)

radius	JRAD	(= 1)
static pressure	JPRE	(= 2)

The state defined by `CSTATE.INC` includes variables that have been defined above in Section C.3.1. The state includes

RGAS	CP	PRT	BKL	BNUL	BREF
CDIFF	REPS	UREF	PREF	TREF	RREF

In addition, the state includes

QF	Array of face variables at all grid points.
QS	Array of pseudo-streamline variables at all grid points.
QFINL	Array of inlet face variables.
QSINL	Array of inlet pseudo-streamline variables.
QSOUT	Array of exit face variables.
QFOUT	Array of exit pseudo-streamline variables.
X	Axial distance for each axial grid point.
RINN	Duct inner radius for each axial grid point.
ROUT	Duct outer radius for each axial grid point.
HPR	Enthalpy addition due to combustion at each grid point.

C.4.2 CFLOW

CFLOW is the program which sets up and solves the problem based on the state file `cdat.xxx` written by INIT or CSTAT. If nothing has changed in `cdat.xxx`, CFLOW simply reads in the state, realizes it is already converged, and writes it back out. If the state is not converged (*i.e.*, the residuals are not zero), CFLOW performs one or more Newton iterations until the state has converged to a new solution. It then writes this new solution to `cdat.xxx`. CFLOW is composed of twelve routines and four include files. These are

`cflow.f`	Main program. Reads in `cdat.xxx` and `param.dat`, performs Newton iterations on the state, and writes out a converged state to `cdat.xxx`.
`io.f`	Takes care of I/O with respect to the state file `cdat.xxx`.
`b4dsol.f`	Newton solver. Solves a quad-diagonal system. Uses input matrices for storage during solution, thereby corrupting these matrices. Must save input matrices before calling B4DSOL if inputs will be needed again later.
`rsetup.f`	Assembles Newton matrix from elements returned by RCELL, RSTRM, and RBND.
`rcell.f`	Computes conservation equations and their derivatives excluding diffusion/mixing terms.
`rstrm.f`	Computes diffusion/mixing terms in the conservation equations as well as their derivatives for all pseudo-streamlines except the outermost wall streamline.
`rbnd.f`	Computes conservation equation terms and their derivatives for shear stresses at the wall of the duct.
`compare.f`	Compares two numbers given a tolerance for their difference. Used in the global tester invoked by setting icomp to 1.
`plsubs.f`	Calls plotting functions defined in the Xplot11 plot library.
`objfun.f`	Defines objective functions for sensitivity analysis. Currently computes inner recirculation zone volume for DLN runs.
`trans.f`	Takes a transform of a tri-diagonal matrix.
`libPltDP.a`	Archive file of compiled Xplot11 functions.
`CSTATE.INC`	Defines the state and puts it into a common block for easy access in other routines.
`INDEX.INC`	Defines indexing into the state arrays.

`LABELS.INC` Defines labels for state variables. Only used in the global testing routine.

`CPLOT.INC` Defines plot subroutine common block.

C.4.3 CSTAT

CSTAT is the used to alter the state file `cdat.xxx` for a converged solution to reflect changes in inlet quantities. For example, in order to increase the axial velocity of a case, the new value would be entered in `input.dat`. This file is read by CSTAT, the changes incorporated into the state, and an updated state written to `cdat.xxx`. The flow is then ready for reconvergence with CFLOW. CSTAT is composed of two routines and two include files. These are

`cstat.f` Main program. Reads `input.dat`, changes state, and writes it out.

`io.f` Takes care of I/O with respect to the state file `cdat.xxx`.

`CSTATE.INC` Defines the state and puts it into a common block for easy access in other routines.

`INDEX.INC` Defines indexing into the state arrays.

C.5 Output Files

The output from cflow includes both state variables and sensitivity information.

C.5.1 State Variables

The state variables and the axial coordinate are output to files in ASCII format. They are

`rho.dat`	density, ρ	(kg/m^3)
`uax.dat`	axial velocity, u	(m/s)
`tmp.dat`	temperature, T	(K)
`uth.dat`	tangential velocity, w	(m/s)
`rad.dat`	radius, r	(m)
`pre.dat`	static pressure, p	(N/m^2)
`x.dat`	axial coordinate, x	(m)

The data for multiple streamtubes is written sequentially into the file. The value of the state variable in the innermost control volume is written out in the axial direction from inlet to exit. This is done for each successive control volume until the outer wall is reached.

C.5.2 Sensitivities

The three sensitivities listed in Section 3.5 are computed for each run and dumped to the screen or to text files readable by Matlab for subsequent plotting. The overall sensitivity, $df/d\alpha$, is printed to the screen. There is currently only one f, that being the inner recirculation zone volume. There are two α's. They are the mixing coefficient, CDIFF, and the magnitude of the heat release, HPR. For these sensitivities, the change in inner recirculation zone volume is normalized by the duct volume. The mixing coefficient is dimensionless, and change in heat release is normalized by the maximum possible heat release (i.e., the lower heating value of the fuel).

The other two sensitivities are output to files in ASCII format. The adjoint is written to six files each one corresponding to one of the conservation equations. They are

`adjmass.dat`	$df/d(continuity)$
`adjxmom.dat`	$df/d(axialmomentum)$
`adjenergy.dat`	$df/d(energy)$
`adjthmom.dat`	$df/d(tangentialmomentum)$
`adjrmom.dat`	$df/d(radialmomentum)$
`adjstate.dat`	$df/d(state)$

For these sensitivities, the change in inner recirculation zone volume is again normalized by the duct volume. The residuals are normalized by the following

continuity	RHOREF*UREF *PI*RREF**2
axial momentum	RHOREF*UREF**2*PI*RREF**2
energy	CP*TREF
tangential momentum	RHOREF*UREF**2*PI*RREF**2 * RREF
radial momentum	RHOREF*UREF**2*PI*RREF**2
state	PREF

The sensitivity of state variables to changes in knobs, $dU/d\alpha$, is written to six more files corresponding to the six state variables, and named

`rho_a.dat`	$d\rho/d\alpha$
`uax_a.dat`	$du/d\alpha$
`tmp_a.dat`	$dT/d\alpha$
`uth_a.dat`	$dw/d\alpha$
`rad_a.dat`	$dr/d\alpha$
`pre_a.dat`	$dp/d\alpha$

For these sensitivities, the mixing coefficient is again dimensionless, and the heat release is normalized by the lower heating value of the fuel. The state variables are normalized by the following

rho	RHOREF
uax	UREF
tmp	TREF
uth	UREF
rad	RREF
pre	PREF

All output of state variables and sensitivities is handled at the end of the main program `cflow.f`.

Appendix D

Recirculation Zone Dynamics

Recirculation zone dynamics can have a large impact on the overall combustion system performance[26]. Assuming that the downstream pressure is linked to the dynamics of the recirculation zone, modification of the existing sensitivity analysis could yield information about changes in recirculation zone volume due to changes in static pressure at a given radial location in the exit plane.

For a converged state

$$\bar{U} = 0, \tag{D.1}$$

the exit pressure boundary condition in subroutine RSETUP can be changed to allow specification of a radial pressure profile. With this new exit condition, the system becomes

$$R(U) = b(U), \tag{D.2}$$

where the new state is U, and $b(U)$ represents the change in the exit boundary condition. Linearizing, we get

$$R(\bar{U}) + \frac{\partial R}{\partial U}\Delta U = b(\bar{U}) + \frac{\partial b}{\partial U}\Delta U. \tag{D.3}$$

We know that $R(\bar{U}) = 0$. After rearrangement

$$\left(\frac{\partial R}{\partial U} - \frac{\partial b}{\partial U}\right)\Delta U = b(\bar{U}), \tag{D.4}$$

and solving for ΔU

$$\Delta U = \left[\frac{\partial R}{\partial U} - \frac{\partial b}{\partial U}\right]^{-1} b(\bar{U}). \tag{D.5}$$

Now linearizing f for changes in U

$$\Delta f = \frac{\partial f}{\partial U}\Delta U, \tag{D.6}$$

and substituting in for ΔU from Equation D.5

$$\Delta f = \frac{\partial f}{\partial U}\left[\frac{\partial R}{\partial U} - \frac{\partial b}{\partial U}\right]^{-1} b(\bar{U}). \tag{D.7}$$

This is the expression that must be evaluated for the general case. Thus, the change in f would be computed after a converged solution was obtained for no perturbation in the exit pressure. This change in f could be divided by the change in U to give the local sensitivity of the inner recirculation zone volume to changes in static pressure at the exit. However, this system must be solved anew for each point in the flowfield, adding considerable computational expense.

Appendix E

Unsteady CFLOW

The potential exists to extend the steady-state CFLOW formulation to unsteady flows. A steady analysis similar to that of CFLOW has been extended to unsteady flows by Drela[39]. The steady and unsteady analyses of Drela did not account for mixing between streams or for swirling flow. These effects must be incorporated. The extension for the zero mass transport case involves definition of a grid based on streaklines instead of streamlines. This grid is defined by grid nodes whose velocity normal to the streakline is equal to the normal component of the flow velocity. Figure E-1 shows this arrangement.

The conservation cell is defined as it was in the steady formulation. The geometric grid nodes (x, y) define the conservation-cell face vectors $(\vec{a}, \vec{b})$ which connect the midpoints of the grid streakline segments. The grid also defines the velocity-direction vector $(\vec{s})$, which connects the midpoints of the vertical grid line segments. The flow velocity relative to the grid is defined as

$$q = \frac{m}{\rho A} \frac{\vec{s}}{|\vec{s}|}. \tag{E.1}$$

The grid velocity is given by

$$\vec{u} = \dot{y}\hat{j}, \tag{E.2}$$

making the absolute velocity

$$\vec{Q} = \vec{q} + \vec{u}. \tag{E.3}$$

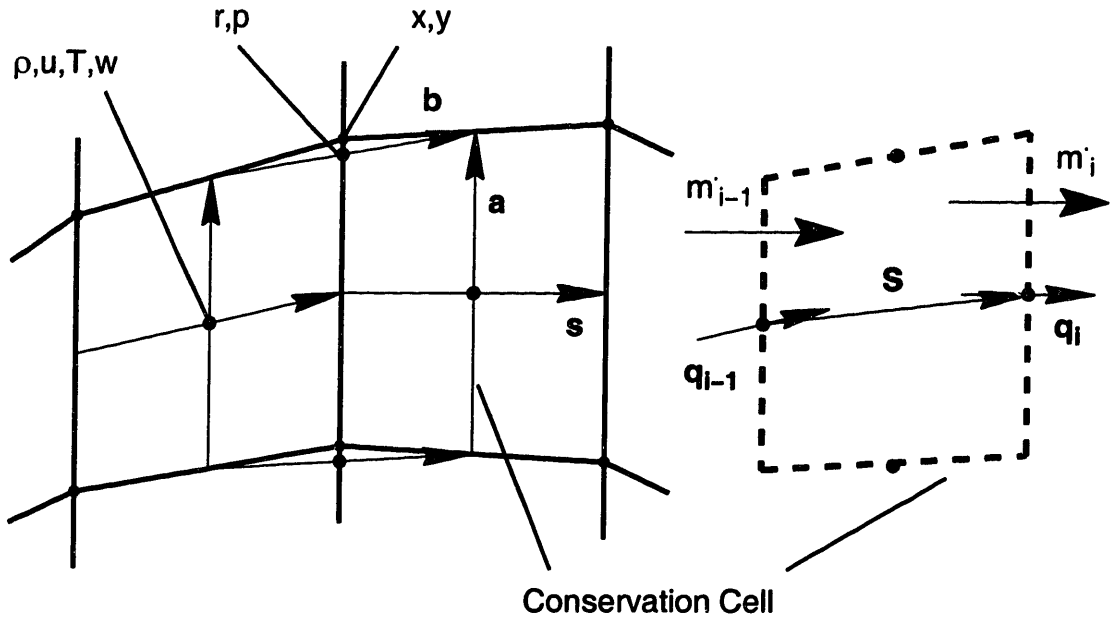

Figure E-1: Geometric grid, conservation cell, and variable locations for an unsteady formulation of CFLOW.

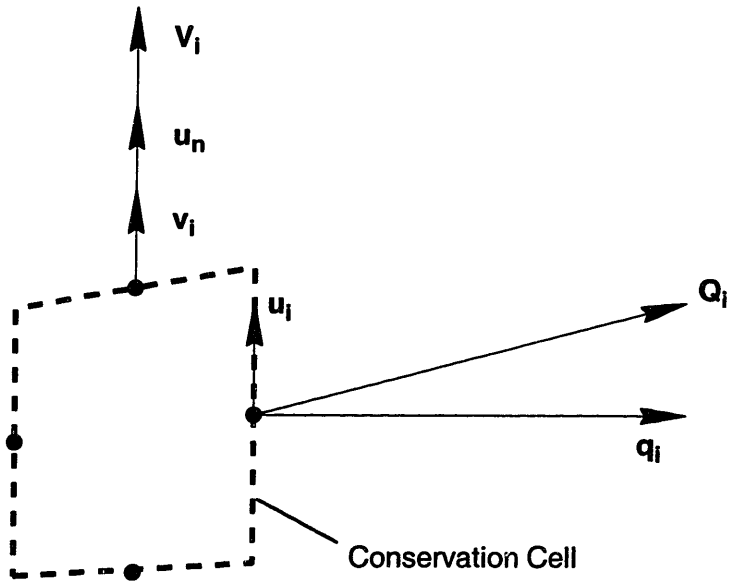

Figure E-2: Cell-face grid velocities and flow velocity vector relations for an unsteady formulation of CFLOW.

In addition, the grid velocity of the midpoint of $\vec{b}$ can be denoted by $\vec{v}$. This must be added to the implied radial velocity from the steady formulation. Thus

$$\vec{V} = \vec{u_n} + \vec{v}. \tag{E.4}$$

The energy equation should be written using Q and V instead of q and u_n. Figure E-2 shows the two grid velocities.

Writing the unsteady conservation equations, the residuals will include all of the steady terms, an unsteady term, and terms to account for non-physical grid motion and $p\,dV$ work due to expansion of the conservation cell. These terms are then added to the residuals on the diagonal of the Newton matrix, as well as lower diagonal terms due to upwinding.

THESIS PROCESSING SLIP

FIXED FIELD: ill. _____ name _____

index _____ biblio _____

▶ COPIES: (Archives) (Aero) Dewey Eng Hum

Lindgren Music Rotch Science

TITLE VARIES: ▶☐ _____

NAME VARIES: ▶☐ _____

IMPRINT: (COPYRIGHT) _____

▶ COLLATION: 135P

▶ ADD: DEGREE: _____ ▶ DEPT.: _____

SUPERVISORS: _____

NOTES:

cat'r: date:

page: 1-74

▶ DEPT: Aero

▶ YEAR: 1999 ▶ DEGREE: Sc. D.

▶ NAME: UNDERWOOD, David Scott